CORA Cork Open Research Archive
Cartlann Taighde Oscailte Chorcaí

Title	Electronic spectroscopy of thiones
Authors	Doherty, William G.
Publication date	2003
Original Citation	Doherty, W. G. 2003. Electronic spectroscopy of thiones. PhD Thesis, University College Cork.
Type of publication	Doctoral thesis
Link to publisher's version	http://library.ucc.ie/record=b1360019~S0
Rights	© 2003, William G. Doherty - http://creativecommons.org/licenses/by-nc-nd/3.0/
Download date	2026-11-05 12:30:34
Item downloaded from	https://hdl.handle.net/10468/1601



UCC
University College Cork, Ireland
Coláiste na hOllscoile Corcaigh

DP2003 DOHE

The National University of Ireland

Electronic Spectroscopy of Thiones

A thesis presented to

Chemistry Department — Roinn na Ceimice
University College, — Coláiste na hOllscoile,
Cork — Corcaigh

for the degree of

Ph.D.

by

William G. Doherty

August 2003

UNIVERSITY COLLEGE Library CORK

Contents

1 General Introduction **1**

1.1 Photophysics of Thiocarbonyls 2

1.1.1 The Thiocarbonyl Chromophore 2

1.1.2 Electronic Energy Levels 3

1.1.3 Electronic Symmetries and Transitions 4

1.2 Radiationless Transitions 9

1.3 Vibronic Coupling Schemes 12

1.4 Outline of Thesis 17

2 Experimental Details **23**

2.1 Phosphorescence Excitation 23

2.1.1 Laser System 24

2.1.2 Wavelength Calibration 25

2.1.3 Pulsed Nozzle System 26

2.1.4 Detection System 27

2.1.5 Data Correction 28

2.2 Cavity Ring-down Spectroscopy 29

2.2.1 Experimental Principles 30

2.2.2 Apparatus 34

2.3 Synthesis of 4-*H*-Pyrane-4-thione 35

2.4 Supersonic Jet Expansion Characteristics 37

UNIVERSITY COLLEGE LIBRARY CORK

3 Phosphorescence Excitation Spectrum of Xanthione **46**

3.1 Experimental Details 47

3.2 Results and Discussion 49

3.2.1 The origin of T_{1_x} 49

3.2.2 Vibrational Analysis 50

3.2.3 Observability of $S_1 \leftarrow S_0$ 61

3.3 Conclusions 66

4 Phosphorescence Excitation Spectrum of 4*H*–pyrane–4–thione **70**

4.1 Introduction 70

4.2 Experimental 71

4.3 Results 74

4.4 Discussion 76

4.4.1 The hidden state $^1B_1(n\pi^*)$ 80

4.4.2 Vibronic Structure 85

4.4.3 Linewidths and Relaxation Dynamics 87

4.5 Conclusions 92

5 Vibronic Lineshape of 4–*H*–Pyran–4–thione **95**

5.1 Introduction 95

5.2 Vibronic Lineshape Analysis 99

5.3 Calculation of Lineshapes 102

5.4 Results and Discusson 108

5.5 Summary 114

6 Conclusions **117**

Abstract

The phosphorescence excitation spectra of two thiones, 4-*H*-1-xanthione (XT) and 4-*H*-1-pyrane-4-thione (PT), cooled in a supersonic jet were investigated. The vibronic lineshape of the T_{1z} origin of PT measured by cavity ring-down spectroscopy is considered and the excited state rotational constants are calculated.

For XT the $^3A_2(n\pi^*) \rightarrow X^1A_1$ phosphorescence excitation spectrum was investigated in the region 14900–17600 cm^{-1}. The structure observed is shown to be due to the $T_1 \leftarrow S_0$ absorption and an assignment in terms of the vibronic structure of the band is proposed. A previous assignment of the $S_1 \leftarrow S_0$ origin is considered and the transition involved is shown to be most probably due to the absorption of a vibronic triplet state T_{1z,ν_7}. An alternative but tentative assignment of the $S_{1,0} \leftarrow S_{0,0}$ transition is suggested.

In the case of PT the phosphorescence excitation spectrum was investigated in the region of the $^1A_2(\pi\pi^*) \leftarrow X^1A_1$ absorption band between 27300 and 28800 cm^{-1}. The spectrum exhibits complex features which are typical for the strong vibronic coupling case of two adjacent electronic states. The observed intermediate level structure was attributed to the coupling with a lower lying dark electronic state $^1B_1(n\pi_2^*)$, whose origin was estimated to be $\sim$ 825 – 1025 cm^{-1} below the origin of $^1A_2(\pi\pi^*)_0$. Consequences of the vibronic coupling on the decay dynamics of $^1A_2(\pi\pi^*)$ as well as tentative assignments of vibronic transitions $^1A_2(\pi\pi^*)_\nu \leftarrow X^1A_1$ are also discussed.

In the $T_{1z} \leftarrow S_0$ cavity ring-down absorption spectrum of PT, the vibronic lineshape of the T_{1z} origin is analysed. As the T_{1z} line is separated from the $T_{1x,1y}$ lines by a large zero-field splitting it is possible to use an Asyrot-like program to calculate the vibrational-rotational parameters determining the lineshape. It is shown that PT is non-planar in the first excited triplet state and the lineshape is composed of a mixture of A–type and C–type bandshapes. The non-planarity of PT is discussed.

Acknowledgements

To list everyone that has in some way or another aided (and abetted) or contributed to the work detailed in this thesis would take a very long time indeed. However, it is important that they be thanked. Firstly, I would like to thank my supervisor Prof. Paul Brint for his help, support, enthusiasm and patience. Also, Dr. Andy Ruth whose vast experience and encouragement were invaluable. Also thanks must be given to Dr. Larry Singleton who guided me through my first steps as a post-graduate and to Dr. Frank O'Keeffe whose impact on the lab is immense.

Tony Hogan, Mick O'Shea (not the real?), Johnny Ryan and Derry Kearney of the Chemistry Department and John Lucey and Christy Roche of the Physics Department technical stff, a big thank you for all the work and effort you have done on my behalf.

Thanks must also be given to all those people who had to try extremely hard to entice me out into the seedy social world of Cork; Aaron, Clive, Ed, Lewis and all the Men in Black, the spirit was willing but the ankles weren't.

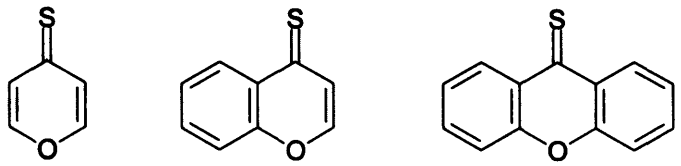
A huge debt of thanks and gratitude are due to my parents Willie and Aileen without whose unending support, patience, encouragement and inspiration I could never have embarked upon my studies.

Finally, to Joy.

Chapter 1

General Introduction

The carbonyl group compounds have been the most important of organic compounds in developing the understanding of the photochemistry and photophysics of polyatomic molecules [1]. They were first investigated towards the beginning of the twentieth century and have been a major topic of investigation ever since. It was not until more recently (e.g. [2,3]) that attention has turned to their sulphur-containing analogs, thiones, and only in the nineteen-sixties that this class of compounds was seriously investigated. This can be attributed to various reasons of which their tendency to have a noxious odour, which is mainly due to impurities, is not insignificant. These compounds are also less stable and had a tendency to polymerise, and those with an α-hydrogen, to thioenolise. However, advances in the ability to synthesize thiones has led to a renewed interest in their photophysics. The thiones have unusual photophysical, photochemical and spectroscopic characteristics and this renewed interest has given rise to many publications in recent years, [4–10], primarily dealing with the thiones in condensed phases. Work in this laboratory has investigated the compounds 4-*H*-1-pyrane-4-thione (PT) and 4-*H*-1-benzopyrane-4-thione (BPT) and in connection with the work in this thesis xanthione (XT) in the gas phase as cold isolated molecules in a supersonic jet [11–13].



(a) (b) (c)

Figure 1.1: (a) PT; (b) BPT; (c) XT

1.1 Photophysics of Thiocarbonyls

This section gives a brief synopsis of the known photophysical properties of PT, XT, and BPT. Most measurements have been recorded in cryogenic matrices or solution.

1.1.1 The Thiocarbonyl Chromophore

Molecular Orbital Theory shows that the lowest energy transitions observed in ketones and thioketones occur between the highest-energy occupied molecular orbital (HOMO) and the lowest-energy unoccupied molecular orbital (LUMO). Spectroscopic studies and computational methods show that the molecular orbitals (MOs) of the thiones involved in the low energy electronic transitions are predominately located on the C=S chromophore. The MOs are the n, π and π^* orbitals as shown in Figure 1.2. The electrons in the non-bonding n orbital on the sulphur atom are of higher energy than the equivalent electrons on a carbonyl oxygen and hence require less energy for excitation. This reduction in excitation energy brings the transitions to the lowest excited states, S_1 and T_1, from the near ultraviolet in carbonyls to the red in thiocarbonyls. The transitions from S_0 to T_1 and to S_1 involve the excitation of an electron from the non-bonding n orbital to the π^* orbital; while in the transitions from S_0 to T_2 and to S_2 an electron is excited from the π orbital to the π^* orbital. Hence,

UNIVERSITY COLLEGE CORK

they are referred to as (n, π^*) and (π, π^*) transitions, respectively.

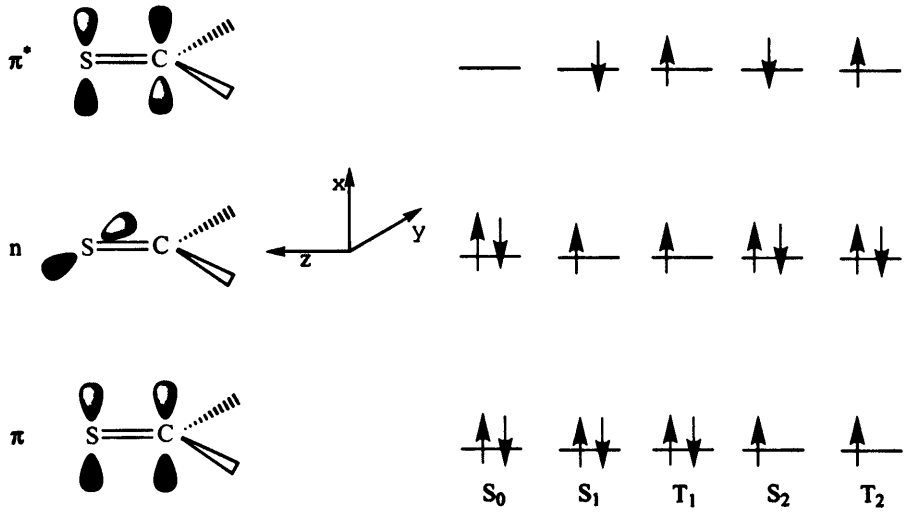


Figure 1.2: Orbital configuration of the C=S chromophore, occupancies, spin configuration and designation, together with the axis convention used throughout this thesis.

1.1.2 Electronic Energy Levels

When considering the UV and visible spectra of the thiones, a minimum of five electronic states, S_0, S_1, T_1, S_2 and T_2, are required.

The occupancies of these orbitals, their spin configuration and designation are shown in Figure 1.2 and their relative energies are shown in Figure 1.3

One of the most immediately noticeable features of the spectra of thiones is the large energy gap between S_1 and S_2, being in the region of $\sim$hc$\times$9700 cm^{-1} for PT in a perfluoralkane solvent [14], $\sim$hc$\times$8800 cm^{-1} for BPT in a perfluoralkane solvent [14] and $\sim$hc$\times$7200 cm^{-1} for XT in a Shpolskii matrix [15]. The same energy gap for xanthone in a supersonic jet is $\sim$hc$\times$2444 cm^{-1} [16], for naphthalene in a supersonic jet is $\sim$hc$\times$3900 cm^{-1} [17] and for biphenylene in chloroform solvent is $\sim$hc$\times$3950 cm^{-1} [18]. S_1 is low in energy due to the low excitation energy of the n_{py} orbital located on the sulphur atom as mentioned

in Section 1.1.1 above. This leads to a strong Franck-Condon inhibition of the $S_2 \rightsquigarrow S_1$ internal conversion, according to the energy gap law (see Section 1.2). This leads in turn to the fact that the competing relaxation pathways, namely (i) $S_2 \rightarrow S_0$ fluorescence and (ii) intersystem crossing to the triplet manifold followed by internal conversion to T_1, have significant quantum yields. In violation of Kasha's rule (Section 1.2), the prompt electric dipole allowed $S_2 \rightarrow S_0$ fluorescence is therefore readily observed in these compounds.

A second noticeable feature is the unusually small S_1 – T_1 energy gap ($\Delta E_{S_1,T_1} \lesssim hc \times 750$ cm^{-1} for all three thiones discussed here [19–21]) caused by the small overlap $\langle \psi_n | \psi_{\pi^*} \rangle$ between the n_{py} and π^* orbitals, with a consequently small exchange integral. In solution at room temperature a fast and virtually complete thermal equilibrium of $T_1 \rightleftharpoons S_1$ of the relative populations of S_1 and T_1 can be assumed. In a supersonic expansion, however, this is not the case. As the density of vibronic T_1 states near the S_1 origin is very low, there is very weak vibronic coupling between these two manifolds. (See Section 1.3 for more details.) Unlike the S_1–T_1 energy gap which is small, the S_2–T_2 energy separation is expected to be quite large. The energy of T_2 has not been determined for any aromatic thione but is expected to lie within 600–2400 cm^{-1} above T_1. Amongst the small thiocarbonyls T_2 has only been observed spectroscopically by electron-impact energy-loss in Cl_2CS [22]. This is consistent with ab initio calculations carried out by Burton et al. [23] which places T_2 only slightly higher than S_1 in the prototype H_2CS.

1.1.3 Electronic Symmetries and Transitions

Using the axis convention as shown in Figure 1.2 the n orbital transforms as B_2 and both the π and π^* orbitals transform as B_1 under C_{2v}. As the molecules dealt with in this thesis belong to this group the following applies. The direct

products for the transition moments are:

$$\Gamma_n \otimes \Gamma_{x,y,z} \otimes \Gamma_{\pi^*}$$

$$\begin{aligned} B_2 \otimes \Gamma_x \otimes B_1 &= B_2 \otimes B_1 \otimes B_1 = B_2 \\ B_2 \otimes \Gamma_y \otimes B_1 &= B_2 \otimes B_2 \otimes B_1 = B_1 \\ B_2 \otimes \Gamma_z \otimes B_1 &= B_2 \otimes A_1 \otimes B_1 = A_2 \end{aligned} \tag{1.1}$$

Since none of these resulting representations contains the totally symmetric representation, A_1, the $n \rightarrow \pi^*$ (and hence the $S_0 \rightarrow S_1$) transition is symmetry forbidden. As a result, an $n \rightarrow \pi^*$ transition is quite weak; PT in 3-methylpentane has an extinction coefficient of $\epsilon_{S_1} = 15$ $dm^3cm^{-1}mol^{-1}$ [24]. The $S_0 \rightarrow S_2$ transition is symmetry allowed;

$$\begin{aligned} B_1 \otimes \Gamma_x \otimes B_1 &= B_1 \otimes B_1 \otimes B_1 = B_1 \\ B_1 \otimes \Gamma_y \otimes B_1 &= B_1 \otimes B_2 \otimes B_1 = B_2 \\ B_1 \otimes \Gamma_z \otimes B_1 &= B_1 \otimes A_1 \otimes B_1 = A_1 \end{aligned} \tag{1.2}$$

The transition has an extinction coefficient $\epsilon_{S_2} = 1.7 \times 10^4 dm^3cm^{-1}mol^{-1}$ in 3-methylpentane.

When dealing with singlet–triplet transitions, one must consider the spin $\otimes$ orbital symmetries of the triplet substates involved. T_{1x}, T_{1y} and T_{1z} have B_1, B_2 and A_1 symmetries, respectively. This is discussed in more detail in the following section. Although transitions to the T_1 and S_1 states from S_0 are spin and symmetry forbidden, transitions from S_0 to the triplet substates

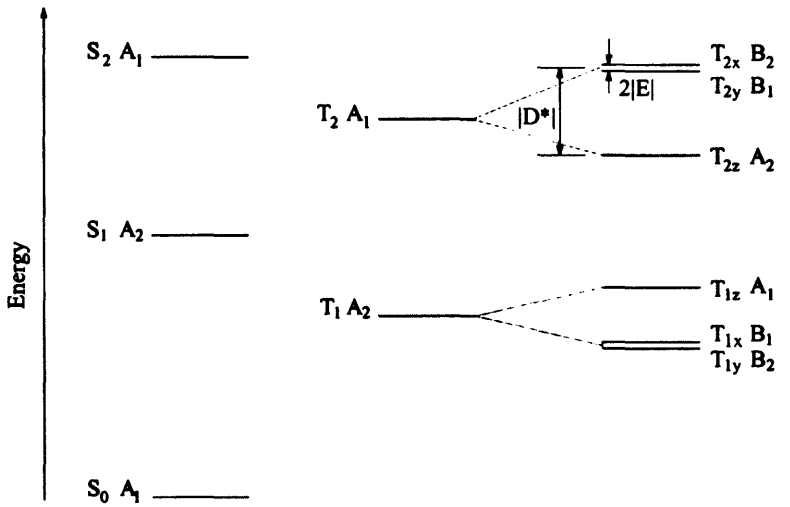


Figure 1.3: Schematic diagram showing the zero-field splittings and the sub-level symmetries of the T_1 and T_2 states of C_{2v} thiones. The ordering of the energies of T_{2z} and T_{2x},T_{2y} is arbitrary.

T_{1x}, T_{1y} and T_{1z} are spin-orbit allowed.

$$\Gamma_{\text{gr.state}} \otimes \Gamma_{x,y,z} \otimes \Gamma_{\text{ex.state}}$$

$$\begin{aligned} A_1 \otimes \Gamma_x \otimes \Gamma_{T_{1x}} &= A_1 \otimes B_1 \otimes B_1 \subset A_1 \\ A_1 \otimes \Gamma_y \otimes \Gamma_{T_{1y}} &= A_1 \otimes B_2 \otimes B_2 \subset A_1 \\ A_1 \otimes \Gamma_z \otimes \Gamma_{T_{1z}} &= A_1 \otimes A_1 \otimes A_1 \subset A_1 \end{aligned} \tag{1.3}$$

Determination of Triplet Substate Symmetries

When considering the classification of electronic states, the symmetry properties of electron spin are usually disregarded. The electronic eigenfunction ψ_e is considered to be a function of the positional coordinates of the electrons. Therefore, the symmetry species refer to the symmetry properties of these orbital wavefunctions. The spin multiplicity of the electronic state must be taken into account where there is one or more unpaired electrons in the molecule. As long as the multiplet splitting is small, the total electronic eigenfunction ψ_{es} may be written as a product of an orbital function ψ_e and a spin function β

$$\psi_{es} = \psi_e \cdot \beta \tag{1.4}$$

To obtain the spin function one may use a space-fixed or a molecule-fixed coordinate system. The space-fixed system is particularly appropriate when the spin–orbit interaction is very small and the spin function is then not affected by any of the symmetry operations of the molecule and the species of the total electronic eigenfunction is the same as that of the orbital function.

However, if the spin–orbit interaction is not negligibly small, it is more appropriate to use molecule-fixed spin functions. These functions are affected by the symmetry operations and therefore must belong to one of the species of the point group of the molecule. It has been shown [25] that for integer spin (i.e. for an even number of electrons) the spin function belongs to one of the even species of the group K_h, viz., D_{0g}, D_{1g}, D_{2g},... depending on whether $S = 0, 1, 2\ldots$ respectively (See Table 1.1). Thus for $S = 1$ the triply degenerate species D_{1g} is obtained. For the molecules in this thesis with point group symmetry C_{2v}, $\varphi = 180°$. Substituting $\varphi = 180°$ into the D_{1g} row of Table 1.1, for the triplet substates T_{1z}, T_{1x}, T_{1y}, $S = 1$, one obtains the reducible representation under C_{2v} with characters $3, -1, \ldots$ which yields on

K_h	I	∞C_∞^φ	$\infty C_\infty^{2\varphi}$	$\cdots$	R	$\infty C_\infty^\varphi R$	$\cdots$
$D_{0g} \equiv S_g$	1	1	1	$\cdots$	1	1	$\cdots$
$D_{1g} \equiv P_g$	3	$1+2\cos\varphi$	$1+2\cos 2\varphi$	$\cdots$	3	$1+2\cos\varphi$	$\cdots$
$D_{2g} \equiv D_g$	5	$1+2\cos\varphi+2\cos 2\varphi$	$1+2\cos 2\varphi+2\cos 4\varphi$	$\cdots$	5	$1+2\cos\varphi+2\cos\varphi$	$\cdots$

Table 1.1: K_h Point Group

reduction $A_2 + B_1 + B_2$ (see Table 1.2). Referring to the C_{2v} point group given in Table 1.3 and using the the rotational representations $R_z = A_2$, $R_x = B_1$ and $R_y = B_2$, it can be easily seen that A_2 is the symmetry representation of the spin function β_z of the $^3\Gamma_{1z}$ state (R_z), β_x of the $^3\Gamma_{1x}$ state (R_x) has B_1 symmetry and β_y of the $^3\Gamma_{1y}$ state (R_y) has B_2 symmetry. Now that the species of the spin functions, β, for the multiplet state have been determined, it is a straightforward operation to obtain the total electronic wavefunction ψ_{es}. Similar to the determination of electronic state symmetries in Section 1.1.3, the symmetry representation of the total electronic wavefunction, $\Gamma_{\psi_{es}}$, is obtained by

$$\begin{aligned} \Gamma_{\psi_{es}} &= \Gamma_{\psi_e} \otimes \Gamma_\beta && (1.5) \\ &= A_2 \otimes A_2, B_1, B_2 \\ &= A_1, B_2, B_1 && (1.6) \end{aligned}$$

Thus the triplet substates $^3\Gamma_{1z}$, $^3\Gamma_{1x}$, and $^3\Gamma_{1y}$ have A_1, B_2 and B_1 symmetries respectively. In Table 1.2, [25], the species of spin functions of the more important point groups are given.

S	$C_i(C_1)$	C_s	$C_{2h}(C_2)$	C_{2v}	$D_{2h}(D_2)$
0	A_g	A'	A_g	A_1	A_g
$\frac{1}{2}$	$2B_{\frac{1}{2}g}$	$E_{\frac{1}{2}}$	$E_{\frac{1}{2}g}$	$E_{\frac{1}{2}}$	$E_{\frac{1}{2}g}$
1	$3A_g$	$A'+A''$	A_g+2B_g	$A_2+B_1+B_2$	$B_{1g}+B_{2g}+B_{3g}$
$\frac{3}{2}$	$2B_{\frac{1}{2}g}+2B_{\frac{1}{2}g}$	$2E_{\frac{1}{2}}$	$2E_{\frac{1}{2}g}$	$2E_{\frac{1}{2}}$	$2E_{\frac{1}{2}g}$
2	$A_g+2A_g+2A_g$	$3A'+2A''$	$3A_g+2B_g$	$2A_1+A_2+B_1+B_2$	$2A_g+B_{1g}+B_{2g}+B_{3g}$
$\frac{5}{2}$	$2B_{\frac{1}{2}g}+2B_{\frac{1}{2}g}+2B_{\frac{1}{2}g}$	$3E_{\frac{1}{2}}$	$2E_{\frac{1}{2}g}$	$2E_{\frac{1}{2}}$	$2E_{\frac{1}{2}g}$

Table 1.2: Species of spin functions for the more important point groups

	E	C_2	$\sigma_v(xz)$	$\sigma'_v(yz)$		
A_1	1	1	1	1	T_z	$\alpha_{xx}, \alpha_{yy}, \alpha_{zz}$
A_2	1	1	−1	−1	R_z	α_{xy}
B_1	1	−1	1	−1	T_x, R_y	α_{xz}
B_2	1	−1	−1	1	T_y, R_x	α_{yz}
$\Gamma_{x,y,z}$	3	−1	1	1		

Table 1.3: C_{2v} Point Group Table.

1.2 Radiationless Transitions

One of the principal mechanisms for electronic relaxation in the excited states of molecules is the transfer of electronic energy to vibrations without photon emission. These radiationless transitions can populate metastable excited electronic and vibrational states, which are difficult to prepare by direct optical excitation due to low oscillator strengths. This does not mean that they are impossible to populate as the direct $T_1 \leftarrow S_0$ excitation spectrum of Xanthione in Chapter 3 shows. Population of these metastable states can lead to many interesting physical phenomena such as delayed fluorescence, triplet-triplet absorption and phosphorescence. The dynamics of these electronically excited states are determined by the efficiency of the relaxation pathway. While the dynamics of the luminescent relaxation pathways are relatively easily determined, those of radiationless transitions must be determined indirectly.

The Jabloński diagram in Figure 1.4 shows the relaxation processes that can occur in condensed media. As is the case with all molecules with no unpaired electrons in their ground configuration, the ground state is a singlet and is denoted by S_0. Subsequent excited states within the singlet manifold are labelled $S_1 \ldots S_n$. Also, upon excitation from a singlet ground state, triplet states are produced giving a triplet manifold, similarly labelled $T_1 \ldots T_n$, with the triplets generally lying at lower energy than their corresponding singlet states (i.e. $E_{T_1} < E_{S_1}$, $E_{T_2} < E_{S_2}$ $\cdots$ $E_{T_n} < E_{S_n}$). Associated with each

of these electronic states are vibrational levels. At high excess energy these vibronic states form a continuum.

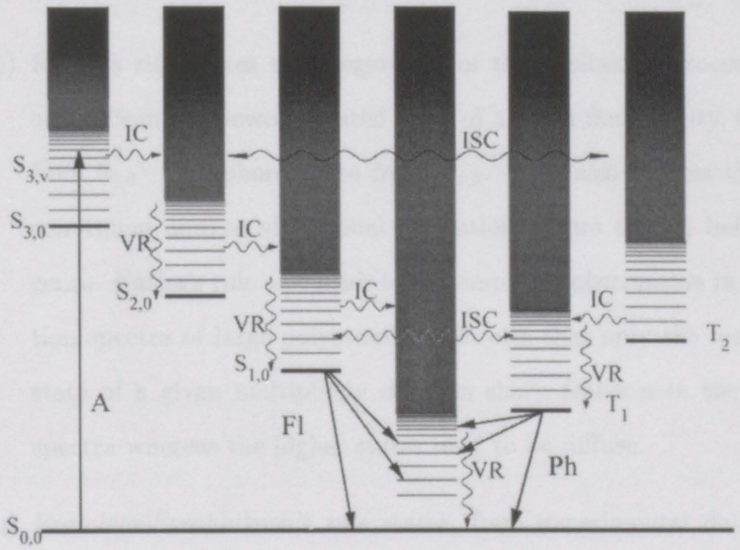


Figure 1.4: **A:** Absorption. **Fl:** Fluorescence. **Ph:** Phosphorescence. **IC:** Internal Conversion. **ISC:** Intersystem Crossing. **VR:** Vibrational Relaxation.

Upon absorption, (process A in Figure 1.4), usually with excess vibrational energy, numerous pathways are available to return the excited molecule to the ground state. Firstly, radiative processes may occur. These transitions, fall into two categories, fluorescence (Fl) and phosphorescence (Ph). Fluorescence involves a transition within the same manifold, i.e. without changing multiplicity. Usually, fluorescence occurs from the $S_{1,0} \rightarrow S_{0,v}$. Phosphorescence is a radiative transition that involves a change in multiplicity, e.g. $T_{1,0} \rightarrow S_{0,v}$. Secondly, there are radiationless transitions. These occur without the emission of photons. There is vibrational relaxation, VR, $S_{1,v} \rightsquigarrow S_{1,0}$. Also, transitions from $S_{1,v}$ to other isoenergetic levels such as $S_{0,w}$, called *internal conversion*, IC, or to $T_{1,u}$, called *intersystem-crossing*, ISC, may occur.

The evidence for radiationless transitions are:

(i) $S_1 \leftarrow S_0$ absorption brings about $S_1 \rightarrow S_0$ fluorescence. The quantum yield, ϕ, of this process is less than unity. This implies that there is a radiationless deactivation process occurring within the S_1 state.

(ii) *Kasha's rule* states that regardless of the excitation process, emission occurs from the lowest excited state of a given multiplicity, fluorescence from $S_{1,0}$[1], phosphorescence from $T_{1,0}$. This also implies that internal conversion and/or vibrational relaxation occurs to $S_{1,0}$ before fluorescence. Kasha's rule also leads to the empirical observation in the absorption spectra of large polyatomic molecules that only the lowest excited state of a given multiplicity displays sharp features in the absorption spectra whereas the higher states tend to be diffuse.

(iii) *Ermolaev-Sveshnikova's rule* states, from experimental data, that the dominating channel for the physical intramolecular degradation of the emission from the first excited singlet state is provided by intersystem-crossing.

(iv) *Vavilov's law* says that the fluorescence spectrum and quantum yield in polyatomic molecules are independent of the wavelength of exciting radiation over the whole absorption spectrum. This only holds in condensed phases where fast vibrational relaxation establishes the Boltzmann distribution over the S_1 vibrational states. This distribution is only dependent on the temperature of medium and not on the initial vibrational energy. This law does not apply to vapours or molecules seeded in supersonic jets.

(v) *El-Sayed's rule* states that the rate of intersystem-crossing between different electronic states, ($n\pi^* \nleftrightarrow \pi\pi^*$), is two to four orders of mag-

[1]This is true for the vast majority of organic polyatomics, with notable exceptions such as azulene and the thiones, including XT, BPT and PT, which fluoresce from S_2.

nitude higher than that between similar configurations, ($\pi\pi^* \leftrightsquigarrow \pi\pi^*$, $n\pi^* \leftrightsquigarrow n\pi^*$).

(vi) *Energy gap law.* The magnitude of the energy gap, ΔE, between two electronic states involved in a radiationless transition strongly affects the very nature of the process. At $\Delta E > 10000$ cm^{-1} the so-called *statistical limit* of large molecules is usually reached. The radiationless transition rate falls off exponentially with increasing ΔE.

At $\Delta E < 5000$ cm^{-1} coupling between the two electronic states corresponds to the *intermediate case* of large molecules or the *small-molecule limit.* These coupling schemes will be studied further in Section 1.3

The above discussion refers primarily to molecules in condensed phases. In isolated gas phase molecules, such as molecules seeded in a supersonic jet, there is no mechanism for vibrational relaxation (VR) as shown in Figure 1.4 as there are no collisions during which VR can occur[2]. All processes therefore originate from states isoelectronic with the initial absorption state. This is shown in Figure 1.5.

1.3 Vibronic Coupling Schemes

Vibronic coupling is clearly very important in the spectroscopy of molecules. A description of the separation of the vibronic coupling into three distinct types is presented here as in Chapter 4 the spectroscopy of PT investigated is found to be of the intermediate coupling type. This is the least commonly observed vibronic coupling scheme, the classic example of which is the vibronic coupling of S_2 with S_1 in jet-cooled naphthalene [17], which exhibits a complex intermediate level structure in the $S_2 \leftarrow S_0$ excitation spectrum [26]. Some

[2]This is not strictly true but is used here for illustrative purposes only

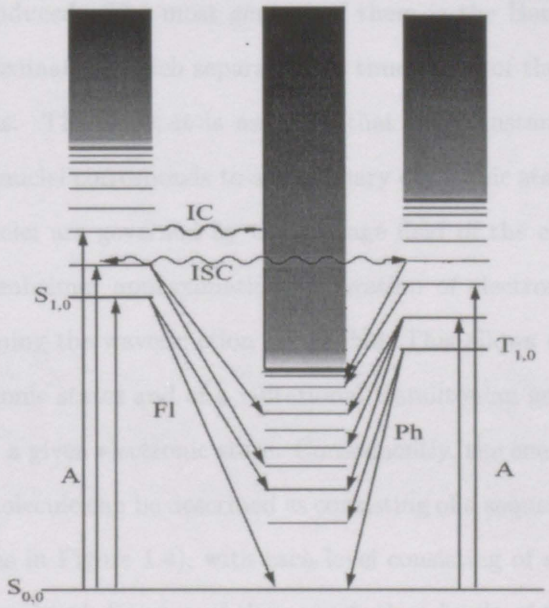


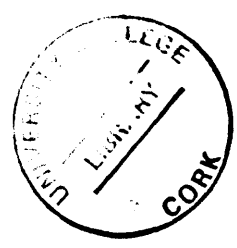
Figure 1.5: Jabloński Diagram for isolated molecules in a jet. **A:** Absorption. **Fl:** Fluorescence. **Ph:** Phosphorescence. **IC:** Internal Conversion. **ISC:** Intersystem Crossing.

familiarity with the terminology presented here is assumed in Chapter 4.

Consider an isolated molecule which has no interaction with any external field. The structure and the properties of this molecular system are determined by the motion of its electrons and nuclei and by their interaction. As the equations determining these interactions are inherently insoluble, the quantum-mechanical treatment of molecular structures in most cases can be carried out only if some simplifying approximations (which are physically justified) are introduced. The most general of them is the Born-Oppenheimer adiabatic approximation which separates the time-scales of the electronic and nuclear motions. Therefore, it is assumed that every instantaneous (fixed) position of the nuclei corresponds to a stationary electronic state, and the motions of the nuclei are governed by the average field of the electrons. Using the Born–Oppenheimer approximation, separation of electronic and nuclear motions in forming the wavefunction is possible. This allows us to envisage a notion of electronic states and of a vibrational Hamiltonian governing the nuclear motion in a given electronic state. Consequently, the energy spectrum of a polyatomic molecule can be described as consisting of a sequence of electronic energy levels (as in Figure 1.4), with each level consisting of a set of vibronic sublevels. A simplified diagram of the unperturbed levels of the zeroth-order Hamiltonian is shown in Figure 1.6. The total molecular Hamiltonian, H, can be expressed as

$$H = H_0 + V \tag{1.7}$$

where H_0 is the zeroth-order Hamiltonian and V is a perturbation. In the following discussion, the simplified zeroth-order approximation is used. It is assumed that there exits only one vibronic state ϕ_0 at energy E_0, connected by an allowed dipole transition with one of the lowest vibrational levels of an excited electronic state ϕ_s at energy E_s. This state ϕ_s is called an optically



bright or *doorway state*. In addition, there are a large number of vibrational sublevels ϕ_l and ϕ_m at energies E_l and E_m belonging to a different excited state (or the ground state). The E_l levels are nearly isoenergetic with the levels at E_s, while those at E_m are vibrationally relaxed. If the states at E_l and E_m belong to the ground state, S_0, or the first excited triplet state, T_1, then the processes that can occur are internal conversion and intersystem-crossing respectively. The states ϕ_l are called *dark states* as no optical transitions from or to these states are observed, and they are impossible to be photoexcited directly from the ground state as the transition dipole moment is negligibly small, $d_{0l} \approx 0$. It is further assumed that the interaction operator V only has the following non-zero matrix elements:

$$v_{sl} = \langle \phi_s | V | \phi_l \rangle \tag{1.8}$$

The level diagram in Figure 1.6 and the excitation process are characterised by several parameters; the interaction matrix element v_{sl}; the mean level spacing ρ^{-1} (ρ is the density of states per cm^{-1}); the level half-widths γ_s and γ_l; the detuning

$$\Delta = E_s - E_{l=0} \tag{1.9}$$

where $E_{l=0}$ is the level nearest to E_s; and the duration of the exciting monochromatic pulse τ_{pulse}. An important parameter also to be considered is

$$k_s = \frac{2\pi}{\hbar} v_{sl}^2 \rho_l \tag{1.10}$$

where k_s can have the meaning of a transition rate constant or be merely considered as a formal quantity and ρ_l is the density of states at energy E_l. Depending on the specific relationships between these parameters, of which ρ_l, the density of dark states, is the most important, three important clas-

sifications can be made: the small molecule limit, the intermediate case and the statistical limit of large molecules. A scheme depicting the relationships between the above parameters and the three mentioned limiting cases is shown in Figure 1.7. Small molecules are characterised by large mean separations between vibrational–rotational levels E_l. With γ being the corresponding level width, the basic condition for the **small molecule limit** is

$$\gamma \ll \frac{1}{\rho_l} \tag{1.11}$$

The mean separation between level E_l decreases rapidly with increasing number of atoms. The limiting case of large molecules is divided into the statistical limit and the intermediate case. The **statistical limit of large molecules** is characterised by the following condition:

$$\gamma \gg \frac{1}{\rho_l} \tag{1.12}$$

This above condition needs to be adapted as it has been noted [27] that effective states play a major role in the statistical limit. Effective states are introduced to eliminate such final states to which transitions are actually forbidden because of too low values of the matrix elements v_{sl}. Equation 1.12 becomes

$$\gamma \gg \frac{1}{\rho_{\text{eff}}} \tag{1.13}$$

This important role of effective states means that all states are effective, i.e. $v_{sl} = v_{\text{eff}}$ and $\rho_l = \rho_{\text{eff}}$. Therefore, replacing γ_l and ρ_l with the respective parameters γ and ρ_{eff}, one obtains the statistical limit in the form corresponding to that described in Figure 1.7:

$$\gamma \gg \frac{1}{2}k_s + (2\pi\rho_{\text{eff}})^{-1} \tag{1.14}$$

where k_s is given by Equation 1.10. In the weak coupling limit, $\nu_{\text{eff}} \ll 1/\rho_{\text{eff}}$, the first term on the right hand side of Equation 1.14 is small compared to the second and reduces to Equation 1.13. The **intermediate case of large molecules** is characterised by

$$\frac{1}{\rho_{\text{eff}}} \gg \gamma \gg \frac{1}{\rho_l}. \tag{1.15}$$

Finally, the number of states in an energy interval, N, is given by

$$N = 2\pi^2 v_{sl}^2 \rho_l^2 \tag{1.16}$$

1.4 Outline of Thesis

The previous section gave background information on the photophysics of the thiones, symmetry properties and vibronic coupling schemes. The experimental systems and procedures are detailed in Chapter 2. The $T_{1,0} \leftarrow S_0$ phosphorescence excitation spectrum of jet-cooled xanthione (XT) is examined in Chapter 3. The phosphorescence excitation spectrum of 4-*H*-1-pyrane-4-thione (PT) is investigated in Chapter 4. Finally, Chapter 5 presents computational work on the $T_{1z,0}$ line of PT.

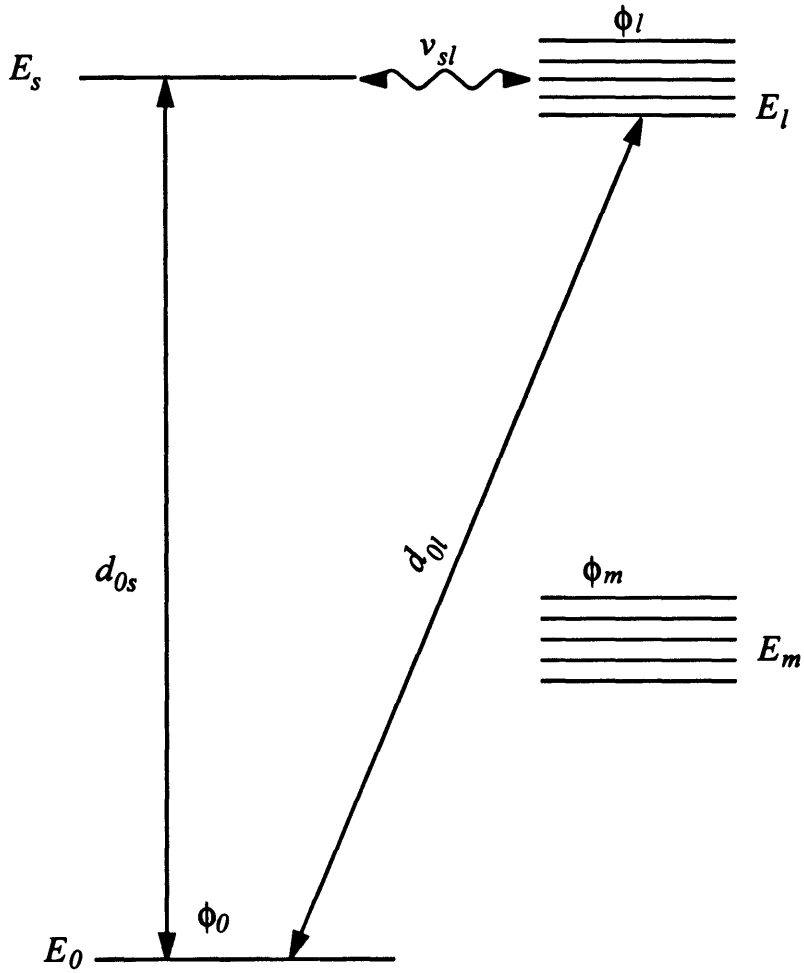


Figure 1.6: Simplified Jabloński Diagram

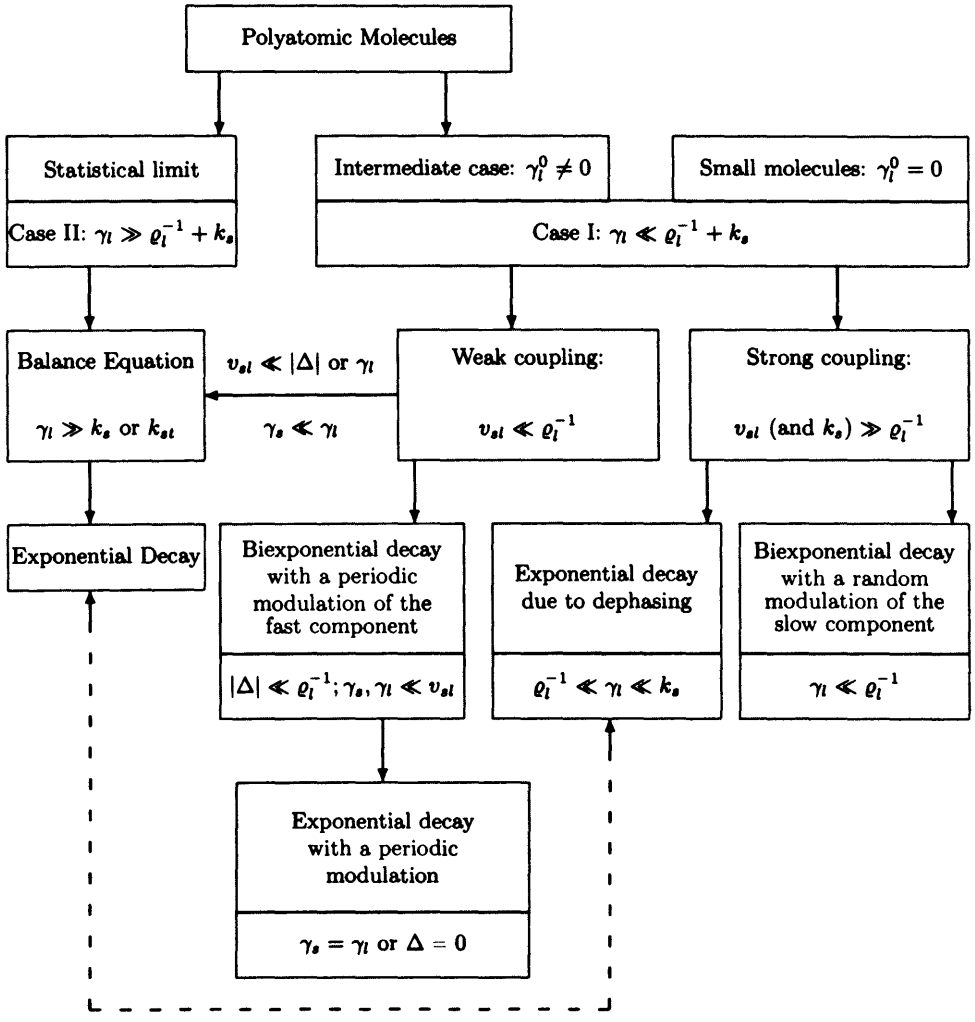


Figure 1.7: Schematic illustrating the three limiting cases in luminescence kinetics and the relationships between various parameters. Constants 2π and h are omitted in the relations given in the figure to aid with clarity.

Bibliography

[1] D.C. Moule and A.D. Walsh. *Chem. Rev.*, 75:67, 1975.

[2] G.N. Lewis and M. Kasha. *J. Am. Chem. Soc.*, 66:2100–2116, 1944.

[3] G.N. Lewis and M. Kasha. *J. Am. Chem. Soc.*, 67:994–1003, 1945.

[4] D.M. Burland. *J. Chem. Phys.*, 75(6):403–411, 15 September 1981.

[5] M.R. Taherian and A.H. Maki. *Chem. Phys.*, 68:179–189, 1982.

[6] M.J. Petrin, S. Ghosh, and A.H. Maki. *Chem. Phys.*, 120:299–309, 1988.

[7] M. Szymański and R.P. Steer. *J. Phys. Chem.*, 96:8719–8728, 1992.

[8] M. Ludwiczak, H.K. Sinha, and R.P. Steer. *Chem. Phys. Lett.*, 194(3):196–202, 1992.

[9] H.K. Sinha and R.P. Steer. *Chem. Phys. Lett.*, 211(4,5):397–402, 1993.

[10] H.K. Sinha, L. Chantranupong, and R.P. Steer. *J. Mol. Spectrosc.*, 169:302–314, 1995.

[11] A.A. Ruth, F.J. O'Keeffe, M.W.D. Mansfield, and R.P. Brint. *J. Phys. Chem. A*, 101(42):7735–7741, 1997.

[12] A.A. Ruth, F.J. O'Keeffe, R.P. Brint, and M.W.D. Mansfield. *Chem. Phys.*, 217:83–98, 1997.

[13] A.A. Ruth, T. Fernholz, R.P. Brint, and M.W.D. Mansfield. *Chem. Phys. Lett.*, 287:403–411, 1998.

[14] A. Maciejewski and R.P. Steer. *Chem. Rev.*, 93:67–98, 1993.

[15] M. Mahaney and J.R. Huber. *J. Mol. Spectrosc.*, 87:438–448, 1981.

[16] M. Baba, T. Kamei, M. Kiritani, S. Yamauchi, and N. Hirota. *Chem. Phys. Lett.*, 185(3,4):354–358, 1991.

[17] S.M. Beck, D.E. Powers, J.B. Hopkins, and R.E. Smalley. *J. Chem. Phys.*, 73(5):196–202, 1 Sept 1980.

[18] J. Hertzberg and B. Nickel. *Chemical Physics*, 132:235–242, 1989.

[19] A. Maciejewski and R.P. Steer. *Chem. Rev.*, 93:67–98, 1993. and references therein.

[20] H. Eisenberger and B. Nickel. *J. Chem. Soc. Faraday Trans.*, 92:733, 1996.

[21] H. Eisenberger, B. Nickel, A.A. Ruth, and R.P. Steer. *J. Chem. Soc. Faraday Trans.*, 92:741, 1996.

[22] W.M. Flicker, O.A. Mosher, and A. Kupperman. *Chem. Phys. Lett.*, 57:183, 1978.

[23] P.G. Burton, S.D. Peyerimhoff, and R.J. Buenker. *J. Chem. Phys.*, 73:83, 1982.

[24] M. Szymanski, R.P. Steer, and A. Maciejewski. *Chem. Phys. Lett.*, 135(3):243–248, 3 April 1987.

[25] G. Herzberg. *Molecular Spectra and Molecular Structure*, volume III. Electronic Spectra and Electronic Structure of Polyatomic Molecules. Van Nostrand Reinhold Company, 1966.

[26] J. Wessel and D.S. McClure. *Mol. Cryst. Liq. Cryst.*, 58:121–153, 1980.

[27] E.S. Medvedev and V.I. Osherov. *Radiationless transitions in Polyatomic Molecules*, volume 4. Springer, Berlin, 1995.

Chapter 2

Experimental Details

Two spectroscopic methods were employed in this work and are detailed below. The laser induced phosphorescence method is described in Section 2.1 and the cavity ring down method is described in Section 2.2. These details apply to the majority of the experiments performed, and where different the changes will be detailed in the text.

2.1 Phosphorescence Excitation

The experimental apparatus is illustrated in Figure 2.1. The sample was seeded into a carrier gas and was then injected into the vacuum chamber by means of a pulsed valve (Section 2.1.3). The sample was excited by an intersecting light pulse from a tunable dye laser (Section 2.1.1). Light emitted by the sample molecules was collected by a mirror and lens system and focused onto the cathode of a photomultiplier tube, (PMT). The output from this PMT was connected to a photon counter which was interfaced to a computer. A portion of the input light reflected off the entrance window was collected by a second PMT or by a Molectron JS-09 Joulemeter. The output from these devices was connected to a LeCroy 9410 Oscilloscope and was used as a reference

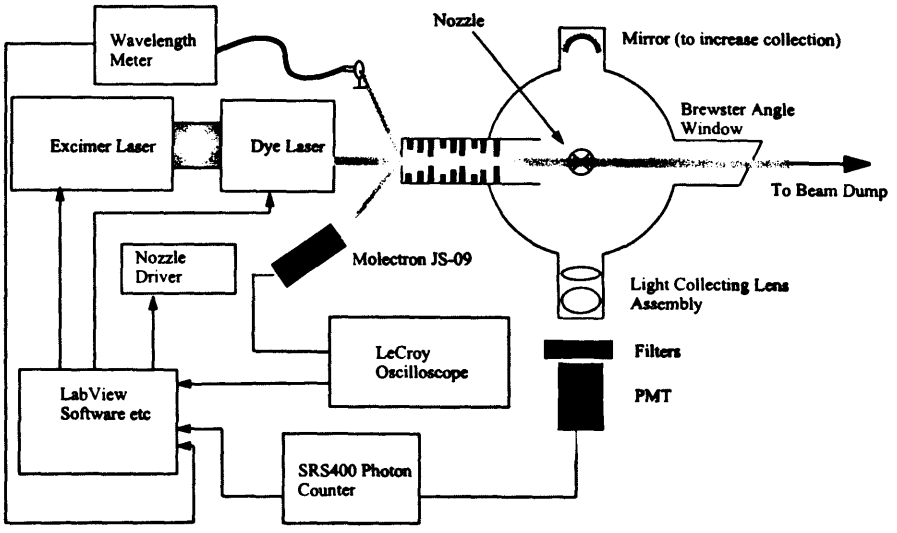


Figure 2.1: Phosphorescence Excitation Experimental Setup

measurement. Another portion was reflected off one of the beam steering prisms and was coupled into a wavelength meter for exact energy measurement. See Section 2.1.2 for details. A programme written using National Instruments LabView © software controlled the whole experiment.

2.1.1 Laser System

The sample in the jet was excited by an excimer-pumped dye laser. A XeCl excimer laser (Lumonics EX-700) with an output at 308 nm is the pump source for the dye laser. Operating at 38kV and 8Hz, typical pump energies of $\sim$ 300mJ per pulse fwhm $\simeq$ 15ns were achieved.

The dye laser used was a Lumonics HyperDYE-300. Several dyes were used to cover the various excitation ranges. Coumarin 153, rhodamine 6G, rhodamine B, rhodamine 101 and DCM covered the dye range 680–540 nm for Xanthione. QUI, DMQ, BMQ and butyl-PBD were used for the range 368–342 nm for Pyranthione. These dyes were obtained from Coherent Ltd. Pulse energies varied over the dyes and their dye ranges with typically 10–15 mJ

per pulse at maximum dye efficiency. These energy variations were taken into account when correcting the subsequent data, Section 2.1.5

2.1.2 Wavelength Calibration

The wavelength of the output from the dye laser was monitored by the Wavelength Meter WS-7 supplied by Angstrom Ltd. of the Siberian Institute of Metrology, Novosibirsk, Russia.

A back reflection from one of the steering-prisms was coupled into a fibre-optic coupling lens system. This optic fibre is in turn coupled into the optical unit. This unit is designed for obtaining the laser's emission interference pattern by means of five Fizeau interferometers on two linear photodiode arrays. The first photodiode array registers the interference pattern from interferometers 1–4, the second registers the interference pattern from interferometer 5. The signal from the linear photodiode arrays, housed in the optical unit, is transmitted via a serial communication cable to an ADC board on an IBM compatible PC. The software installed on the computer calculates the wavelength by comparison of periods and phases of the laser's interference pattern with the interference pattern of the reference laser of a known wavelength.[1] As this calculation consumes significant computing capacity, a single computer is dedicated to this process. The value of the wavelength, displayed on the monitor, is transferred to the control computer via an RS232 cable.

The wavelength meter works for both CW and pulsed lasers and over a range of 300–1100 nm. Two different optic fibres were supplied with the WS-7. A 10 m optic fibre for ranges 450–725 nm and 700–1100 nm, and a 5 m fibre for the 300–475 nm range. It also allows two modes of measurement: wide line, giving an accuracy of ± 0.002 nm or ± 0.02 cm^{-1}; and narrow line, giving

[1]The WS-7 Wavelength Meter was calibrated regularly with a stabilised He-Ne laser at 632.99100 nm.

an accuracy of ±0.0001 nm or ±0.001 cm^{-1}, measured at 1000nm. These are well within the line width of the dye laser of 0.3 cm^{-1}.

2.1.3 Pulsed Nozzle System

A circular pulsed nozzle (General Valve Corporation, 'Iota One' nozzle driver) with an orifice of 0.8 mm generated the supersonic jet expansion. The valve unit was embedded in a tight-fitting copper block to ensure maximum thermal contact. The valve unit consists of a coil assembly, armature, poppet and nozzle flange. The poppet sits in the armature and when the coil is energised the armature is pulled up into the coil assembly and the valve is opened. When the coil is de-energised a spring returns the armature and poppet to their original position, closing the valve. The top of the valve unit was connected to a brass cylinder with a SwageLok fitting. This cylinder was also tight-fitting. Inside this cylinder the molecular sample was held in a glass tube with a glass frit. These are shown in Figures 2.2 and 2.3.

A Fuji Electronics PID (proportional-integral-derivative) controller was used to maintain the copper block, along with the valve unit and sample holder, at the required temperature. The k-type thermocouple and two resistive heater elements were placed in the block close to the nozzle to sense the temperature and to provide heating. The top of the brass cylinder was connected to a gas reservoir, in which the carrier gas, (5.0 grade Helium), was kept. A manometer with a resolution of 20 mbar was attached to the reservoir. The maximum backing pressure was 3 bar, due to pumping limitations.

The vacuum was maintained at $\sim 10^{-6}$ mbar (with the molecular jet switched off) by means of an Edwards Diffstak diffusion pump backed by an Edwards 8 rotary pump. This pumping arrangement is of sufficient capacity to keep the vacuum in the chamber at $\sim 1 \times 10^{-4}$ mbar under the following

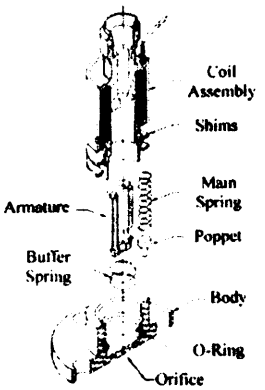


Figure 2.2: General Valve Corporation "Iota One" Pulsed Nozzle

conditions: 8 Hz jet pulse repetition rate; 1 ms jet pulse length; 1000 mbar carrier gas pressure. For higher pressures a lower pulse rate was used.

2.1.4 Detection System

The phosphorescent emission from the excited molecules in the jet was collected by a pair of quartz lenses and directed onto the photocathode of the photomultiplier tube (PMT), as shown in Figure 2.1. A mirror opposite the observation side enhanced the photon collection. The first lens was positioned such that its focal point coincided with the zone of excitation, the intersection of the laser beam and the jet, $\sim$ 13 mm below the nozzle. A quartz window, together with optional filters (coloured glass and/or interference filters, Schott GmbH and Andover Corp. respectively) were placed between the lenses and the PMT.

A Phillips X2254B photomultiplier was used in all of these experiments. It was operated at a negative cathode potential of $\sim$ 1600V in photon counting mode and the output was connected to a Stanford Research Systems SR400

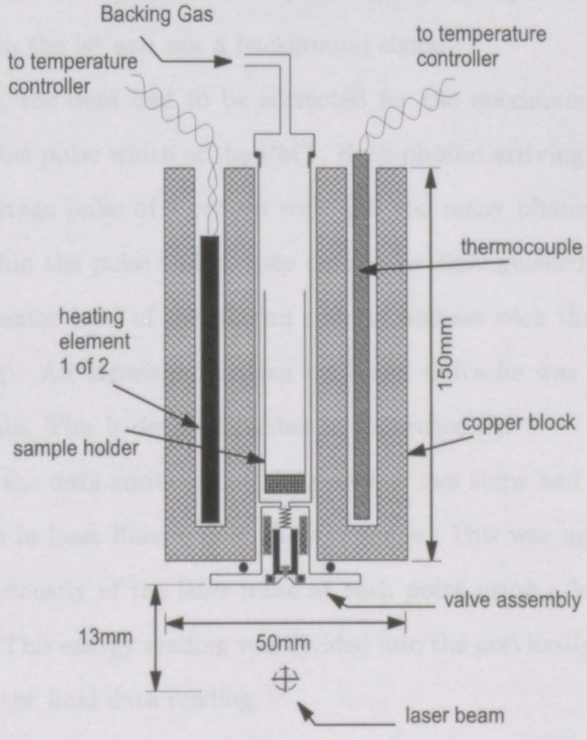


Figure 2.3: Jet valve unit embedded in the copper block

photon counter. The SR400 was connected to the control computer by GPIB from which all parameters, e.g. width and delay of measurement gate, could be varied.

2.1.5 Data Correction

In the case of phosphorescence excitation, the data was corrected in various ways.

Firstly, each data point reading was determined by two measurements.

The laser was fired with and without the jet turned on. The latter counts were subtracted from the former counts to allow for detector noise and scattered light. The value of 'corrected' counts was then used in further correction steps. The corrected counts give a noisier spectrum, but do represent the signal due to material in the jet and not a background signal.

Secondly, the data had to be corrected for the maximum possible count rate due to the pulse width of the PMT. Each photon arriving on the cathode creates a voltage pulse of a certain width. If too many photons arrive at the cathode within the pulse width, they cannot be distinguished. In most cases the discriminator level of the photon counter was set such that there was no pulse overlap. An algorithm written by Frank O'Keeffe was used to correct the count rate. This is detailed further in Reference [1].

Thirdly, the data corrected by the previous two steps had to be corrected for variation in laser fluence over the dye range. This was achieved by measuring the intensity of the laser pulse at each point using a Molectron JS–09 joulemeter. This energy reading was divided into the previously corrected data to arrive at the final data reading.

2.2 Cavity Ring-down Spectroscopy

Cavity Ring-down spectroscopy (CRDS) is a relatively new ultra-sensitive laser absorption technique. Compared to conventional absorption techniques CRDS, or cavity ring-down laser absorption spectroscopy (CRLAS) as it is also known, has numerous advantages. These include extremely long effective path lengths and immunity to shot-to-shot variations in laser intensity. This technique is detailed in the following section.

2.2.1 Experimental Principles

Conventional absorption spectroscopic techniques are based on the Beer–Lambert Law, Eq. 2.1

$$I(\lambda) = I_0 \exp[-\alpha(\lambda)Cl] \tag{2.1}$$

This relates the intensities of radiation before (I_0) and after (I) passing through a sample of concentration C and path length l. The value α is the wavelength dependent absorption coefficient. The molar absorption coefficient (or extinction coefficient) $\varepsilon = \alpha/\ln 10$ is commonly encountered. The product $A = \varepsilon Cl$ is known as the "absorbance" or "optical density" of the sample.

Conventional absorption spectroscopy measures I_0 and I and is quite satisfactory when the samples involved have reasonably large absorption coefficients. However, for weak absorption, the main problem encountered is the very small change in transmitted intensity. This is the case in many gas-phase and supersonic-jet absorption measurements.

CRDS differs from conventional absorption spectroscopy in that the rate of change of intensity is measured as opposed to measuring the change of the magnitude of intensity. This method is immune to variations in the incoming radiation intensity and absorption in the order of one part in 10^7 per pass can be measured. The following discussion is based on the apparatus shown in Figure 2.4 in which an optical cavity is formed by two highly reflecting mirrors of reflectivity R. In an empty cavity, the intensity measured exiting through the exit mirror is I_0. Similarly,

$$I_1 = I_0R^2 \quad I_2 = I_0R^4 \cdots I_n = I_0R^{2n} \tag{2.2}$$

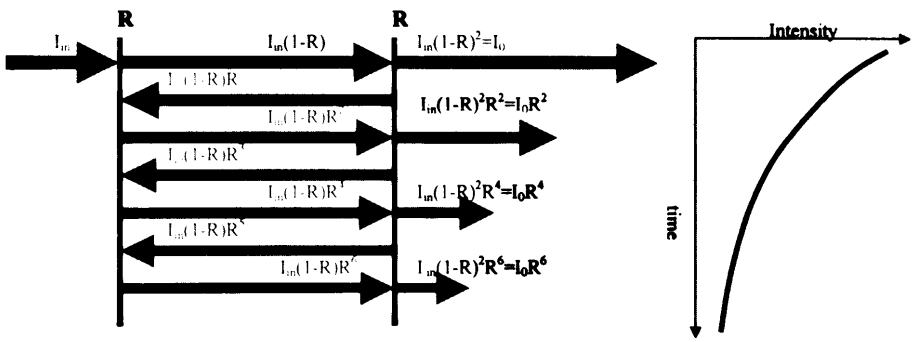


Figure 2.4: Laser light passing through an optical cavity. On the left hand side, the attenuation in intensity per pass is described. On the right hand side is the attenuation in intensity as a function of time

where $1, 2 \cdots n$ are the number of return trips within the cavity.

$$\begin{aligned} I_n &= I_0 R^{2n} \\ &= I_0 \exp[2n \ln R] \end{aligned} \tag{2.3}$$

Replacing the number of round–trips n by the time t,

$$t = n\frac{2d}{c}$$

where d is the mirror separation and c is the speed of light,

this then gives

$$I_t = I_0 \exp\left[\frac{c \ln R}{d} t\right] \tag{2.4}$$

Comparing this to a characteristic exponential equation

$$I_t = I_0 \exp\left[\frac{-t}{\tau}\right]$$

the characteristic decay time, called the cavity ring–down time is given by

$$\tau_{\text{crd}}^{\text{empty}} = \frac{d}{c|\ln R|} \approx \frac{d}{c(1-R)} \tag{2.5}$$

This is the time for the intensity to decay to $1/e$ of its original value. The rate of decay is $(\tau_{\text{crd}}^{\text{empty}})^{-1}$.

As can be seen the ring–down time is governed solely by the mirror separation d and the mirror reflectivity R. By scanning the wavelength and measuring $\tau_{\text{crd}} = \tau_{\text{crd}}(\lambda)$ the wavelength dependence of the mirror reflectivity can be determined. These losses are characteristic of the empty cavity.

If a sample gas is introduced into the cavity and the wavelength of light within the cavity matches an absorption of the gas an additional mechanism for the loss of light exists. This additional loss mechanism increases the rate of intensity decay and hence the ring down time decreases.

This additional absorption of $\sim \exp(\alpha d)$ per pass must be taken into account in the above description of an empty cavity. Now, the initial intensity exiting the cavity is

$$I_0' = I_0 \exp(-\alpha d)$$

and similar to the empty cavity

$$I_1 = I_0' R^2 \exp(-\alpha d)^2 \; I_2 = I_0' R^4 \exp(-\alpha d)^4 \cdots I_n = I_0' R^{2n} \exp(-\alpha d)^{2n}$$

$$I_n = I_0' \exp[2n(\ln R - \alpha d)] \tag{2.6}$$

Similar to Equation 2.4 the time–dependent intensity for this situation is given by

$$I_t = I_0' \exp\left[\frac{c \ln R}{d} t - \alpha c t\right] \tag{2.7}$$

UNIVERSITY COLLEGE LIBRARY CORK

and the ring–down time is given by

$$\tau_{\text{crd}}^{\text{full}} = \frac{d}{c(|\ln R| + \alpha d)} \tag{2.8}$$

It can be seen from Equations 2.5 and 2.8 that

$$(\tau_{\text{crd}}^{\text{full}})^{-1} = \frac{c|\ln R|}{d} + \alpha c$$

$$(\tau_{\text{crd}}^{\text{empty}})^{-1} = \frac{c|\ln R|}{d}$$

and therefore

$$\alpha = \frac{1}{c}\left[(\tau_{\text{crd}}^{\text{full}})^{-1} - (\tau_{\text{crd}}^{\text{empty}})^{-1}\right] \tag{2.9}$$

If the empty cavity ring–down time, $\tau_{\text{crd}}^{\text{empty}}$, is known, measurement of the decay rate of the light intensity as the laser wavelength is scanned gives the absorption coefficient for each laser wavelength and hence the absorption spectrum is produced. It should be noted that value α obtained is the absorption coefficient and the number density (or concentration) of the absorbing species is required in order to obtain the absorption cross–section σ.

Sensitivity of CRD

The fractional loss per round trip,

$$\delta I = \frac{I_0 - I}{I_0}$$

is used to specify the sensitivity of CRD. According to the Beer–lambert Law (Eq. 2.1), the absorption for a single pass through a cavity of length d is

$$I = I_0 \exp\{-\alpha d\} \tag{2.10}$$

where $\alpha = \sigma C$. For very small absorbances per single pass $\alpha d \ll 1$ and therefore

$$\delta I = \frac{I_0 - I}{I_0} \approx \alpha d \tag{2.11}$$

Zalicki and Zare [2] have shown that in terms of change of ring–down time, $\Delta\tau = \tau - \tau'$, upon tuning to an absorption feature[2]

$$\alpha d = (1 - R)\frac{\Delta\tau}{\tau'} \tag{2.12}$$

Therefore,

$$\delta I = (1 - R)\frac{\Delta\tau}{\tau'} \tag{2.13}$$

Thus the sensitivity of CRD is limited by the reflectivity R of the mirrors and the minimum detectable change in ring–down time $\Delta\tau$.

The above discussion only holds true if the absorption satisfies the Beer–Lambert law. This requires that the absorption linewidths are greater than the linewidth of the laser light within the cavity. This requirement ensures that all of the frequencies contained within the laser pulse are attenuated by absorption when the laser is tuned to the central frequency of the absorption line. The Beer–Lambert law can only be satisfied if the pulse duration, t_p, is greater than T_2, the lifetime of the upper state.

2.2.2 Apparatus

The experimental apparatus for this section is shown in Figure 2.5. The vacuum chamber is formed by replacing the entrance and exit windows of the phosphorescence excitation chamber with two highly reflecting mirrors (Reflectivity $R > 99.99\%$ over a specified wavelength). The output from the dye

[2]Here τ and τ' correspond to τ^{empty} and τ^{full}

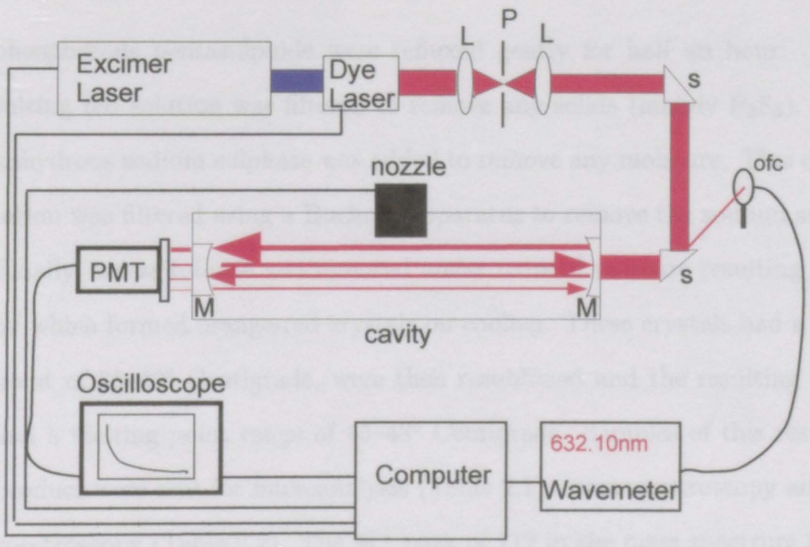


Figure 2.5: Cavity Ring–down apparatus. L=lens, P=pinhole, s=beam steering prism, m=highly reflecting mirror, ofc=optic fibre coupler.The lens-pinhole-lens combination forms a spatial filter and reduces ASE.

laser is coupled into the cavity through the back of one mirror, intersects the seeded-jet expansion and the rate of change of intensity emerging through the other mirror is monitored with a PMT. The output from this tube is connected to one channel of an oscilloscope which is interfaced with a computer. A portion of the reflected light from the front window is coupled into another PMT in order to measure the power of the laser. The laser, jet and wavelength calibration systems are the same as the previous method (see Sections 2.1.1, 2.1.3 and 2.1.2).

2.3 Synthesis of 4-*H*-Pyrane-4-thione

As 4-*H*-Pyrane-4-thione, (PT), is not available from commercial suppliers, it had to be synthesised in the laboratory. The following synthesis is from a brief description by MacDonald et al, [3].

4g of 4-*H*-Pyrane-4-one, (96g/mol), 100mls of dry toluene and excess of

phosphorous pentasulphide were refluxed gently for half an hour. The resulting red solution was filtered to remove any solids (mainly P_2S_5). To this anhydrous sodium sulphate was added to remove any moisture. This dried solution was filtered using a Buchner apparatus to remove the sodium sulphate. Finally, excess toluene was removed under reduced pressure resulting in a red oil which formed orange-red crystals on cooling. These crystals had a melting point of 35–42° Centigrade, were then resublimed and the resulting product had a melting point range of 45–48° Centigrade. Samples of this resublimed product were sent for microanalysis (Table 2.1), mass spectroscopy and NMR spectroscopy (Table 2.2). The M^+ peak of 112 in the mass spectrum suggests that PT was successfully produced. The ^{13}C NMR of PT shows three peaks

Analysis required	theory %	found %
C	53.52	53.42
H	3.60	3.60
S	28.61	28.23

Table 2.1: Microanalysis of synthesised PT

at δ equals 128.303 ppm, 148.055 ppm and ~203 ppm. The peak at $\delta = \sim 203$ ppm is due to the thiocarbonyl carbon. In the carbonyl precursor the carbonyl carbon has a peak at $\delta = 178.06$ ppm. According to Pedersen et al. [4] there is a function describing the relation between the chemical shifts of C=S and C=O :

$$\delta_{C=S} = 1.57 \times \delta_{C=O} - 71.45$$

This gives a value of 208.1 ppm for the chemical shift of the thiocarbonyl carbon. Although the measured value is 203 ppm, this shows that the carbonyl precursor has indeed been converted to the thiocarbonyl.

UNIVERSITY COLLEGE LIBRARY CORK

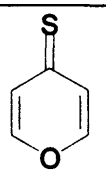
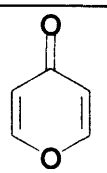
	 4-*H*-Pyrane-4-thione (PT)	 4-*H*-Pyrane-4-one
^{13}C NMR δ/ppm†	128.303 148.055 ~203	118.57 157.81 178.06
^{1}H NMR δ/ppm†	7.17 7.57	~ 6.25 ~ 8.15

Table 2.2: NMR spectra of synthesised PT compared to the carbonyl precursor. †Chemical shift values for 4-*H*-Pyrane-4-one were obtained from Aldrich FTIR Atlas

2.4 Supersonic Jet Expansion Characteristics

Most spectral lines are broadened to some extent by pressure-broadening, Doppler-broadening, collisional broadening and so on. These broadening processes lead to complicated spectra and difficulties in assigning spectral lines. Ideally, a sample of molecules under investigation should be at a temperature which is low enough to prevent thermal dissociation and to produce only as many rotational and vibrational lines as can be separately identified. Also, the medium in which the sample is supported must not introduce undesirable changes and complications in the spectrum. An ideal spectroscopic sample would be an ensemble of molecules, all in a particular and well-defined quantum state (usually the lowest energy allowed state) travelling in free space with a narrow velocity distribution, and at a sufficiently low density so that intermolecular interactions are unimportant. Such an ideal sample source can be generated using a supersonic jet expansion.

Use is made of the fact that under hydrodynamic flow conditions, the random motion of molecules is converted into a directed mass flow (with velocity u). This conversion of random motion to directed mass flow causes the trans-

lational temperature to decrease and as the speed of sound, a, is given by

$$a = \left(\frac{\gamma kT}{m}\right)^{\frac{1}{2}}$$

where

$$\gamma = \frac{C_p}{C_v}$$

and

$$C_p \text{ and } C_v$$

are the specific heats of the gas at constant pressure and volume respectively, the speed of sound decreases and the Mach number, $M \equiv u/a$, increases. A large Mach number ($M \gg 1$) indicates a well-developed supersonic expansion, with the consequent benefits of cooling and isolation of the carrier gas atoms, and more importantly, of the seeded molecules also. The Mach number, M, is an important parameter as most other thermodynamic properties of an isentropic expansion[3] can be described in terms of it. According to Miller [5], the centreline Mach number can be expressed in terms of

$$M = A \cdot \left(\frac{x - x_0}{D}\right)^{\gamma-1} - \frac{1}{2}\left(\frac{\gamma+1}{\gamma-1}\right)\left[A \cdot \left(\frac{x - x_0}{D}\right)^{\gamma-1}\right]^{-1} \qquad (2.14)$$

where D is the diameter of the nozzle used, x_0 and A are empirical parameters depending on the nature of the expansion gas only, i.e. whether it is monatomic, diatomic (or linear polyatomic), or non-linear polyatomic. Values of x_0 and A for all cases are given in Table 2.3. As only noble carrier gases were used in the experiments described in this thesis, the values of $A = 3.26$ and $x_0 = 0.075D$ apply. Note that Equation 2.14 is only valid at positions further from the nozzle than a minimum distance $x_{\min}$. For a monatonic gas, $x_{\min} = 2.5D$ or

[3]Under reversible flow conditions an expansion is isentropic i.e. pV^γ = constant

UNIVERSITY COLLEGE Library CORK

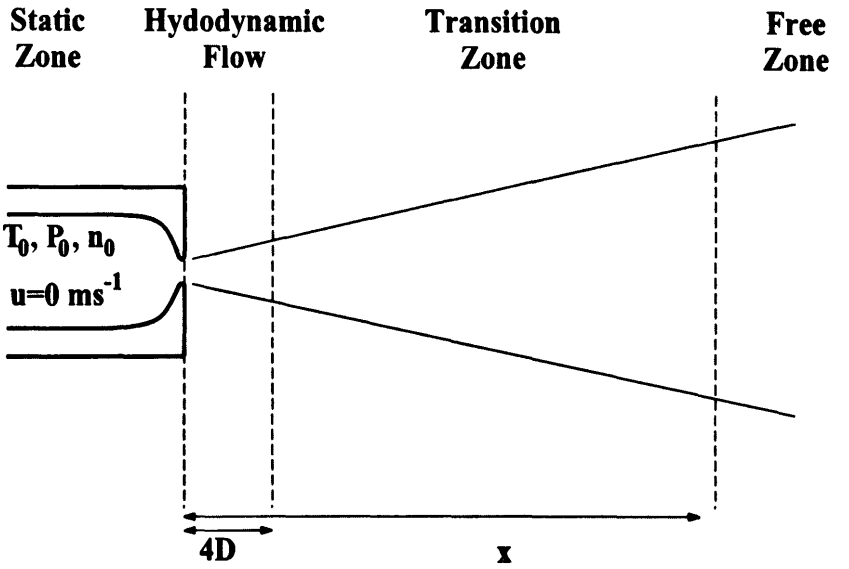


Figure 2.6: Schematic of a supersonic jet expansion. The four zones indicated are: the static zone (before expansion at 'high' pressure) which is simply a static cell; hydrodynamic flow region in which the gas rapidly cools as it expands adiabatically; the transition region in which the gas molecules have cooled to a few Kelvin, but still undergo relatively frequent collisions and continue to accelerate; and the free zone in which the molecules have reached terminal velocity and are effectively isolated.

2 mm in this thesis as in most experiments presented here $D = 0.8$ mm.

One may use the isentropic equation of state of an ideal gas to describe the temperature, T, pressure, P, and density, n, of the beam as a function of the Mach number, M. The isentropic equations of state assume isentropic flow, ideal gas behavior, constant γ and continuum flow. The (translational) temperature T at a given position in the jet is given by

$$\left(\frac{T}{T_0}\right) = \left(1 + \frac{\gamma - 1}{2} M^2\right)^{-1} \tag{2.15}$$

where T_0 is the temperature of the carrier gas in the reservoir. Similarly, the

Gas	γ	A	x_0/D	x_{min}/D
monatomic	5/3	3.26	0.075	2.5
diatomic/linear polyatomic	7/5	3.65	0.4	6
non-linear polyatomic	8/6	3.16	0.85	4

Table 2.3: The values of A, x_0 and x_{min} required to calculate the centreline Mach number in a supersonic jet expansion using Equation 2.14 according to Ref [5].

pressure, P, and the particle density, n are given by

$$\left(\frac{P}{P_0}\right) = \left(\frac{T}{T_0}\right)^{\frac{\gamma}{\gamma-1}} \tag{2.16}$$

$$= \left(1+\frac{\gamma-1}{2}M^2\right)^{-1}$$

and

$$\left(\frac{n}{n_0}\right) = \left(\frac{T}{T_0}\right)^{\frac{1}{\gamma-1}} \tag{2.17}$$

$$= \left(1+\frac{\gamma-1}{2}M^2\right)^{-\frac{1}{\gamma-1}} \tag{2.18}$$

where P_0 and n_0 are the stagnation pressure and particle density in the reservoir before expansion, respectively. A further quantity that should be mentioned when describing an adiabatic expansion is u, the average speed of neighbouring particles in a given region of the jet is given by

$$u = M\sqrt{\frac{\gamma k_B T_0/m_a}{1+\frac{\gamma-1}{2}M^2}} \tag{2.19}$$

where m_a is the mass of a carrier gas atom or molecule.

These equations only hold in the region where collisions still occur, the transition region. As there are a finite number of collisions, terminal values for the above equations are arrived at a distance in the jet where no collisions

occur, in the free zone. From equations 2.14–2.19, it is clear that, in the limit as $x \rightarrow \infty$, $M \rightarrow \infty$ and $T \rightarrow 0$ K. For a monatomic carrier gas, the terminal velocity is given by

$$u^{\infty} = \lim_{x \rightarrow \infty} u = \sqrt{\frac{5k_B T_0}{m_a}} \tag{2.20}$$

The most important effects of the jet expansion in spectroscopic applications are (i) the reduction of temperature of the gas without condensation as its speed increases and (ii) the isolation of the molecules from their molecular environment. If one compares the velocity distribution of molecules in a static cell to that of molecules in a jet (Figure 2.7), point (i) is illustrated quite clearly. The translation temperature of a gas is determined by the width of the velocity distribution and not by the position of the peak. A narrow velocity distribution corresponds to a lower translational temperature.

Seeded Jet Expansions

When a jet is seeded with molecules three non-equilibrium effects need to be addressed — diffusive separation, non-continuum velocity slip and temperature slip.

According to Anderson [6], under the operating conditions of most free-jet expansions, diffusive separation is negligible and will not be dealt with any further here.

Heavier species tend to lag behind the lighter species in velocity in the accelerating portion of the jet flow. This diffusive effect gives rise to velocity slip. For a monatomic carrier gas seeded with a fraction η of molecules, the

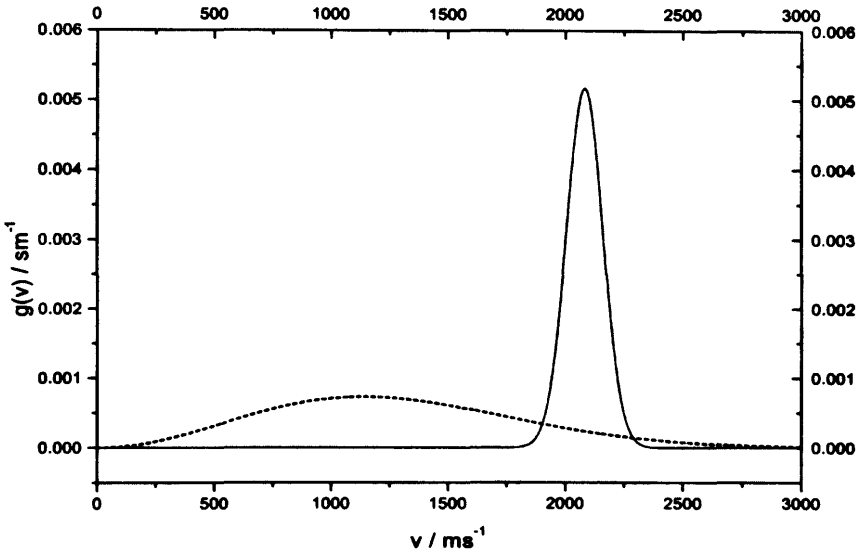


Figure 2.7: Velocity distribution of helium atoms in the reservoir at 313 K (dashed curve) and in a supersonic molecular beam at 13 mm downstream of a nozzle with $D = 0.8$ mm (solid curve). Both distributions are normalised to give $\int_0^\infty g(v)dv = 1$.

terminal velocity u_m^∞ of the molecules is given by [5]:

$$u_m^\infty = \sqrt{\frac{5k_B T_0}{\eta m_m + (1-\eta)m_a}} \tag{2.21}$$

where m_m and m_a are the masses of the seed molecules and carrier gas atoms respectively. For a sufficiently lightly seeded jet, velocity slip can be made insignificant, and Equation 2.21 reduces to $u_m^\infty = \sqrt{5k_B T_0/m_a} = u^\infty$, Equation 2.20.

The effect of temperature slip is very important. For the various degrees of freedom of the particles in the jet to reach a thermal equilibrium large numbers of inter-particle collisions are required. As the jet expands, a point is reached whereby the particle density is so low that collisions cease and the distributions of the various degrees of freedom are 'frozen' and do not change.

Hence, the jet cannot be characterised by a single temperature at any location outside the reservoir. Four[4] temperatures are required to describe the energy distribution: translational temperatures $T_{trans(a)}$ and $T_{trans(m)}$ of the atoms and molecules respectively; rotational temperature $T_{rot(m)}$ of the molecules; and vibrational temperature $T_{vib(m)}$ of the molecules. Little quantitative experimental data is available regarding the cross-section for collisional energy transfer between rare-gas atoms and large aromatic molecules. However, this can be explained qualitatively. Firstly, transfer of translational kinetic energy is most rapid between particles of similar mass, and so $T_{trans(a)} < T_{trans(m)}$. This explains why heavier noble gases provide more efficient cooling. Secondly, as the rotational and vibrational energies of the molecule are quantised, the cross-sections for conversion of these energies through collisions with light atoms are reduced. Also, as vibrational energies are much larger than rotational energies ($100 \lesssim E_{vib} \lesssim 3500\text{cm}^{-1}$; $E_{rot} \lesssim 10\text{cm}^{-1}$) the cross-section for vibrational relaxation is further reduced. Therefore the temperatures in most seeded supersonic jet expansions are ordered as follows:

$$T_{trans(a)} < T_{trans(m)} < T_{rot(m)} < T_{vib(m)} \tag{2.22}$$

The following are typical values used in the xanthione experiments described in this thesis:

T_0 = 418 K

P_0 = 1000 mbar

m_a = 6.64×10^{-27} kg (Helium)

m_m = 3.52×10^{-25} kg (XT)

D = 0.8 mm

Using these values and inserting them into Equations 2.14 to 2.19, the

[4]For a molecular carrier gas, the rotational temperature of the carrier gas must also be considered. However, the upper vibrational energy levels of the commonly used carrier gases are not usually populated at the temperatures normally used.

UNIVERSITY COLLEGE CORK LIBRARY

following conditions at the excitation zone, $x = 13$ mm downstream from the nozzle are obtained:

$M \simeq 20.8$

$T_{trans(a)} \simeq 2.9$ K

$P \simeq 3.9 \times 10^{-3}$ mbar

$n_a \simeq 9.88 \times 10^{15}$ cm^{-3} (carrier gas density)

$u \simeq 2078$ ms^{-1}

Bibliography

[1] F.J. O'Keeffe. *Triplet States of Jet-Cooled Aromatic Thiones.* PhD thesis, Physics Dept., National University of Ireland, Cork, 1997.

[2] P. Zalicki and R.N. Zare. *J. Chem. Phys.*, 102(7):2708–2717, 1994.

[3] J.N. MacDonald, S.A. Mackay, J.K. Tyler, A.P. Cox, and I.C. Ewart. *J. Chem. Soc., Faraday Trans. 2*, 77:79–99, 1981.

[4] B.S. Pedersen, S. Scheibye, N.H. Nilsson, and S.-O. Lawesson. *Bull. Soc. Chim. Belg.*, 87(3):223–228, 1978.

[5] G. Scoles, editor. *Atomic and Molecular Beam Methods*, volume I. Oxford University Press, 1988. *'Free Jet Sources'* by David R. Miller.

[6] Peter P. Wegener, editor. *Molecular Beams and Low density Gasdynamics.* Marcel Dekker, Inc. New York, 1974. *'Molecular Beams from Nozzle Sources'* by James B. Anderson.

Chapter 3

Phosphorescence Excitation Spectrum of Xanthione

The spectroscopy of the ground and excited states of XT has received considerable attention. This is due to the general interest in thione excited state properties outlined in the introduction and the relatively high symmetry of the molecule, which results in reasonably analysable spectra and the possibility of comparison with its simplest congener pyranethione. The $S_2 \leftarrow S_0$ transition of XT is the most studied, through absorption spectroscopy in solution and in frozen matrices [1], and through laser induced fluorescence (LIF) as a jet-cooled gas sample [2]. The $T_1 \leftarrow S_0$ transition has been studied through excitation spectroscopy with the sample in a Shpolskii matrix at low temperature [1] and in a crystalline host [3]. Both the $S_2 \rightarrow S_0$ fluorescence [4,5] and the $T_1 \rightarrow S_0$ phosphorescence have been reported [5,6] and there has been a report of the infra-red and Raman spectroscopy of the ground state along with theoretical calculations of vibrational frequencies [7]. Somewhat surprisingly, considering this range of studies, there has been no investigation of the $T_1 \leftarrow S_0$ transition for the sample in a molecular jet. This is despite the fact that the above reports span the period when the technique of laser induced phosphorescence

(LIP) spectroscopy of samples in a molecular jet became relatively common. From this summary of available spectroscopic studies on XT, it is clear that a well-resolved spectrum should be readily assigned, as there are a number of analysed spectra for comparison. It is also clear that the S_1 state has not been confidently located, although one of the reports does claim evidence of that state. This is addressed below and the data presented here contradicts that assignment.

A study of the phosphorescence excitation spectrum of the $T_1 \leftarrow S_0$ transition of XT cooled in a supersonic jet is a logical extension of previous work on the corresponding transitions in PT [8] and BPT [9]. XT is expected to exhibit increased vibronic activity compared to the other two molecules owing to its larger number of vibrational modes. As explained below, there is a realistic expectation of achieving an assignment of the observed vibronic structure to an extent comparable with the study of PT owing to the availability of studies of the ground state. The lack of certain knowledge of the location of the S_1 state of XT is similar to the situation that pertained in BPT before this investigation.

3.1 Experimental Details

The experimental apparatus for the phosphorescence excitation spectrum of XT is described in Section 2.1. These general aspects are expanded here.

The carrier gas used was helium and was kept at a stagnation pressure of $\approx$ 1000 mbar. The sample was heated to a temperature of 145° C in a copperblock as described in Section 2.1.3. The excitation region was 13 mm downstream of the nozzle. The nozzle diameter, D, was 0.8 mm. From Equations 2.14–2.20 the following parameters were obtained:

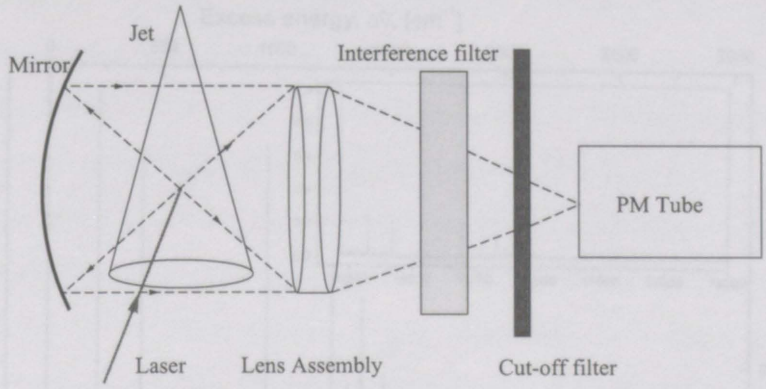


Figure 3.1: Lens and filter arrangement in the phosphorescence excitation spectrum of XT

$$
\begin{aligned}
M &\simeq 20.8 \\
T_{trans(a)} &\simeq 2.9\text{K} \\
u &\simeq 2077\text{ms}^{-1} \\
u^{\infty} &\simeq 2084\text{ms}^{-1}
\end{aligned}
$$

At a velocity of $u \simeq 2077$ ms^{-1} the molecules are at 99.66% of the terminal velocity u^{∞}. It can be assumed that at this distance of 13 mm from the nozzle the molecules are in the free-jet region of the jet expansion (see Figure 2.6) and there are very few collisions occurring here.

Both an interference filter (700FS80-50 Andover Corp.) and a cut-off filter (RG645 Schott GmBH) were used to ensure no scattered laser light was detectable. These were arranged as shown in Figure 3.1. This arrangement ensured that no fluorescence from the cut-off filter due to scattered laser light was detected with a red sensitive photomultiplier tube (Phillips XP2254B).

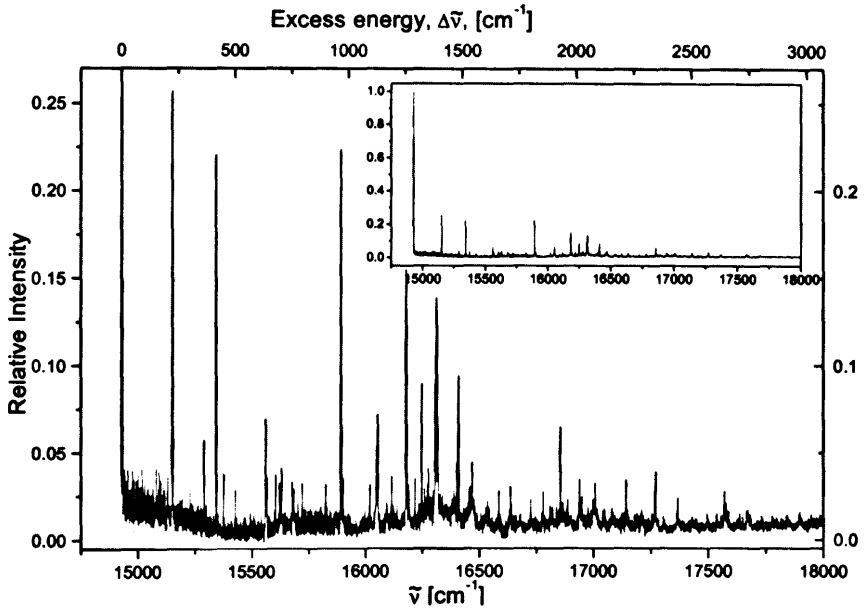


Figure 3.2: The $S_0 \rightarrow T_1$ Phosphorescence Excitation Spectrum of XT in a supersonic jet, carrier gas was helium at a backing pressure of $\approx$ 1 bar. Inset graph illustrates the intensity of the T_{1z} origin compared to the other lines.

3.2 Results and Discussion

3.2.1 The origin of T_{1_z}

The phosphorescence excitation spectrum of XT in the region of $hc \times 14900 - 18000$ cm^{-1} is shown in Figure 3.2. The strongest line by far in this spectrum at 14927.4 cm^{-1} was confidently assigned to the origin of $T_{1,0}$. The corresponding $T_{1,0}$ origins in BPT and PT are 15828 cm^{-1} [8] and 16844 cm^{-1} [9], respectively. This is a well-known feature; the larger the degree of π-conjugation, the lower the electronic excitation energy. The energy of the isolated XT origin is $\approx$ $hc \times 175$ cm^{-1} lower than in a Shpolskii matrix [1] and $\approx$ $hc \times 203$ cm^{-1} lower than in an alkane solvent [10]. This hypsochromic shift is characteristic of $n \rightarrow \pi^*$ transitions. The corresponding hypsochromic shifts for BPT and PT in Shpolskii matrices are $\approx$ $hc \times 262$ cm^{-1} [8] and $\approx$ $hc \times 256$ cm^{-1} [9],

respectively.

As is the case in both PT and BPT, XT exhibits a very large zero-field splitting, $|D^*|/hc = -20$ cm^{-1} in a crystalline host, [3]. This extraordinarily large splitting between the virtually degenerate substates T_{1x}, T_{1y}[1] with the triplet substate T_{1z} is due to the considerable spin-orbit coupling owing to the "heavy" sulphur atom[2]. This large zero-field splitting value is also due to the relatively strong interaction of the T_{1x}, T_{1y} substates with the low-lying second excited triplet substates T_{2y}, T_{2x} respectively and that of the T_{1z} substate with the high-lying second excited singlet state S_2. T_{1x} and T_{2y} have B_1 symmetry, T_{1y} and T_{2x} have B_2 symmetry and T_{1z} and S_2 have A_1 symmetry. This is illustrated in Figure 1.3 on page 6. The energy of T_2 is not known but estimates range from 600 cm^{-1} [6] to 2400 cm^{-1} [3] above T_1. In the condensed phase the $T_1 \leftarrow S_0$ absorption initially populates the T_{1z} sublevel almost exclusively and subsequent spin-lattice relaxation is required to populate T_{1x} and T_{1y}. However, in isolated XT, as is the case here in a supersonic jet expansion at 13 mm downstream from the nozzle, there is no mechanism for spin-lattice relaxation. For T_{1x} and T_{1y} to gain intensity they require a higher order of spin–orbit coupling than the $T_{1z,0} \leftarrow S_{0,0}$ transition. Intensity may be gained by mixing with S_2, $^1A_1(\pi\pi^*)$, the state closest in energy to which absorption is allowed. It is for these reasons that the origin is confidently labelled T_{1z}. Due to the lack of a mechanism for spin-lattice relaxation one would not expect to observe the zero-field splitting for isolated XT.

3.2.2 Vibrational Analysis

XT has C_{2v} symmetry giving a total of 63 normal vibrational modes composed of 22 a_1 and 21 b_2 in-plane and 9 a_2 and 11 b_1 out-of-plane motions. Transitions

[1] $\Delta E_{T_{1x},T_{1y}} = 0.0611$ cm^{-1} [6].

[2] The spin-orbit coupling constant scales to the fourth power of the atomic number, i.e. Z^4. Therefore, the larger Z the larger the spin-orbit coupling.

to vibronic levels of T_{1z} of a_2 symmetry are forbidden and 8 of the in-plane vibrations are due to C–H stretches with energies in excess of 3000 cm^{-1} and hence lie outside the range of the spectrum shown in Figure 3.2. Therefore a maximum of 46 fundamental modes would be expected to be observed.

A previous study of XT in a Shpolskii matrix [1], a complete vibrational analysis of XT in the ground state [7] and an ab initio calculation of the ground state vibrations of XT using the Gaussian 98 software [11] were used in the analysis of the spectrum presented here. The analysis of the Shpolskii matrix spectrum was given with the presumption of two origins, one 950 cm^{-1} higher in energy than the first. The assignment of this second line as an origin arose from a very similar pattern of vibronic structure being built on it as that for the low energy origin. The equivalent line is observed in the jet spectrum at 15892 cm^{-1}, 964 cm^{-1} higher in energy than the origin and again has a similar pattern of vibronic lines associated with it. Initially the analysis reported here makes no assumption as to the assignment of the 964 cm^{-1} line, treating it as simply a vibronic line of the transition. After assigning the spectrum on that basis the reasons for discounting the alternative assignment are presented. The assignment of vibronic lines is based on the usual criteria of:

(i) commonly repeated intervals;

(ii) the greater probability of observing vibronic lines involving modes of a_1 symmetry;

(iii) that strongly active modes will involve the C=S chromophore;

(iv) the expectation that modes will have frequencies not too different from those observed in other states.

The second point, whilst commonly observed, can be explained more accurately. Vibronic transitions, $T_{1z,v'} \leftarrow S_{0,v''=0}$, have intensities proportional to

the integral:

$$\langle S_{0,v''=0}|\mu|T_{1z,v'}\rangle$$

where μ has x (b_1), y (b_2), z (a_1) components, the symmetries referring to C_{2v}. As both the electronic states have A_1 symmetry as does the v''=0 level, this requires $\Gamma_\mu = \Gamma_{v'}$ for non-zero intensity and hence v' levels of a_2 symmetry are forbidden. There is a distinct difference, however, between μ_z, v' (a_1) transitions and either of the other two symmetry allowed possibilities. The integral can be separated into electronic and nuclear components as:

$$\langle S_0|\mu_z|T_{1z}\rangle\langle v'' = 0|v', a_1\rangle$$

for v' states of a_1 symmetry, making the intensity of these vibronic lines proportional to the intensity of the origin – the strongest line in the spectrum – through a ratio of, non-zero, Frank-Condon factors. For v' of b_1 or b_2 symmetry no such separation is possible and the intensity integral:

$$\langle S_{0,v''=0}|\mu_{x,y}|T_{1z,v',b_1,b_2}\rangle$$

implies coupling of nuclear vibrational and electronic motion for the transition to gain intensity. Stated differently, but equivalently, the transitions to v', a_1 levels are allowed through first-order (1°) spin-orbit coupling interaction to overcome the spin selection rule, whilst the transitions to v', b_1, b_2 levels depend on second-order (2°) spin-orbit coupling and/or the nuclear co-ordinate dependence of μ for non-zero intensity. Whilst not guaranteed, it is usual that such 2° mechanisms result in considerably reduced intensity.

A total of 46 lines are listed in Table 3.1 along with their assignments as fundamental modes or combinations of modes. These lines in the spectrum are accounted for by 20 vibrational modes, 11 of a_1, 5 of b_1 and 4 of b_2 symmetry.

Four of the five strongest vibronic lines involve single quanta of individual a_1 symmetry modes, ν_3, ν_7, ν_{12} and ν_{14}, the fifth being ν_{43} of b_2 symmetry, and it has to be expected that these will be modes involving motion in the region of the C=S group. As can be seen from Table 3.3 four of these five modes, ν_3, ν_7, ν_{12} and ν_{43}, form the bases for vibronic progressions. These combinations agree to within 2 cm^{-1} with the sum of the fundamental frequencies in most cases and any assignments outside this range are to be considered tentative. Table 3.2 lists the energies of the modes identified and compares these with the values assigned to the same modes in S_0, T_1 and S_2 states in the studies previously mentioned. Most modes have T_1 frequencies between $0.94 - 1.03$ of their S_0 values (with the exception of ν_{43} at 0.92 largely as a result of the low frequency of the mode magnifying the proportional change). The ν_7 mode is of particular interest having the largest vibronic progression based on it, 9 modes in total. It is worth pointing out that this mode has decreased in energy by $\approx$ 58 cm^{-1} compared to the ground state but this is in keeping with the above range. The other possible assignment as ν_8, ground state frequency of 1041 cm^{-1}, would be outside the range. A value of the frequency of ν_7 in S_2 of 957 cm^{-1} is given in Table 3.2 but is not the value reported in any of the LIF studies of XT. In all such studies there is a band 957 cm^{-1} above the origin and this is consistently assigned as being a combination band involving two modes with frequencies of 623 and 335 cm^{-1}. This assignment ignores the fact that the 957 cm^{-1} line is the strongest line in the spectrum (after the origin) and is considerably stronger than the lines involving single quanta of the combining modes. Despite the coincidence of the energies, the intensities contradict the assignment and therefore this line has been re-assigned as a single quantum of the a_1 symmetry mode, ν_7.

There is no recognised C=S vibration at $\approx$ 965 cm^{-1} and this may the reason why this line is assigned as the S_1 origin. However, in the complete

vibrational analysis of the ground state of XT by Sinha et al. [7] a value for ν_7 at 964.2 cm^{-1} is calculated. This calculation, which was a Gaussian 98 calculation of the ground state vibrations at the Hartree-Fock level using the CEP-31G basis, was reproduced. The calculated frequency of the ν_7 vibration was 964.80 cm-1 (after multiplying by the optimal Pople correction factor of 0.8953 [12]). Whilst there is nothing new in this, the output section describing the extent of atomic motions, information not detailed by Sinha et al. [7], was analysed to identify which modes are active in the C=S region. The modes were also visualised using the Hyperchem software package[3]. The extent of the relative motion of the carbon and sulphur atoms of the CS group decreases for each symmetry species as listed below.

a_1 (z) modes, $\nu_1 - \nu_{22}$:

$$\nu_7,\ \nu_{12},\ \nu_3 \ >\ \nu_4,\ \nu_{14},\ \nu_5,\ \nu_2 \ >\ \nu_6,\ \nu_{10},\ \nu_9,\ \nu_{17},\ \nu_{11},\ \nu_{13},\ \nu_{16}$$
$$>\ \nu_8,\ \nu_{15},\ \nu_1,\ \nu_{18} - \nu_{22}$$

b_1 (x) modes, $\nu_{32} - \nu_{42}$:

$$\nu_{37},\ \nu_{33},\ >\ \nu_{35},\ \nu_{34}\ >\ \nu_{38},\ \nu_{32},\ \nu_{36},\ \nu_{39}\ >\ \nu_{40} - \nu_{42}$$

b_2 (y) modes, $\nu_{43} - \nu_{63}$:

$$\nu_{43}\ >\ \nu_{47},\ \nu_{45},\ \nu_{48}\ >\ \nu_{54},\ \nu_{46},\ \nu_{53},\ \nu_{52},\ \nu_{55}$$
$$>\ \nu_{57},\ \nu_{49},\ \nu_{56},\ \nu_{50},\ \nu_{59},\ \nu_{58},\ \nu_{44},\ \nu_{60} - \nu_{63}$$

where the direction of relative motion is given (x,y,z) and > represents a decrease in the C=S activity. An approximate order of magnitude implied, in arbitrary units, is

$$40\ >\ 10\ >\ 5\ >\ 1$$

[3]An evaluation version of this software was obtained from the Internet (`http://www.hyper.com`) and the visualisation routine was used to investigate the atomic motions in each of the calculated vibrations.

As can be seen those modes not involving C=S motion, for example the C–H stretches of ν_{19}–ν_{22} and ν_{60}–ν_{63}, are all on the lower end of the activity scale. The a_2 modes are not shown as such modes of vibration do not involve motion of atoms on the C_2 axis, thus excluding C=S activity.

The $S_1 \leftarrow S_0$ transition may gain intensity by first–order vibronic coupling of $S_1(^1A_2)$ with the $S_2(^1A_1)$ state through the a_2 symmetry modes of S_1. However, the a_2 modes do not even exhibit motion of the atoms adjacent to the C=S group and is a major cause of the low intensity of the $S_1 \leftarrow S_0$ transition. Seven of the nine calculated a_2 symmetry modes show effectively zero motion on the central ring of the molecule, and in the remaining two modes motion on this ring is not large. This is presumably due to the extended conjugated bonding structure restricting non-planar motion of the central ring and therefore the a_2 symmetry modes involve mainly motion of the "wings" of the molecule. Although Sinha et al. [7] state that both the ν_3 and the ν_{12} modes of XT in the ground state are strongly C=S localised vibrational modes of a_1 symmetry, most a_1 symmetry vibrations show some degree of C=S stretching, the exceptions being the 4 a_1 C—H stretches, with ν_7 having the largest relative motion of atoms. The activity of the C=S group has also aided in the assignment of one mode over another. The energies of ν_1 and ν_{43} calculated above are very similar, $hc \times 226$ and $hc \times 243$ cm^{-1}. The low-energy vibronic transition at $hc \times 15150$ cm^{-1} ($\Delta E = hc \times 222.6$ cm^{-1}) could be assigned to either of the two modes on energy and symmetry grounds. However, it is expected that those modes showing activity in the C=S region are likely to be more intense than those with low activity. In fact, ν_{43} was found to be very active, while ν_1 was found to be completely inactive in the C=S region, allowing a confident assignment of ν_{43} to the transition occurring at $hc \times 15150$ cm^{-1}.

Table 3.1: Assignment and comparison of vibrational modes of XT assuming two origins.

Energy cm^{-1}	Assign.	$\Delta\tilde{\nu}$ cm^{-1}	Rel. Int.	ΔE cm^{-1}	Assign.	$\Delta\tilde{\nu}$ cm^{-1}	Rel. Int.	ΔE cm^{-1}
14927.40	T_{1z} origin	0	1.00					
15079.00	ν_{33}	151.6	0.04					
15150.20	ν_{43}	222.8	0.26					
15288.60	ν_2	361.2	0.06					
15342.20	ν_3	414.8	0.22					
15374.20	$2\nu_{43}$ or ν_{44}	446.8	0.04	1.2				
15426.20	ν_{36}	498.8	0.03					
15560.60	ν_4	633.2	0.07					
15565.00	$\nu_3 + \nu_{43}$	637.6	0.04	0.0				
15603.00	ν_5	675.6	0.04					
15621.00	ν_a	693.6	0.03					
15630.60	ν_b	703.2	0.04					
15675.40	ν_{38}	748.0	0.03					
15719.80	ν_{39}	792.4	0.03					
15720.60	ν_6	793.2	0.03					
15825.80	ν_{48}	898.4	0.03					
15892.20	ν_7	964.8	0.22		S_1 or ν_7 origin	0.0	0.22	
15900.60	ν_{42}	973.2	0.04					
15922.20	$\nu_2 + \nu_4$	994.8	0.02	0.4				
16017.80	$\nu_3 + \nu_5$	1090.4	0.03	0.0				
16045.80		1184.4			ν_{33}	153.6	0.04	2.0
16053.40	ν_9	1126.0	0.07					
16114.60					ν_{43}	222.4	0.04	0.4

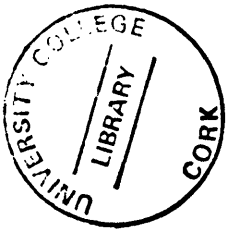
Table 3.1: continued overleaf

Table 3.1: Assignment and comparison of vibrational modes of XT assuming two origins (continued).

Energy cm^{-1}	Assign.	$\Delta\tilde{\nu}$ cm^{-1}	Rel. Int.	ΔE cm^{-1}	Assign.	$\Delta\tilde{\nu}$ cm^{-1}	Rel. Int.	ΔE cm^{-1}
16179.00	ν_{12}	1251.6	0.15					
16216.60	ν_{13}	1289.2	0.04					
16247.00	ν_{54}	1319.6	0.09					
16306.60					ν_3	414.4	0.09	0.4
16312.20	ν_{14}	1384.8	0.14					
16401.40	$\nu_{12}+\nu_{43}$	1474.0	0.04	0.4				
16408.60	ν_{16}	1481.4	0.09					
16459.80	ν_{58}	1532.6	0.03					
16468.20	$\nu_3+\nu_9$	1540.8	0.05	0.0				
16468.20	$\nu_{38}+\nu_{39}$	1540.4	0.05	0.4				
16585.80					ν_a	693.6	0.03	0.0
16635.80	$2(\nu_{33}+\nu_b)$	1708.4	0.03	1.2				
16641.00					ν_{38}	748.8	0.02	0.8
16855.40	$2\nu_7$	1928.0	0.07	1.6	ν_7	963.2	0.07	1.6
16865.40					ν_{42}	973.2	0.02	0.0
16886.60					$\nu_2+\nu_4$	994.4	0.02	0.0
16982.60					$\nu_3+\nu_5$	1090.4	0.01	0.0
17005.80	$\nu_a+\nu_{14}$	2078.4	0.03	0.0				
17017.40					ν_9	1125.2	0.02	0.8
17142.80					ν_{12}	1250.6	0.04	1.0
17210.40					ν_{54}	1318.2	0.02	1.4
17271.20					$\nu_3+\nu_7$	1379.0	0.04	0.6
17365.60					$\nu_7+\nu_{12}+\nu_{43}$	1473.4	0.03	1.0

	This Thesis T_{1z} $\Delta\tilde{\nu}/cm^{-1}$	Table III Ref [7] S_0 $\Delta\tilde{\nu}/cm^{-1}$	Table II Ref [1] S_0 $\Delta\tilde{\nu}/cm^{-1}$	Ratio T_1/S_0 †	Table I Ref [1] T_1 $\Delta\tilde{\nu}/cm^{-1}$	Table 1 Ref [5] S_2 $\Delta\tilde{\nu}/cm^{-1}$
a_1 modes						
ν_2	361.2	379.7	378	0.951		335
ν_3	414.8	439.2	435	0.944	411	
ν_4	633.2	642.7	641	0.985	649	623
ν_5	675.6	684.2		0.987		671/676
ν_6	793.2	807.5		0.982		
ν_7	964.8	1022.7	1031	0.943	950	957
ν_9	1126.0	1155.0	1156	0.975	1121	
ν_{12}	1251.6	1240.7	1243	1.009	1237	
ν_{13}	1289.2	1286.5	1285	1.002		1292
ν_{14}	1384.8	1341.3	1341	1.032	1382	
ν_{16}	1481.2	1479.6	1484	1.001	1475	
b_1 modes						
ν_{33}	151.6	150.0	126	1.011		
ν_{36}	498.8	528.0		0.945		
ν_{38}	748.0	749.1		0.999		747
ν_{39}	792.4	822.3		0.964		
ν_{42}	973.2	979.6		0.993		
b_2 modes						
ν_{43}	222.8	241.5	239	0.923	222	
ν_{48}	898.4	913.7		0.983		
ν_{54}	1319.6	1323.9		0.997		
ν_{58}	1532.6	1561.5		0.981		

Table 3.2: Frequencies of vibrational modes of T_1, comparison with other techniques and states. †S_0 values are taken from Ref [7].



no. fund.	$T_{1z,v}$ cm^{-1}	ν_{43} cm^{-1}	ν_3 cm^{-1}	ν_7 cm^{-1}	ΔE cm^{-1}	ν_{12} cm^{-1}
origin	14927.4	15150.2	15342.2	15892.2		16179.0
ν_{33}	151.6			153.6	2.0	
ν_{43}	222.8	224.0	222.8	222.4	0.4	222.4
ν_2	361.2					
ν_3	414.8	414.8		414.4	0.4	
ν_{36}	498.8					
ν_4	633.2					
ν_5	675.6		675.6			
ν_{38}	748.0			748.8	0.8	
ν_{39}	792.4					
ν_6	793.2					
ν_7, $S_{1,0}$	964.8	964.4	964.4	963.2	1.6	963.8
ν_{42}	973.2			973.2	0.0	
$\nu_2 + \nu_4$	994.8			994.4	0.4	
$\nu_3 + \nu_5$	1090.4			1090.4	0.0	
ν_9	1126.0		1126.0	1125.2	0.8	
ν_{12}	1251.6	1251.2		1250.6	1.0	
ν_{13}	1289.2					
ν_{54}	1319.6			1318.2	1.4	
ν_{14}	1384.8					
$\nu_{12} + \nu_{43}$	1474.0			1473.4	0.6	
ν_{57}	1481.4					
ν_{58}	1532.6					

Table 3.3: Comparison of the most prominent progressions of XT based on vibronic origins ν_{43}, ν_3, ν_7 and ν_{12}.

Comparison of structure built on the origin and the 15892 cm^{-1} line

The $T_{1z,0}$ origin and the line at 15892 cm^{-1}($hc \times 965$ cm^{-1} higher in energy than the origin) support very similar patterns of vibronic structure. The extent to which these patterns are similar is important in the discussion in the following section and therefore is considered in more detail here. Figure 3.3 shows the two groups of transitions being compared. The intensities of the two groups of lines are compared in form of a histogram in Figure 3.4. The intensities of the transitions associated with the $hc \times 15892$ cm^{-1} line have been increased by a factor of 5.5 to set the intensities of the two 'origins' equal at unity. The similarity of the two patterns in terms of energy separations and intensities is

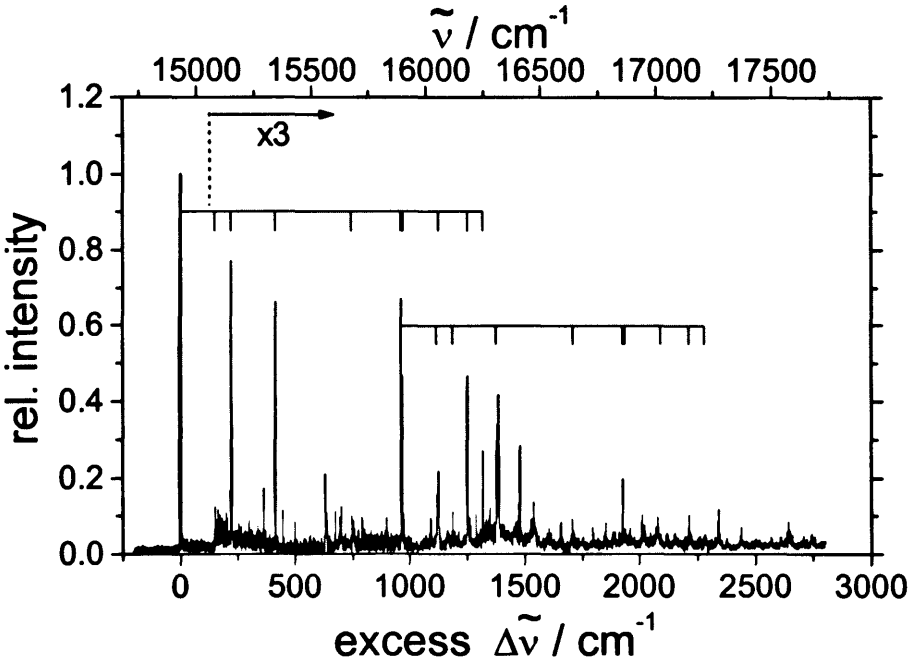


Figure 3.3: Comparison of vibronic transitions based on $T_{1z,0}$ and line at 15892 cm^{-1}. The y-scale has been multiplied by a factor of 3 from 15070 cm^{-1} on. The combs show the transitions being compared.

remarkable.

From Table 3.1 and Figure 3.4 it is clear that the 15892 cm^{-1} line supports vibronic transitions involving considerably fewer fundamental modes than does the origin. This is not simply due to the relative intensities of the two 'origins' and subsequent lines based on 15892 cm^{-1} not having enough intensity to be observed. From the work on the activities of the modes, a distinction is drawn between the vibronic 'origins'. Nine modes are common to both 'origins'. Five of these modes (ν_3, ν_7, ν_{12}, ν_{33}, and ν_{43}) are very strongly localised on the C=S group. Three modes (ν_9, ν_{38} and ν_{54}) have significant C=S activity and only one (mode ν_{42}) is from the C=S inactive group. These nine modes are not exclusively a_1 symmetry modes which one would assume to be the most intense, they are: 4 a_1 modes (ν_3, ν_7, ν_9, ν_{12}), 3 b_1 modes (ν_{33}, ν_{38}, ν_{42}) and 2

b_2 modes (ν_{43}, ν_{54}). Nor is it based simply on the most intense vibrations in T_{1z}, as in some cases the intensity of the vibronic line based on 15892 cm^{-1} is significantly greater (relatively) than that based on T_{1z}. Of the twelve more modes associated only with the origin $T_{1z,0}$, none are from the most active group, five (ν_2, ν_4, ν_5, ν_{14}, ν_{48}) and six (ν_6, ν_{16}, ν_{36}, ν_{38},ν_{39}, and ν_{48}) are from the progressively less C=S active groups and one ν_{58} from the inactive group. This is clear evidence that there is a strong bias towards strongly C=S active modes being associated with the 15892 cm^{-1} line.

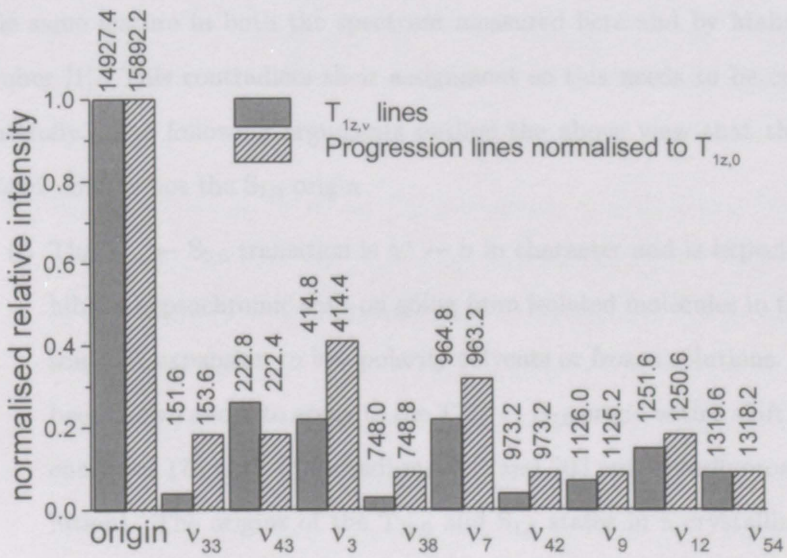


Figure 3.4: Comparison of vibration intensities. Values in the first row are the excess enegries of vibrations based on the T_{1z} origin at 14927.4 cm^{-1}. Similarly values in the second row are the excess energies of vibrations based on a ν_7 vibronic origin at 15892.2 cm^{-1}.

3.2.3 Observability of $S_1 \leftarrow S_0$

Mahaney and Huber [1] assign the $S_{1,0}$ origin in a Shpolskii matrix to the strong vibration at $\approx$ 950 cm^{-1} above T_1. The authors do point out, however, that

this assignment is tentative. This assignment was a quite reasonable conclusion to arrive at since the pattern of vibronic structure is very similar to that based on the $T_1 \leftarrow S_0$ transition. Also, in the matrix environment used, intersystem crossing $S_1 \rightsquigarrow T_1$ is more probable. Thus an excitation and emission scheme of $S_{0,0} \rightarrow S_{1,0} \rightsquigarrow T_{1z,\nu'} \rightarrow S_{0,\nu''}$ is likely. The strong vibration (fourth strongest line) at 965 cm^{-1} above T_{1z} (15892 cm^{-1}) in Figure 3.2 corresponds to the $S_{1,0} \leftarrow S_{0,0}$ assignment in [1]. In the previous sections it was assumed that this line is a vibronic transition in $T_{1z} \leftarrow S_0$ excitation spectrum and not the S_1 origin. In this thesis, it is assumed that the line at 965 cm^{-1} above T_{1z} is the same feature in both the spectrum measured here and by Mahaney and Huber [1]. This contradicts their assignment so this needs to be considered carefully. The following arguments outline the above view that the line at 15892 cm^{-1} is not the $S_{1,0}$ origin.

(i) The $S_{1,0} \leftarrow S_{0,0}$ transition is $\pi^* \leftarrow n$ in character and is expected to exhibit a hypsochromic shift on going from isolated molecules in the supersonic jet expansion to low polarity solvents or frozen solutions. This has been shown above to apply to the $T_{1z,0} \leftarrow S_{0,0}$ origin with a shift to higher energy of 175 cm^{-1} (Shpolskii matrix) and 203 cm^{-1} (perfluoroalkane solution). The origins of the $T_{1z,0}$ and $S_{1,0}$ states in a crystalline matrix have been observed to be at 15383 and 16039 cm^{-1}, respectively [13], an environment comparable to the Shpolskii matrix. If the 15892 cm^{-1} line were the $S_{1,0} \leftarrow S_{0,0}$ transition, this would imply a large difference of 309 cm^{-1} between the shifts experienced by the T_1 state and S_1 states of XT on changing environment from the isolated molecule in a jet to the crystalline matrix with the T_1 state shifted by 456 cm^{-1} and the S_1 state by 147 cm^{-1}. This has to be considered unlikely. BPT has a separation between $T_{1z,0}$ and $S_{1,0}$ states of 694 cm^{-1} in the gas phase and 690 cm^{-1} in solution, showing that the two states experience almost the same hyp-

sochromic shift for this similar molecule. In order for the T_1 and S_1 states of XT to exhibit such significantly different interactions with the environment they would have to have significantly different electron distributions. This inevitably implies a significant difference in the chemical bonding found in the $T_{1,z}$ and S_1 states and therefore differences in their vibrational frequencies and wavefunctions. This is incompatible with the remarkable similarity — in both energies and intensities — of the two vibronic patterns observed on the origin and the 15892 cm^{-1} band, discussed above. The similarity is so close that of the two possible explanations that of only one state being involved had to be preferred, but the possibility of two states being involved becomes increasingly unlikely if those states have also to exhibit different electronic distributions.

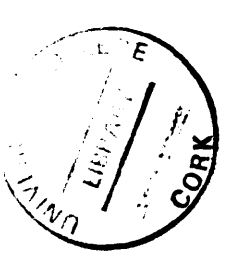
(ii) The transition at 15892 cm^{-1} is too intense to involve the same photophysics that allowed the $S_{1,0} \leftarrow S_{0,0}$ transition in BPT to be observed in the phosphorescence excitation spectrum through the process $S_{0,0} \rightarrow S_{1,0} \rightarrow S_{n,\nu} \rightsquigarrow T_{1z,\nu'} \rightarrow S_{0,\nu''}$ [14]. The observed feature in the BPT phosphorescence excitation spectrum is very weak which is to be expected of a multiphoton mechanism. A similarly weak transition in the PT spectrum has been tentatively assigned to the S_1 origin observed through the same mechanism [8]. In both these molecules the density of $T_{1z,\nu'}$ levels at the energy of $S_{1,0}$ is too low to result in the mechanism, $S_{0,0} \rightarrow S_{1,0} \rightsquigarrow T_{1z,\nu'} \rightarrow S_{0,\nu''}$, being viable. If the transition in XT is the S_1 origin, then its intensity indicates that it must arise through the direct mechanism which requires a close energy match of $S_{1,0}$ and $T_{1z,\nu'}$ levels.

One way of considering if this match is probable is by comparing the density of $T_{1z,\nu'}$ levels of XT and BPT using Haarhoff's purely statis-

tical method of estimating densities of vibronic states [15]. Using the 63 fundamental frequencies determined for the ground state of XT, the density of $T_{1z,\nu'}$ states is found to be ~ 0.42 cm^{-1} at an excess energy of $hc \times 965$ cm^{-1}. The equivalent density for BPT at the excess energy corresponding to its $S_{1,0}$ level is ~ 0.06 cm^{-1}. Whilst the difference of a factor of 7 is large, it is not large enough to be confident that XT lies outside the coupling regime for small molecules or that efficient $S_{1,\nu} \rightsquigarrow T_{1z,\nu'}$ interaction is to be expected.

Therefore, the S_1 origin is observable through the direct mechanism only if there is a fortuitous coincidence in energy of $S_{1,0}$ and a $T_{1z,\nu'}$ level. The presence of a heavy atom in the molecule ensures strong spin-orbit interaction provided the interacting levels are close in energy. Therefore the assignment as $S_{1,0}$, also requires a coincidence in energy between all the $S_{1,\nu}$ levels observed and $T_{1z,\nu'}$ levels. The density of $T_{1z,\nu'}$ states of XT across the range of excess energies from 965 to 2000 cm^{-1} — the spectral range of the vibronic transitions built on the line at 15892 cm^{-1} — varies from ~ 0.42 to ~ 1330 (cm^{-1})$^{-1}$. Even at the high energy limit of the range the density is far from the statistical limit of vibronic coupling.

(iii) Figure 3.3 shows that the patterns of vibronic transitions observed based on the two 'origins' are very similar. However there are many bands based on the T_{1z} origin that do not appear in the progression based on the line at 15892 cm^{-1}. The assignment of this line as the S_1 origin could explain this difference if the 'missing' bands were mostly the low frequency ones. They would then occur at energies where the density of $T_{1z\nu'}$ levels is too small for coincidences in energy to be probable. However, three of the four lowest frequency modes are observed, ν_{33}, ν_{43} and ν_3, and the



'missing' modes are largely in the middle range of frequencies. This is contrary to a statistical explanation based on the density of $T_{1z\nu'}$ levels outlined in (ii). The selection of modes observed is more likely to be due to the differences in the extent of C=S activity discussed above. Of the 'missing' modes, ν_2, ν_6, ν_{13}, ν_{33}, ν_{39}, ν_{43} and ν_{44}, all have little or no motion in the C=S region, leaving only ν_4 and ν_5 as modes that may have been expected to be observable but they do not occur in the progression based on the line at 15892 cm^{-1}.

It is our opinion, based on these arguments, that the transition at 15892 cm^{-1}, $hc \times 965$ cm^{-1} higher in energy than the T_{1z} origin, is more likely to be a vibronic transition $T_{1z,\nu} \leftarrow S_{0,0}$ than the origin of the $S_{1,0} \leftarrow S_{0,0}$ transition.

Justifying the assertion that the 15892 cm^{-1} is not the S_1 origin would be best achieved by a definitive identification of the $S_{1,0}$ level, e.g. through a high resolution absorption experiment. Such data is not currently available but in fact if the assignment of the line as a vibronic transition is accepted then the phosphorescence excitation spectrum does show tentative evidence of the $S_1 \leftarrow S_0$ transition. In Table 3.2 four lines in the spectrum are left unassigned and indicated by ν_a, ν_b, $\nu_a+\nu_7$ and $\nu_a+\nu_{14}$. The energies of ν_a and ν_b were incompatible with any ground state modes assigned in Ref. [7] or with any acceptable combinations of modes. It is possible that the ν_a line is in fact the $S_{1,0} \leftarrow S_{0,0}$ transition and is being observed through the multiphoton mechanism that is known to operate in BPT. This assignment would place $S_{1,0}$ at approximately 700 cm^{-1} above $T_{1z,0}$ similar to the 656 cm^{-1} observed in the crystalline matrix [3]. The lines labelled ν_a and ν_b are very weak, as is to be expected from a multiphoton mechanism. The other two transitions are then transitions

involving S_1 vibronic levels observed through the same mechanism. The frequencies of two modes of S_1 happen to be very close to the ν_7, and ν_{14} modes of T_{1z} resulting in the assignment labelling used in Table 3.2. They may even correspond to those modes in S_1, which is quite possible, as modes in the two electronic states should have similar frequencies. ν_b, at a separation of 10 cm^{-1} from ν_a, cannot be a vibrational mode based on that origin but could be a hot, sequence transition involving a low frequency mode active in both ground and excited singlet states. The lowest frequency modes are out-of-plane vibrations and should couple effectively to the electronic S_1 state with its overall out-of-plane symmetry of A_2 and could have an energy difference of +10 cm^{-1} between S_0 and S_1. It is worth noting that if the previous assignment of the 15892 cm^{-1} line applied there would be no sensible explanation for ν_a and ν_b.

3.3 Conclusions

The direct $T_1 \leftarrow S_0$ transition of isolated XT in a molecular jet has been measured up to an excess energy of $\approx$ 3000 cm^{-1}. The T_{1z} origin has been observed at 14927.4 cm^{-1}, corresponding to a hypsochromic shift of $\approx$ hc $\times$ 175 cm^{-1} and $\approx$ hc $\times$ 203 cm^{-1} compared to a Shpolskii matrix and an alkane solvent, respectively. 19 fundamental modes have been assigned and a vibronic origin based on ν_7 has been assigned.

A serious doubt has been raised over the assignment of S_1 by Mahaney and Huber, and it is this value of S_1 that has been cited since. The progression observed in a Shpolskii matrix and assigned as a progression in S_1 is now in considerable doubt. However, until the exact position of S_1 is confirmed, the assignment of ν_7 is tentative. In order to confirm the energy of the S_1 origin a multiphoton absorption experiment would have to be attempted.

UNIVERSITY COLLEGE LIBRARY CORK

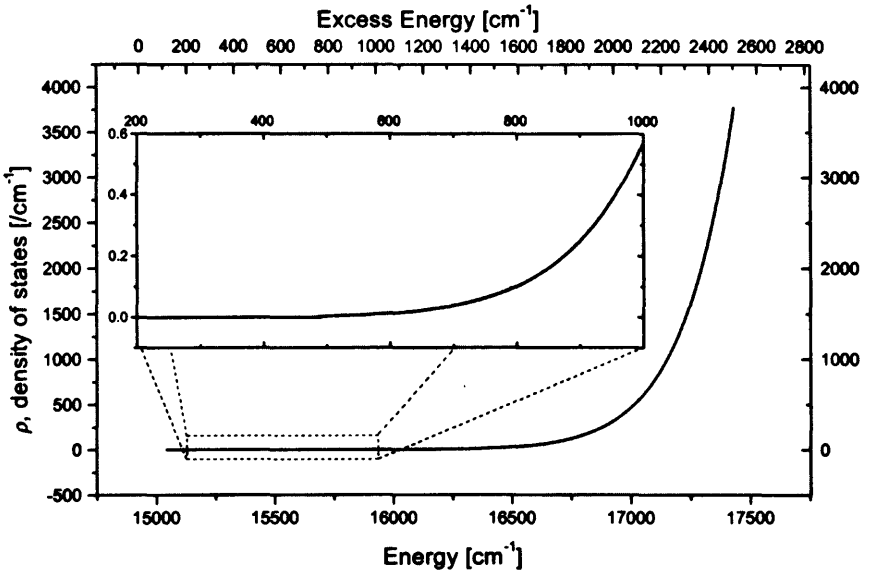


Figure 3.5: Density of states, ρ, per cm^{-1} calculated by Haarhoff's semi-classical method [15] using the values of the 63 fundamentals for the ground state given in Reference [7]. The inset graph shows the region 200—1000cm^{-1} magnified.

Bibliography

[1] M. Mahaney and J.R. Huber. *J. Mol. Spectrosc.*, 87:438–448, 1981.

[2] H.K. Sinha and R.P. Steer. *J. Mol. Spectrosc.*, 181:194–206, 1997.

[3] D.M. Burland. *J. Chem. Phys.*, 75(6):403–411, 15 September 1981.

[4] S.A. Wittmeyer, A.J. Kaziska, M.I. Shchuka, A.L. Motyka, and M.R. Topp. *Chem. Phys. Lett.*, 151(4,5):384–390, 1988.

[5] A.L. Motyka and M.R. Topp. *Chem. Phys.*, 121:405–417, 1988.

[6] M.R. Taherian and A.H. Maki. *Chem. Phys.*, 68:179–189, 1982.

[7] H.K. Sinha, L. Chantranupong, and R.P. Steer. *J. Mol. Spectrosc.*, 169:302–314, 1995.

[8] A.A. Ruth, F.J. O'Keeffe, M.W.D. Mansfield, and R.P. Brint. *J. Phys. Chem. A*, 101(42):7735–7741, 1997.

[9] A.A. Ruth, F.J. O'Keeffe, R.P. Brint, and M.W.D. Mansfield. *Chem. Phys.*, 217:83–98, 1997.

[10] A. Maciejewski and R.P. Steer. *Chem. Rev.*, 93:67–98, 1993. and references therein.

[11] M. J. Frisch, G. W. Trucks, H. B. Schlegel, G. E. Scuseria, M. A. Robb, J. R. Cheeseman, V. G. Zakrzewski, Jr. J. A. Montgomery, R. E.

UNIVERSITY COLLEGE Library CORK

Stratmann, J. C. Burant, S. Dapprich, J. M. Millam, A. D. Daniels, K. N. Kudin, M. C. Strain, O. Farkas, J. Tomasi, V. Barone, M. Cossi, R. Cammi, B. Mennucci, C. Pomelli, C. Adamo, S. Clifford, J. Ochterski, G. A. Petersson, P. Y. Ayala, Q. Cui, K. Morokuma, D. K. Malick, A. D. Rabuck, K. Raghavachari, J. B. Foresman, J. Cioslowski, J. V. Ortiz, A. G. Baboul, B. B. Stefanov, G. Liu, A. Liashenko, P. Piskorz, I. Komaromi, R. Gomperts, R. L. Martin, D. J. Fox, T. Keith, M. A. Al-Laham, C. Y. Peng, A. Nanayakkara, C. Gonzalez, M. Challacombe, P. M. W. Gill, B. Johnson, W. Chen, M. W. Wong, J. L. Andres, C. Gonzalez, M. Head-Gordon, E. S. Replogle, and J. A. Pople. *Gaussian 98, Revision A.7.* Gaussian Inc., Pittsburgh PA, 1998.

[12] J.A. Pople, A.P. Scott, M.W. Wong, and L. Radom. *Isr. J. Chem..*, 33:345–350, 1993.

[13] H. Eisenberger and B. Nickel. *J. Chem. Soc. Faraday Trans.*, 92:733, 1996.

[14] A.A. Ruth, F.J. O'Keeffe, M.W.D. Mansfield, and R.P. Brint. *Chem. Phys. Lett.*, 264:605–613, 1997.

[15] P.C. Haarhoff. *Mol. Phys.*, 7:101–117, 1963.

Chapter 4

Phosphorescence Excitation Spectrum of 4*H*–pyrane–4–thione

4.1 Introduction

As stated in Chapter 2, the large energy separation between the first excited singlet state $^1(n\pi^*)$ and the higher energy excited $^1(\pi\pi^*)$ state of aromatic thiones causes the rate of non–radiative decay from the higher to the lower state to be small (cf. Energy Gap Law, Section 1.2). This leads to prompt fluorescence from the $^1(\pi\pi^*)$ state being observable with significant quantum yield. For the compounds xanthione (XT) and 4H–1–benzopyran–4–thione (BPT) the energy of $^1(\pi\pi^*)$ (denoted S_2) is accurately known from measurements of the prompt $S_2 \rightarrow S_0$ fluorescence upon excitation in the $S_2 \leftarrow S_0$ absorption band in cold supersonic expansions [1,2]. The vibronic structure of S_2 and its intramolecular relaxation dynamics showed that the vibronic coupling of S_2 with S_1 in XT and in BPT is well within the statistical limit, which is expected for the observed large energy gaps of $\Delta(S_1,S_2) \approx 8000\text{cm}^{-1}$ [1,3] and

$\Delta(S_1,S_2) = 9330cm^{-1}$ [4,5], respectively. For the smaller 4H–pyran–4–thione (PT), however, no excitation spectrum of the prompt fluorescence from $^1(\pi\pi^*)$ has been measured under jet–cooled conditions due to its much smaller fluorescence quantum yield in comparison to XT and BPT [3]. Hence for PT no detailed information on the vibronic structure of the excited $^1(\pi\pi^*)$ state exists. Since PT exhibits a high intersystem–crossing (ISC) quantum yield upon excitation in the singlet manifold (phosphorescence quantum yield $\Phi_p = 0.33$ in perfluoroalkane [6]), the $^1(\pi\pi^*)$ state of PT was investigated by measuring the excitation spectrum of the $^3(n\pi^*) \rightarrow X^1A_1$ phosphorescence in the region of the $^1(\pi\pi^*) \leftarrow X^1A_1$ absorption band with the sample in a pulsed supersonic jet. Such an excitation spectrum is particularly interesting, since in a theoretical publication by Tatchen et al. [7] a 'dark' excited singlet state $^1(n\pi_2^*)$ state of B_1 symmetry was calculated to be in the vicinity of the $^1(\pi\pi^*)$ state in PT. The existence of such a state could strongly influence the vibronic coupling scheme of $^1(\pi\pi^*)$ away from the statistical limit towards the intermediate case. The dark $^1(n\pi_2^*)$ state is *a priori* not expected to be directly observable owing to an approximately 50 times smaller transition dipole moment than the $^1(\pi\pi^*) \leftarrow X^1A_1$ transition [7]. It may however manifest itself in the excitation spectrum due to its influence on $^1(\pi\pi^*)$, similar to the classic example of vibronic coupling of S_2 with S_1 in jet-cooled naphthalene [8], which exhibits a complex intermediate level structure in the $S_2 \leftarrow S_0$ excitation spectrum [9].

4.2 Experimental

The 4H–pyran–4–thione was synthesized according to a procedure given by Macdonald et al. [10,11], purified by repeated vacuum sublimation as is detailed in Section 2.3. The supersonic jet apparatus and the general experiment are described in Section 2.1. For all experiments PT was seeded into helium

at T=40°C and expanded at a reservoir pressure of 1 bar. The diameter of the pulsed nozzle was 0.8 mm and the excimer pumped dye laser (Lumonics) intercepted the molecular jet $\sim$ 13 mm downstream of the nozzle. For these expansion conditions and assuming velocity slip and stick conditions to be negligible, using Equations 2.14–2.20, the following parameters were obtained for PT molecules at the zone of laser excitation.

$$\begin{aligned} M &\simeq 20.8 \\ T_{trans(a)} &\simeq 2.15\text{K} \\ u &\simeq 1797\text{ms}^{-1} \\ u^{\infty} &\simeq 1803\text{ms}^{-1} \end{aligned} \tag{4.1}$$

The repetition rate of the laser was 8 Hz, its bandwidth was $\sim$ 0.3 cm^{-1} and a typical sampling rate was 50 shots per datapoint. The phosphorescence was detected between 15625 and 17850 cm^{-1} by a red-sensitive photomultiplier tube (Philips XP2254B) at right angles to the jet and to the laser beam using the photon counting method. The phosphorescence was selected using a combination of an interference filter (80 nm bandwidth, center wavelength 600 nm; Andover Corporation) and an optical cut-off filter (OG595; Schott Mainz), thereby scattered light from the excitation laser pulses was effectively suppressed. This arrangement is shown in Figure 3.1. For measuring the emission spectrum a spherical mirror arrangement in conjunction with two achromatic lenses was used to image the phosphorescence onto the entrance slit of a double monochromator (Jobin Yvon, 5-349 UV) with a spectral resolution of $\approx$ 5 cm^{-1}.

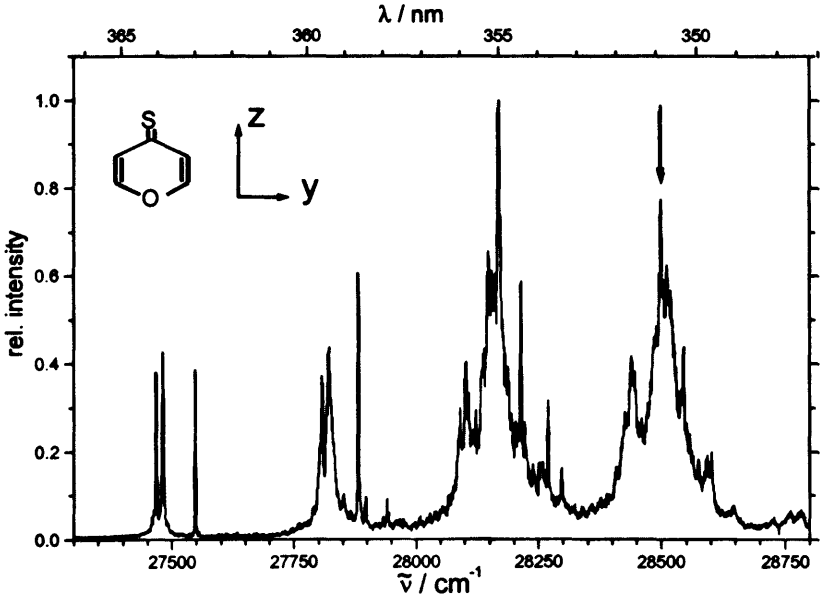


Figure 4.1: Excitation spectrum of the $^3(n\pi^*) \rightarrow$ X $^1A_1$ phosphorescence in the region of the $^1(\pi\pi^*) \leftarrow$ X $^1A_1$ absorption band between 27400 and 28800 cm^{-1}. The vertical arrow indicates the excitation wavenumber for the phosphorescence spectrum in Figure 4.2.

4.3 Results

The excitation spectrum of the $T_1 \rightarrow S_0$ phosphorescence of jet-cooled PT in the spectral range between 27300 and 28800 cm^{-1}, the region of the $^1(\pi\pi^*) \leftarrow X^1A_1$ absorption, is shown in Figure 4.1. The relative intensities of the spectrum are corrected regarding the excitation energy of the laser and the counting rate. Due to the fact that the observed phosphorescence was rather strong, combined with an efficient suppression of stray light owing to the big difference in the excitation and emission wavenumbers, a large signal-to-noise ratio of ≈ 100 or better was readily achieved. The expansion condition for the measurement assured that no features in the spectrum are due to hot bands and/or van der Waals complexes with the carrier gas helium (cf. next section). Thus, given the good signal–to–noise ratio, even very weak bands are confidently assigned to PT ground state absorptions. The excitation spectrum was also measured between 26400 and 27300 cm^{-1} (not shown in Figure 4.1), however no other absorption features were observable in that spectral region. The fact that the observed emission is indeed the $T_{1z,\nu''} \rightarrow S_{0,\nu'}$ phosphorescence from highly vibronically excited triplet states is demonstrated in Figure 4.2, which shows the dispersed emission spectrum upon excitation at 28499 cm^{-1} (marked by a vertical arrow in Figure 4.1). The main emission band (0–0 transition) is centred at ≈ 16836 cm^{-1}, which corresponds well with the 0–0 transition in the $T_{1z} \leftarrow S_0$ phosphorescence excitation spectrum at 16844 cm^{-1} [12]. The size of the observed emission signal is quite surprising since the phosphorescence must be due to mixed states of substantial triplet character at extremely high excess energies (> 10500 cm^{-1}) above the triplet origin in the isolated molecule. A similar result is known for jet-cooled fluoranthene, where the prompt $S_1 \rightarrow S_0$ fluorescence was observed at excess energies of $> hc \times 10400$ cm^{-1} above $S_{1,0}$, after $S_4 \leftarrow S_0$ excitation energy in fluoranthene [13].

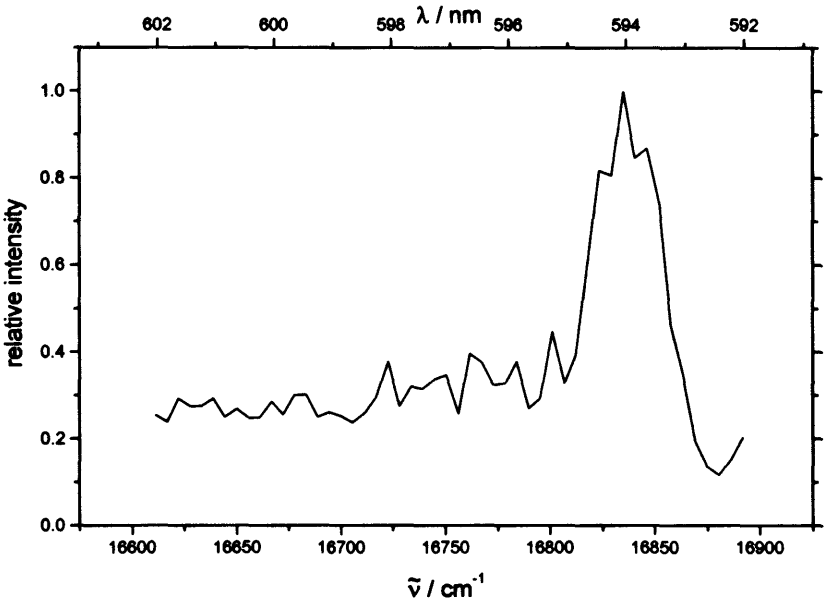


Figure 4.2: $^3(n\pi^*) \rightarrow ^1$ X phosphorescence spectrum upon excitation at 28499 cm^{-1} in P4 (line 35 in Table 4.1) of the $^1(\pi\pi^*) \leftarrow ^1$X band.

For the lifetime of the phosphorescence in Figure 4.2 a *lower limit* of $\sim 4-5$ μs was found, (see also Figure 4.3), which is not incompatible with the lifetime of 21 μs of the triplet substate T_{1z} in a Shpolskii matrix at 1.2 K [14]. An accurate determination of the phosphorescence lifetime was not possible because the excited molecules in the molecular jet travel out of the emission detection zone within the lifetime of the metastable triplet state T_{1z}, which causes the decay curves to deviate significantly from a monoexponential at times $> 10\mu$s. This can be seen in Figure 4.3 where the decay in phosphorescence as a function of time is plotted. In the example shown, the phosphorescence emission upon excitation at 28499 cm^{-1} has a lifetime of approximately 5μs.

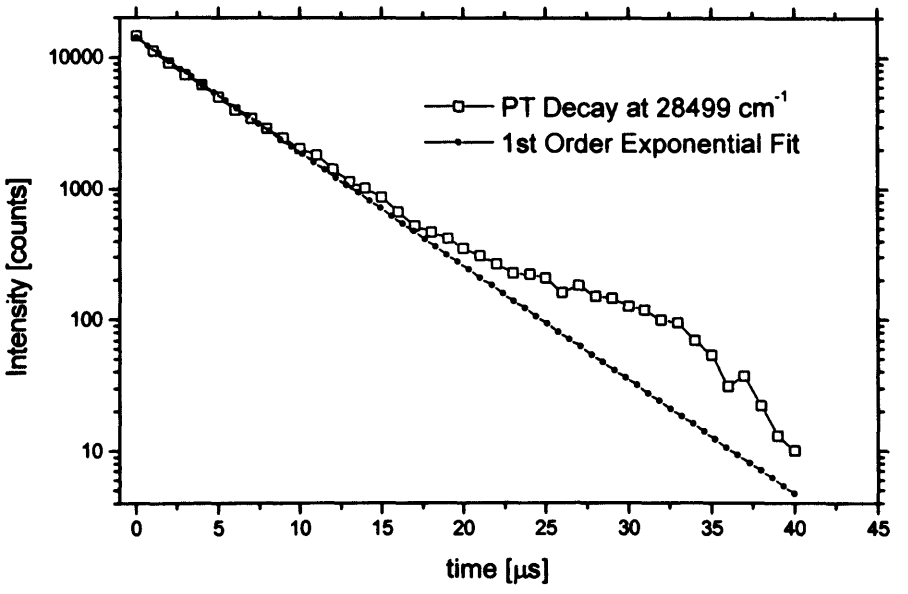


Figure 4.3: Decay of the $^3(n\pi^*) \rightarrow {}^1\mathrm{X}\ {}^1\mathrm{A}_1$ phosphorescence emission spectrum upon excitation at 28499 cm^{-1}.

4.4 Discussion

The phosphorescence excitation spectrum of isolated jet–cooled PT upon excitation into the $^1(\pi\pi^*) \leftarrow \mathrm{X}^1\mathrm{A}_1$ absorption band is shown in Figure 4.1. This spectrum exhibits a complex fine structure consisting in excess of 70 lines up to an energy of 28800 cm^{-1}. According to Maciejewski et al. [3], the energy between the first excited singlet state $^1(n\pi^*)$ and the $^1(\pi\pi^*)$ state is $\sim$ 9300 cm^{-1}. This large energy gap would lead one to conclude that the vibronic coupling between these two states would be in the statistical limit. This essentially means that the density of zeroth order vibronic states $^1(n\pi^*)_\nu$ with the same symmetry as the origin $^1(\pi\pi^*)_0$ form a quasi-continuum at the energy of $^1(\pi\pi^*)_0$. In this instance a well defined 0–0 transition with a Lorentzian profile should be observed. This is the situation that is observed for the coupling between S_2 and S_1 in BPT and XT and also in the classic example of azulene.

However, as can be seen from Figure 4.1, this is not the case. The 0–0

transition at around 27500 cm^{-1} is split into a fine structure of at least 10 lines. This fine structure is the first of a series of four energy regions (within the energy range measured) that show a pattern of similar splittings up to an energy of 1200 cm^{-1} above the origin. The origin was assigned to the spectral centre of the first pattern at 27499.3 cm^{-1}. This spectral origin $\tilde{\nu}_0$ was determined from the expression

$$\tilde{\nu}_0 = \frac{\sum I_i \tilde{\nu}_i}{\sum I_i}$$

where I_i and $\tilde{\nu}_i$ are the relative intensity and wavenumber of the ith line in P1, respectively, P1 being the first pattern. It is in effect the intensity weighted centre wavenumber.

In Figure 4.4 the four patterns P1 ... P4 are shown above each other for comparison. In this figure the major or most prominent lines are labelled. Not all are labelled to ease congestion and to aid with clarity, however all lines and wavenumbers along with their pattern assignment are given in Table 4.1.

The problem that must be addressed, given the large energy gap and that the similar congeners XT and BPT behave according to this energy gap rule, is why does PT appear to deviate from it and show such a complex structure? Possible reasons are listed below and are discounted.

1. **Rotational Fine Structure**

   The origin pattern P1 is not rotational fine structure because the energy separation between the strongest lines 3 and 5, as well as between lines 5 and 8 are 14.2 and 66.2 cm^{-1}, respectively. These ranges are too large to represent rotational energy spacings considering our expansion conditions.

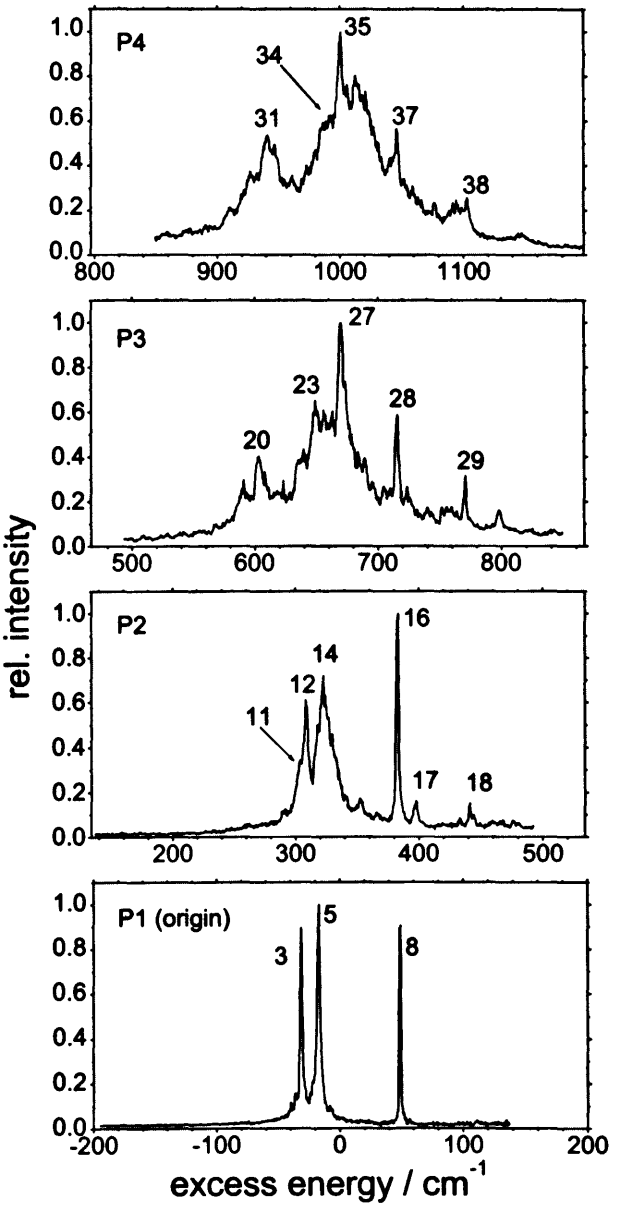


Figure 4.4: Comparison of the four patterns P1 to P4 in the spectrum, which are individually separated by 333 cm^{-1} according to the position of lines 8, 16, 28 and 37. The structures are due to strong vibronic coupling with lower lying dark levels of the $^1(n\pi_2^*)$ state. Wavenumbers of lines numbered 1–38 (several lines were not labelled for reasons of figure congestion) are listed in Tables 4.1 and 4.2 together with tentative assignments. Line numbering and assignments are not comprehensive.

2. **Vibronic Modes**

   As no features were observed in the region between 26400 and 27300 cm^{-1}, immediately below pattern P1, it is safe to assume that this pattern contains the origin. As the lowest energy mode of PT in the ground state and the first excited state was found to be $\sim$ 150 cm^{-1} [15], the features cannot be due to lower frequency vibronic modes.

3. **Hot Bands**

   The complex pattern in P1 could be accounted for by hot PT molecules but again this is unlikely due to the expansion conditions in the jet. Even if the lines were due to hot molecules one would not expect them to be so intense. Furthermore, these features are repeated at higher energies with greater intensities so therefore can almost certainly be ruled out as hot bands.

4. **Van der Waal Clusters**

   Cluster formation is a common occurrence in the expansion of seeded noble gases, an example of which is Reference [12]. Van der Waals clusters cause the absorption wavelengths of the isolated molecule to be shifted due to dipolar interactions. These shifts are well recorded and only result in small chromic shifts, i.e. clusters only result in wavelength shifts and not in complex fine structure. Due to the expansion conditions formation of van der Waals clusters are highly unlikely. Finally PT–Helium clusters have not yet been observed in supersonic expansions and thus can be ruled out as the cause of the observed complex structure.

Consequently, this complex structure is interpreted as strong intermediate vibronic coupling of $^1A_1(\pi\pi^*)$ with a 'dark' state $^1B_1(n\pi_2^*)$ [7] with its origin below $^1(\pi\pi_0^*)$.

In the intermediate coupling case the number of strongly mixed molecular eigenstates in P1, N_{ME}, can be estimated assuming no severe dispersion of the vibronic coupling matrix elements, ν_{sl} (cf. Section 1.3). This value of N_{ME} should coincide with the number of observed states in P1, N_{obs}. N_{obs} was found to be ≈ 10. In the strong intermediate case the Equations 1.10 and 1.16 hold and are shown here again:

$$k = \frac{2\pi}{\hbar}\langle\nu_{sl}\rangle^2\rho_l, \tag{1.10}$$

$$N_{ME} = \langle\nu_{sl}\rangle^2\langle\rho_l\rangle^2, \tag{1.16}$$

and using $\tau\Delta E \geq \hbar$, $\Delta E \geq \hbar/\tau = k\hbar$, Equation 1.10 becomes in terms of energy

$$\Gamma = 2\pi\langle\nu_{sl}\rangle^2\rho_l \tag{4.2}$$

where Γ corresponds to the half-width of P1, and ρ_l is the density of dark states $^1B_1(n\pi_2^*)_\nu$ at the origin. From Figure 4.4 it can be seen that the half width of P1 is$\approx$ 70 cm^{-1}. The density of dark states $^1B_1(n\pi_2^*)_\nu$ at the origin was found to be ≈ 0.3 (cm^{-1})$^{-1}$. The estimation of this value of ρ_l is explained in the next section and is illustrated in Figure 4.5. Inserting these values to Equations 1.10 and 1.16 above, one obtains a value of ~ 3 for N_{ME}. This is in satisfactory agreement with N_{obs} considering the absolute value of N_{obs} is quite small. This also indicates that the energy gap between the origins of the two vibronic states $^1(\pi\pi^*)_0$ and $^1(n\pi^*)_0$ is quite small. The criterion for the strong coupling case of intermediate case of large molecules of $\langle\nu_{sl}\rangle\langle\rho_l\rangle \gg 1$ is just about fulfilled; $10 \times 0.3 \cong 3.3 > 1$.

4.4.1 The hidden state $^1B_1(n\pi^*)$

According to Tatchen et al. [7], the $^1B_1(n\pi_2^*)$ state is a consequence of a transition of an n (b_2) electron to the lowest unoccupied molecular orbital of a_2

no.	wavenumber [cm^{-1}]	rel. int.	excess [cm^{-1}]	FWHM [cm^{-1}]	L.L. of lifetime ps	attribution identifier/pattern
1	27459.0	w	-40.3	1.9 ± 0.1	2.8 ± 0.2	A
2	27462.6	w	-36.7	1.4 ± 0.1	3.8 ± 0.3	B
3	27467.6	m	-31.7	2.0 ± 0.1	2.6 ± 0.1	C
4	27476.6	w	-22.7	4.1 ± 0.2	1.3 ± 0.1	D
5	27481.3	m	-18.0	2.6 ± 0.2	2.0 ± 0.1	E
6	27482.0	w/m	-17.3	2.9 ± 0.1	1.8 ± 0.1	F
7	27491.7	w	-7.6	2.8 ± 0.2	1.9 ± 0.1	G
8	27547.6	m	48.3	1.9* G		H
9	27549.1	w	49.8	2.9 ± 0.1	1.8 ± 0.1	I
10	27555.8	w	56.5	1.0 ± 0.1	5.3 ± 0.5	J
11	27802.6	w	303.3			B
12	27807.2	m	307.9			C
13	27817.0	m	317.7			D
14	27821.6	m	322.3			E
15	27828.8	m	329.5			G
16	27882.0	s	382.7	2.8*		H
17	27896.6	w	397.3	4.8*		K
18	27940.2	w	440.9	3.0*		L
19	28089.6		590.3			M
20	28102.2		602.9			N
21	28107.0		607.7			O
22	28122.0		622.7			P
23	28148.0	s	648.7			C
24	28155.0	s	655.7			D
25	28158.6	s	659.3			Q
26	28161.8	s	662.5			E
27	28169.4	s	670.1			G
28	28214.6	s	715.3	4.8*		H
29	28269.8	m	770.5			R
30	28425.8		926.5			M
31	28439.8		940.5			N
32	28445.6		946.3			O
33	28459.8		960.5			P
34	28489.8	s	990.5			C
35	28499.4	s	1000.1			Q
36	28502.2	s	1002.9			E
37	28545.2	m	1045.9			H
38	28601.8	w	1102.5			R

Table 4.1: List of spectroscopic features of the excitation spectrum in Figure 4.1. The data on P1 as shown in Figure 4.4 are comprehensive, whereas values for P2-P4 are limited to the most prominent bands. The origin was attributed to the center of P1 at 27499.3 cm^{-1}. Progression identifiers are listed in the last column. Abbreviations: L.L.= lower limit, w=weak (0-30%) , m=medium (30-50%), s=strong (50-100%) with respect to the strongest line of the spectrum, FWHM=full width at half maximum of Lorentzian profile fitted to the measured line - error limits are due to the fit procedure (non-linear least square Marquardt algorithm). Line 8 was fitted with a Gaussian profile. *For prominent isolated lines the FWHM was taken directly from the spectrum.

symmetry ($b_2 \otimes a_2 = b_1$). This dark state could not be placed definitively above or below the origin of the $^1(\pi\pi^*)$ excitation energy. It is clear from the complex structure of the 0–0 transition in Figure 4.1 that the $^1B_1(n\pi_2^*)_0$ must be below the $^1(\pi\pi^*)_0$. The structure revealed in the spectrum is due to the mixing of the zero-th order vibrationless $^1A_1(\pi\pi^*)_0$ state with a set of discrete zero-th order vibronic states $^1B_1(n\pi_2^*)_\nu$ with the same symmetry as the $^1A_1(\pi\pi^*)_0$ state. This means that b_1 vibrations of the dark state $^1B_1(n\pi_2^*)_\nu$ are involved in the coupling. From this information it is possible to estimate the origin of the $^1(n\pi_2^*)$ state.

In Section 1.3, it is stated that all vibronic states can be considered effective for coupling. Therefore, all the vibronic states of $^1B_1(n\pi_2^*)_\nu$ with symmetry b_1, N_{b_1}, in the region of the 0–0 transition should be approximately equal to $N_{obs} = 10$. All vibronic states of b_1 symmetry are considered effective. Vibronic states of other symmetries do not promote vibronic coupling and therefore are not considered. Therefore, the origin of $^1(n\pi_2^*)$ should be at an energy below $^1(\pi\pi^*)_0$ such that N_{b_1} is equal to or slightly greater than N_{obs} over the energy range of P1, which is 140 cm^{-1}. To evaluate this energy, all possible combinations of up to 15 vibrational quanta of all normal vibrations of PT were calculated up to an excess energy of $hc \times 6000$ cm^{-1}. The energies of the 27 normal vibrations used were from the ground state measurements of Somogyi [16]. Next, the number of combinations with b_1 symmetry per 140 cm^{-1}, N_{b_1} was extracted. This is shown in Figure 4.5. From this figure an estimation of $N_{b_1} = 10/140$ cm^{-1} is arrived at an excess energy of 825 cm^{-1}. This value is the energy above $^1(n\pi_2^*)_0$ at which $N_{b_1} = 10$ states per 140 cm^{-1} and corresponds to $(27499.3 - 825\ \text{cm}^{-1}) \approx 26675$ cm^{-1}. The density of $^1(n\pi_2^*)$ states, ρ_l, at 27499.3 cm^{-1} i.e. 825 cm^{-1} above the estimated $^1(n\pi_2^*)$ origin at 26675 cm^{-1} is ≈ 0.3 states per cm^{-1}. It is this value of ρ_l that was used in the previous section. This upper limit of 26675 cm^{-1} can be bounded by assuming

an uncertainty in N_{b_1} such that N_{b_1} = 15 states/140 cm^{-1}. This occurs at an excess energy of 1025 cm^{-1}, thus the lower limit of $^1(n\pi_2^*)_0$ is at 26475 cm^{-1}.

To confirm these values, the number of lines in P2 were also used. In P2, 19 lines were observed assuming they were based on a_1 vibrations in $^1(\pi\pi^*)$. Therefore, 19 states/140 cm^{-1} for N_{b_1} in P2 corresponds to excess energies of between $\sim$ 1080 and $\sim$ 1140 cm^{-1} and places the upper limit of $^1(n\pi_2^*)_0$ at 26695 cm^{-1} which is in good agreement with that calculated above.

Tatchen et al. [7] give two values for the energy separation ΔE. These are based on geometry optimised calculations on the ground state and first excited triplet state. This energy separation places $^1(n\pi_2^*)_0$ at either $hc \times 1690$ cm^{-1} below or at $hc \times 890$ cm^{-1} above $^1(\pi\pi^*)_0$. This first value is supported by the above interpretation and the second value can be rejected. Therefore, $^1(n\pi_2^*)$ should be attributed to the second excited singlet state S_2, whereas $^1(\pi\pi^*)$ is in fact the third excited singlet state S_3.

The origin of $^1(\pi\pi^*)$ of PT in a perfluoroalkane at room temperature is at an energy of $hc \times 27490$ cm^{-1} [3]. This is almost identical to the value found in the isolated molecule in the supersonic jet. In general, chromic shifts are encountered when changing the polarity of solvent in which the molecule of interest is dissolved. On going from polar to less polar solvents, $\pi^* \leftarrow \pi$ transitions are expected to shift to higher energies. Conversely, $\pi^* \leftarrow n$ transitions shift to lower energies. In this case, PT is going from a polar solvent (perfluoroalkane) to a less polar solvent (molecules are isolated). As the energy of the origin does not change significantly, this lends support to the fact that the states involved in the transition are of mixed $n\pi^*/\pi\pi^*$, where one hypsochromic shift cancels out the other bathochromic shift.

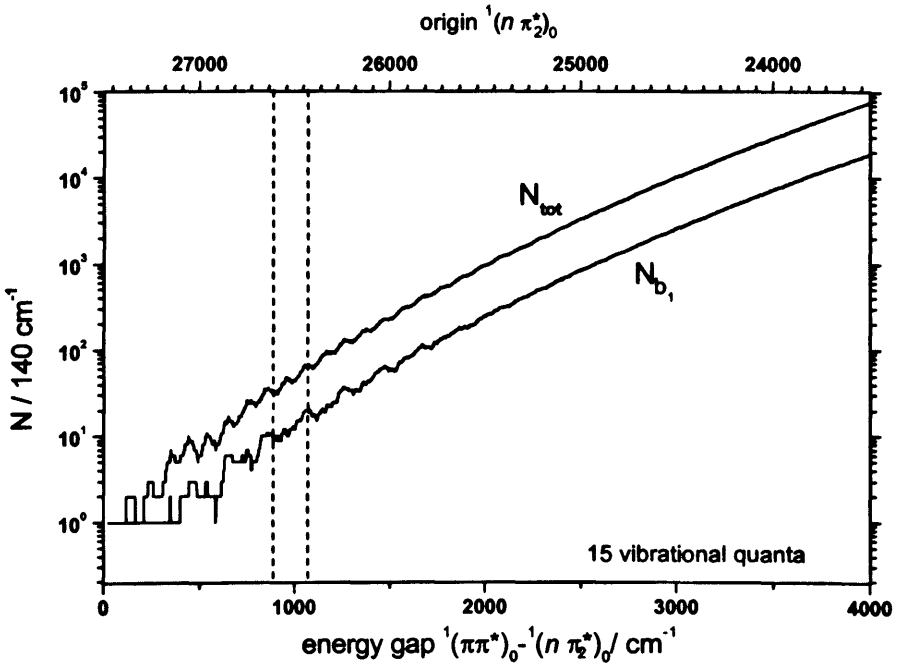


Figure 4.5: Excess energy dependence of the number of vibronic states with b_1 symmetry and the total number of states N_{tot} integrated over 140 cm^{-1}. Numbers were determined by a purely combinatorical calculation based on the frequencies of the ground state normal vibrations in PT [16]. The vertical dashed lines indicate the estimated range for the spectral position of the origin of the dark state $^1(n\pi_2^*)$ - upper axis.

	P1	$\Delta\tilde{\nu}/cm^{-1}$	P2	$\Delta\tilde{\nu}/cm^{-1}$	P3	$\Delta\tilde{\nu}/cm^{-1}$	P4
A	2	339.8	11				
B	3	339.6	12	340.8	23	341.8	34
C	4	339.8	13	338	24		
D	5	339.8	14	340.2	26	340.4	36
E	7	338.2	15	340.6	27		
F	8	334	16	332.6	28	330.6	37
G					25	340.8	35
H					29	332	38
M					19	336.2	30
O					21	338.6	32
P					22	337.8	33

Table 4.2: Selection of the most prominent progressions and combinations across all patterns P1...P4. Line numbers and assignments (A...P) are taken from Table 4.1.

4.4.2 Vibronic Structure

Due to the complexity of the intermediate level structure, it is difficult to obtain any quantitative and unambiguous spectroscopic information from Figure 4.1. Therefore, the following vibrational analysis is of a qualitative nature and only discusses the most prominent features and their likely assignments. As seen in Figure 4.1, there are four patterns of irregularly spaced features with varying intensities when looked at individually. However, when viewed collectively, there are a number of repetitive features. Thus, the totally symmetric modes in $^1(\pi\pi^*)$ and $^1(n\pi_2^*)$ have similar frequencies. Harmonic progressions are present in the spectrum with lines 8(P1), 16(P2), 28(P3), and 37(P4) separated by 333 cm^{-1}, lines 3(P1), 12(P2), 23(P3) and 34(P4) as well as lines 5(P1), 14(P2), 26(P3) and 36(P4) all separated by 340 cm^{-1}. In fact, separations of 330 cm^{-1} and 340 cm^{-1} occur in other combinations over a large part of the spectrum and these are shown in Table 4.2. The first symmetric a_1 vibration in PT occurs at 420 cm^{-1} in the ground state [16] and at 472 cm^{-1} in the first excited triplet state ([12] and Table 5.1 Chapter 5). The next totally symmetric vibration occurs at 722 cm^{-1} so therefore the main absorption lines forming

the harmonic progressions in P2, P3 and P4 are therefore likely to be based upon the first symmetric a_1 vibration in PT at 420 cm^{-1}. This means that the first totally symmetric a_1 vibration in $^1(\pi\pi^*)$ possesses $hc \times 80 - 90$ cm^{-1} less energy than in S_0 or T_1. There exists a vibration in the ground state of PT with an energy of 300 cm^{-1}. This has symmetry b_2 (see Table 5.1, Chapter5). However, this vibration is unlikely to be involved in the above progression for the following reasons:

1. In order for this vibration to be involved in coupling it must interact with a vibronic state in $^1(n\pi_2^*)$ with the same symmetry, b_2. For this to occur the coupling vibration in $^1(n\pi_2^*)$ must be of a_2 symmetry, as $^1(n\pi^*)_0$ has B_1 symmetry, $a_2 \otimes B_1 = b_2$. However, out-of-plane $a_2$symmetry vibrations in C_{2v} molecules cannot involve motion of the atoms on the C_2 axis and therefore are ineffective at mixing states localised on the C=S group.

2. In the previous work on the triplet state by Ruth et. al [12] this vibration is not observed in the triplet state.

The difference of $\approx$ 7 cm^{-1} between the two observed progression forming energies of 333 cm^{-1} and 340 cm^{-1} may be due to resonance splittings, and does not need another vibration to explain it.

Other modes besides those based on 333 cm^{-1} and 340 cm^{-1} appear in P3 and P4. Similar to the above splitting, a set of lines is found based on 590 and 625 cm^{-1}. This the totally symmetric ring mode with C=S bend character which is found at 722 cm^{-1} in the ground state and at 697 cm^{-1} in the first excited triplet state, again see Table 5.1, Chapter 5. Also a set of lines are found between 925 and 960 cm^{-1}. These are tentatively assigned to the combination of the two lowest totally symmetric vibrations in $^1(\pi\pi^*)$ with the splitting caused by the vibronic coupling with $^1(n\pi^*)$. A list of combinations is given in Table 4.2.

Due to the coupling, the individual intensities of the vibronic transitions of $^1(\pi\pi^*)$ are much lower than if the coupling were in the statistical limit. The integrated intensities of each pattern should approximate the intensities of the decoupled spectrum. These intensities are in the order P1 < P2 < P3 > P4 and scale approximately as 1 : 2 : 4 : 3.8. This suggests a broad Franck–Condon pattern which in turn suggests that the excited state geometry is significantly different for the active vibrations involved. This is supported by the previously found difference of $hc \times 80 - 90$ cm^{-1} to lower energy for the first two a_1 vibrations in the excited state compared to the ground state.

4.4.3 Linewidths and Relaxation Dynamics

In Table 4.1 two columns showing the Full Width at Half Maximum (FWHM) and lifetimes of lines in pattern P1 are listed. Although these lines experience inhomogeneous broadening due to the incomplete rotational cooling in the jet and the limited instrumental resolution, they are in fact quite narrow. These broadened lines were fitted with a series of Lorentzian profiles to establish an upper limit to the FWHMs, as shown in Figure 4.6. With the exception of line 8, which is better represented by a Gaussian lineshape, the Lorentzian fits are quite good. From the FWHM, the lifetimes can be derived using the following equation:

$$\Delta\tau\Delta E \geq \hbar \tag{4.3}$$

As these linewidths are longer than the natural linewidths and also from the above inequality it follows that these lifetimes are lower limits. However, the real lifetimes are only slighter longer than those derived from the observed linewidths.

1. In Ruth et. al [17] and in Figures 5.7 and 5.8, the $T_{1z} \leftarrow S_0$ transition is

shown. This exhibits a typical rotational envelope[1]. This was recorded under similar conditions by direct excitation into the first excited triplet state manifold. Therefore, if the homogeneous linewidths of the rotational states were much narrower than those derived by the Lorentzian fits above, rotational fine structure should be present in the spectrum at the above experimental resolution. As no such rotational fine structure is observed, this lends weight to the argument that the natural linewidths are only slightly less.

2. According to Maciejewski et. al [3], the lifetime of $^1(\pi\pi^*)$ in perfluoroalkane solution at room temperature has an upper limit of $\approx$ 20 ps. This, therefore, gives an homogeneous linewidth of 0.27 cm^{-1}, which is in agreement with the values detailed in Table 4.1.

3. Ruth et. al [19] investigated the $S_1 \leftarrow S_0$ transition of azulene in a supersonic jet. They found that the rotationally broadened structure of the 0–0 transition could be described by a Lorentzian profile with a halfwidth of $\approx$ 5.6 cm^{-1} based on a homogeneous FWHM of 4 cm^{-1}. This is further support to the above argument.

The interest in PT originated in it's unusual photophysical properties (as is that of XT and BPT). Maciejewski et. al [3] state that PT is also an exception to the energy gap law [20]. This law is described in Section 1.2 and states that as the energy gap between $^1(n\pi^*)$ and $^1(\pi\pi^*)$ increases linearly, the rate of non-radiative decay decreases exponentially. It was suggested in [3] that upon excitation into $^1(\pi\pi^*)$ substantial geometric change occurs due to its low rigidity and hence PT does not obey the energy gap law. However, MacDonald et. al [10] through microwave spectroscopy and Tatchen et. al [7]

[1]Ruth et. al [17,18] assert that it is an A–type envelope. The rotational envelope will be dealt with in more detail in Chapter 5.

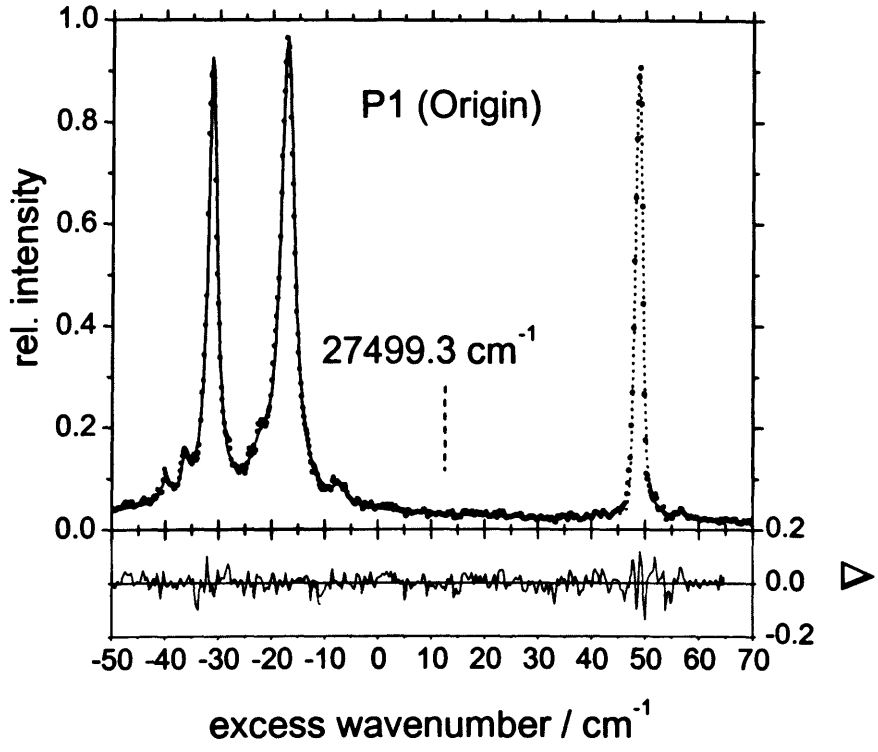


Figure 4.6: Fit of Lorentzian profiles as empirical representation of the lines A-H in the origin pattern, P1. FWHM and centre wavenumbers of the respective lines are listed in Table 4.1. The lower part of the figure shows the weighted residuals Δ of the fit.

through geometry optimisations on the ground state and first excited triplet state, suggest that PT is planar in both states. Thus, it is more likely that rather than geometric alteration upon excitation, it is the presence of the nearby $^1(n\pi_2^*)$ state and its coupling to the $^1(\pi\pi^*)$ that governs the dynamic behaviour at excitation energies $> hc \times 27500$ cm^{-1}. This nearby state lessens the Franck–Condon inhibition of radiationless relaxation from higher excited states and thus explains the lower $^1(\pi\pi^*) \rightarrow X^1A_1$ fluorescence quantum yield of PT compared to those of XT and BPT. Not only can the high ISC quantum yield be explained by strong direct SO coupling between $^1(\pi\pi^*)$ and $^3(n\pi^*)$ whose matrix element $\langle ^1(\pi\pi^*)|H_{SO}|^3(n\pi^*)\rangle = -126.1$ cm^{-1} [7], but also by a relaxation channel involving $^1(n\pi_2^*)$. The violation of the energy gap law is determined by the molecular energy redistribution. If the ISC process was solely dominated by direct SO coupling between $^1(\pi\pi^*)$ and $^3(n\pi^*)$, $^1(n\pi_2^*)$ would only influence the structure of the excitation spectrum. It is proposed that an alternative pathway of efficient irreversible intramolecular redistribution of initially excited eigenstates to high vibronic states $^3(n\pi^*)_\nu$ of the first excited triplet state exists, and it is likely to proceed via $^1(n\pi_2^*)$ and the third excited triplet state $T_{3z} \equiv ^3B_2(\pi\pi_2^*)$. The existence and relevance of this decay channel is outlined below.

1. Strong vibronic coupling of $^1(\pi\pi^*)$ with $^1(n\pi_2^*)$ populates a set of molecular eigenstates of $^1(\pi\pi^*)$ and $^1(n\pi_2^*)$ states. This is evinced by the small chromic shift outlined in the previous section.

2. Tatchen and Marian [21] calculated the SO coupling matrix element $\langle ^1B_1(n\pi_2^*)|H_{SO}|^3B_2(\pi\pi_2^*)\rangle = 154.1$ cm^{-1}, which is larger than that for $\langle ^1(\pi\pi^*)|H_{SO}|^3(n\pi^*)\rangle$ and thus ISC from the dark $^1(n\pi_2^*)$ to T_{3z} can be very efficient. Therefore, the population of $^1(n\pi_2^*)$ states are not rate limiting. Furthermore,the position of T_3 was calculated to be approximately

at the same excitation energy as $(n\pi_2^*)$ [7].

3. Internal conversion from T_{3z} to highly vibronically excited triplet states $T_{1z,\nu}$ takes place, as $T_{1z,\nu'} \rightarrow S_{0,\nu'}$ phosphorescence is readily observed. Unfortunately no further information on the efficiency of the IC process $T_{3z} \rightsquigarrow T_{1z}$ is available. The rate of the IC must be very fast in order to make this proposed decay channel feasible.

4. Direct ISC from $^1(n\pi_2^*)$ to T_{1z} is unlikely to be effective due to the very small value of $\langle ^1(n\pi_2^*)|H_{SO}|^3(n\pi^*)\rangle = 0.0005$ cm^{-1} [21]. The second excited triplet $T_2 \equiv ^3A_1(\pi\pi^*)$ appears to play no role in the intramolecular relaxation pathway on the basis of the small SO coupling matrix element $\langle ^1B_1(n\pi_2^*)|H_{SO}|^3A_1(\pi\pi^*)\rangle = -0.04$ cm^{-1} [21].

It is assumed that the main contributions to the observed linewidths are due to fast irreversible ISC to the triplet manifold. This assumption accords with the long lifetime of the observed red-shifted emission, which is due to the general prohibition of spin-forbidden transitions and not a consequence of the vibronic coupling as for instance reported in the case of ovalene's S_2 state [22]. The fact that the observed linewidths do not vary drastically over the excitation range has two consequences: Firstly, it is a sign that in this region no conical intersection of the potential surfaces of $^1(\pi\pi^*)$ and $^1(n\pi_2^*)$ is present, which is also indicated by the weak background in the spectrum. The weak background is a consequence of the spectrum being based on sparse low energy vibronic states of a_1 symmetry in $^1(\pi\pi^*)$, so that all the patterns are well separated and no dramatic overlapping of lines is observed. The possible occurrence of a conical intersection at somewhat higher excess energies would not be too surprising considering the proximity of the states and the increasing intensities of lines in the spectrum. Secondly, the observed linewidths indicate that the phosphorescence quantum yield is probably not strongly dependent on the

excitation energy in that region. This hypothesis could be tested through comparison of Figure 4.1 with an absorption spectrum in the excitation range.

4.5 Conclusions

The $T_1 \rightarrow S_0$ phosphorescence excitation spectrum was measured upon absorption in $^1(\pi\pi^*) \leftarrow X^1A_1$ band of jet–cooled PT up to an excess energy of $\approx hc \times 1200$ cm^{-1} above the 0–0 transition, which is located around $\approx hc \times 27500$ cm^{-1}. An intermediate level structure was found, which is due to the strong vibronic coupling of $^1(\pi\pi^*)$ with a dark $^1(n\pi_2^*)$ state at lower energy. The energy gap between the two states has been estimated to be approximately $hc \times 825 - 1025$ cm^{-1}. Hence $^1(n\pi_2^*)$ should be attributed to the second excited singlet state S_2 in PT, whereas $^1(\pi\pi^*)$ appears to be the third excited singlet state S_3.

Four repetitive patterns of transitions were found in the spectrum and several progressions of mixed states across the pattern were identified and tentatively assigned. Through evaluation of the linewidths in the origin pattern a lower limit of the lifetime of the highly mixed states was estimated to be ≈ 4 ps. A fast decay channel involving the states $^1(n\pi_2^*)(\equiv S_2)$ and $^3(\pi\pi_2^*)(\equiv T_3)$ was suggested in order to explain the violation of the energy gap law in comparison to other aromatic thiocarbonyl compounds.

Bibliography

[1] A.L. Motyka and M.R. Topp. *Chem. Phys.*, 121:405–417, 1988.

[2] H.K. Sinha and R.P. Steer. *J. Mol. Spectrosc.*, 181:194–206, 1997.

[3] A. Maciejewski, A. Safarzadeh-Amiri, R.E. Verrall, and R.P. Steer. *Chem. Phys.*, 87:295, 1984.

[4] A.A. Ruth, F.J. O'Keeffe, R.P. Brint, and M.W.D. Mansfield. *Chem. Phys.*, 217:83–98, 1997.

[5] A.A. Ruth, T. Fernholz, R.P. Brint, and M.W.D. Mansfield. *Chem. Phys. Lett.*, 287:403–411, 1998.

[6] M. Szymanski, R.P. Steer, and A. Maciejewski. *Chem. Phys. Lett.*, 135(3):243–248, 3 April 1987.

[7] J. Tatchen, M. Waletzke, C.M. Marian, and S. Grimme. *Chem. Phys.*, 264:245, 2001.

[8] S.M. Beck, D.E. Powers, J.B. Hopkins, and R.E. Smalley. *J. Chem. Phys.*, 73(5):196–202, 1 Sept 1980.

[9] J. Wessel and D.S. McClure. *Mol. Cryst. Liq. Cryst.*, 58:121–153, 1980.

[10] J.N. MacDonald, S.A. Mackay, J.K. Tyler, A.P. Cox, and I.C. Ewart. *J. Chem. Soc., Faraday Trans. 2*, 77:79–99, 1981.

[11] B.S. Pedersen, S. Scheibye, N.H. Nilsson, and S.-O. Lawesson. *Bull. Soc. Chim. Belg.*, 87(3):223–228, 1978.

[12] A.A. Ruth, F.J. O'Keeffe, M.W.D. Mansfield, and R.P. Brint. *J. Phys. Chem. A*, 101(42):7735–7741, 1997.

[13] A.A. Ruth and M.T. Wick. *Chem. Phys. Lett.*, 266:206–216, 1997.

[14] M.-R. Taherian and A.H. Maki. *Chem. Phys. Lett*, 96:541, 1983.

[15] M.R. Taherian and A.H. Maki. *Chem. Phys.*, 68:179–189, 1982.

[16] Á. Somogyi, G. Jalsovszky, C. Fülöp, J. Stark, and J.E. Boggs. *Spectrochim. Acta*, 45A:679, 1989.

[17] A.A. Ruth, W.G. Doherty, and R.P. Brint. *Chemical Physics Letters*, 352:191–201, 2002.

[18] A.A. Ruth, T. Fernholz, M.W.D. Mansfield, and R.P. Brint. *J. Mol. Spectrosc.*, 214:80–86, 2002.

[19] A.A. Ruth, E.-K. Kim, and A. Hese. *Phys. Chem. Chem. Phys.*, 1:5121, 1999.

[20] R. Englman and J. Jortner. *J. Mol. Phys.*, 18:145, 1970.

[21] J. Tatchen and C.M. Marian. private communication.

[22] A. Amirav, U. Even, and J. Jortner. *J. Phys. Chem.*, 74:3745, 1981.

Chapter 5

Vibronic Lineshape of 4–*H*–Pyran–4–thione

5.1 Introduction

Recently in this laboratory the relatively new technique of cavity ring–down spectroscopy was introduced. This highly sensitive technique as described in Section 2.2 has given rise to many new innovative applications, publications and several reviews [1–4]. Ruth et. al. [5] investigated the weak $S_0 \rightarrow T_1$ transition of BPT in a supersonic jet by means of CRD spectroscopy. The CRD technique has been used to study the spectra of the triplet manifolds of large aromatic thiones, jet-cooled or in static cell [6,7] that could not be studied by laser-induced phosphorescence owing to having a very small phosphorescence quantum yield. CRD spectra are measurable for any system with the correct magnitude of the product of the absorption cross-section and the concentration, see Chapter 2, and in these cases the compounds have a sufficiently large vapour pressure to compensate for the very small cross section.

A demonstration of the sensitivity of the CRD technique is provided by the example of the extremely weak visible band transition of O_2 $b\ ^1\Sigma_g^+(\nu' =$

2) ← $X\ ^3\Sigma_g^-(\nu'' = 0)$. This transition is spin and spatially forbidden. Being $g \leftrightarrow g$ it is strictly electric dipole forbidden in a diatomic molecule and therefore can only gain intensity through a magnetic dipole transition and through spin–orbit mixing. It is therefore extremely weak. There is no difficulty, however, in achieving a sufficient gas pressure to compensate for the small cross-section and the spectrum in a static gas cell shown in Figure 5.1. This measurement was used as a test case for a CRD apparatus that was commissioned for the Technische Universität–Berlin. The aim of this project in Berlin was to measure the absorption spectrum of large polyaromatic hydrocarbons (PAHs) and their ions to determine if these molecules are responsible for the diffuse interstellar bands. The first PAH to be studied using this system was 1,4-diaminoanthraquinone (DAAQ), Figure 5.2. It was hoped that by heating the sample one could obtain enough sample in the gas phase to allow an absorption spectrum to be recorded. Unfortunately, this failed due to condensation of DAAQ on the cold mirrors. Since then, the system has been used to measure the $S_0 \rightarrow S_1$ transition in jet–cooled azulene [8] and the the $S_0 \rightarrow T_1$ absorption of PT in the static gas [9]. Ruth et al. [9] overcame a number of difficulties in measuring the $S_0 \rightarrow T_1$ transition of PT in the static gas at room temperature. The most important of these difficulties was subliming sufficient quantities of the sample molecule into the gas phase and taking into account the condensation of the sample over the time scale of the experiment. Briefly, an amount of PT was sublimed into the cavity which was heated externally. Measuring the 0–0 transition repeatedly over a time range of 150 minutes, they were able to extract the dependence of the number of molecules in the gas phase ($\propto$ intensity of absorption) with respect to time. In effect, a decay time of PT concentration due to the condensation was measured. Next, an accurately known amount of PT was sublimed into the cavity and the absorptions of 16 reasonably strong transitions were recorded over a

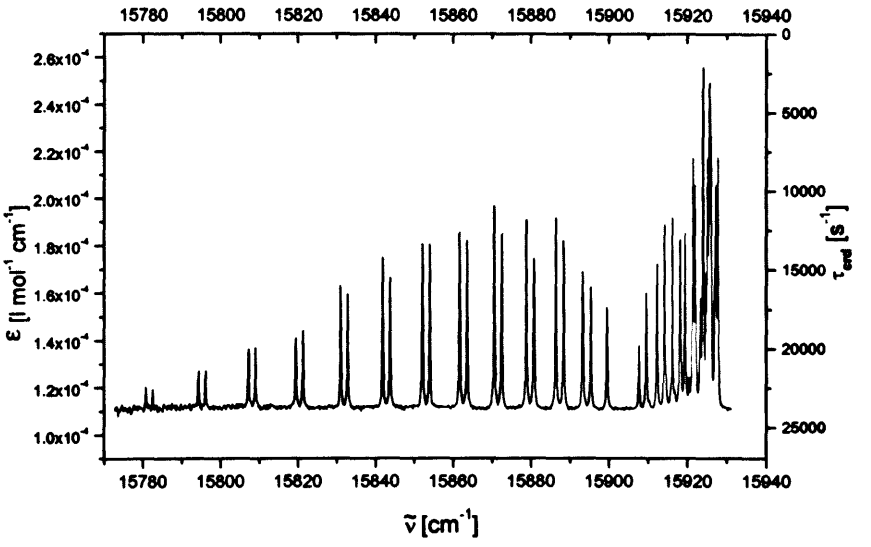


Figure 5.1: The CRD absorption spectrum of the visible band transition of O_2 $b\ ^1\Sigma_g^+(\nu' = 2) \leftarrow X\ ^3\Sigma_g^-(\nu'' = 0)$ in a static cell at 1180 mbar.

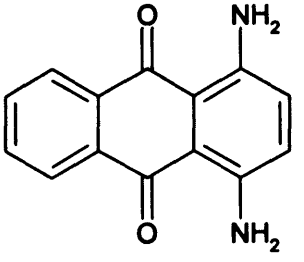


Figure 5.2: 1,4-diaminoanthraquinone (DAAQ)

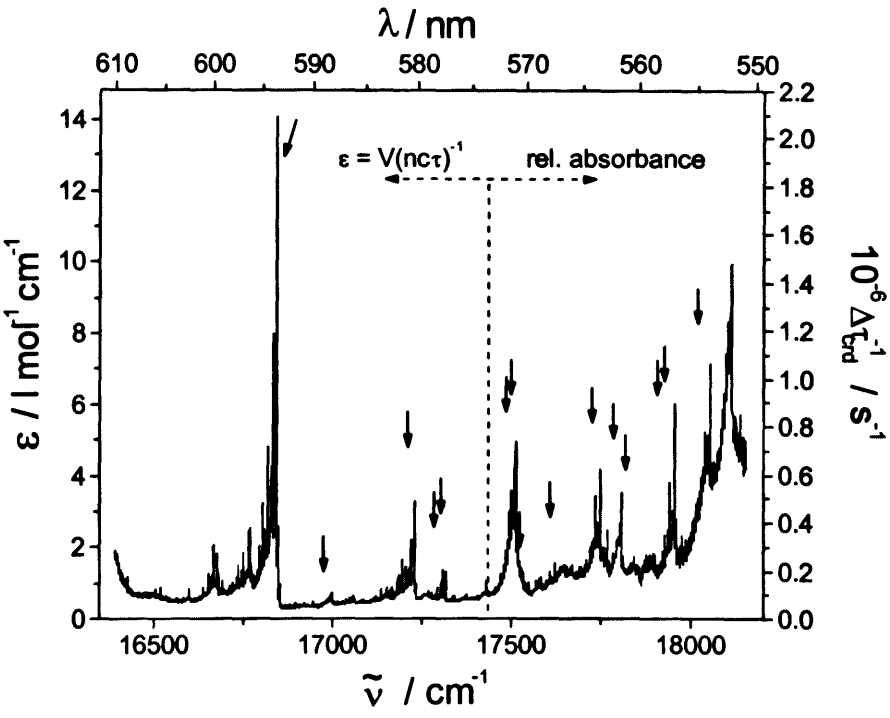


Figure 5.3: Cavity ring–down absorption spectrum of PT at room temperature. The absolute extinction scale (ϵ, left axis) refers to the low energy part of the spectrum ($\leq$ 17450), the relative absorbances ($\Delta\tau_{crd}^{-1}$, right axis) refers to the high energy part of the spectrum ($>$ 17450). The arrows indicate absorption features which were observed in the $S_0 \rightarrow T_1$ phosphorescence excitation spectrum of jet–cooled PT in Ref. [10]. Excitation wavenumbers are vacuum corrected.

50 minute period. These 16 absorptions were then corrected for condensation effects described above. These corrected absorptions were then used to scale the whole spectrum. This spectrum is shown in Figure 5.3.

When analysing this spectrum use was made of previously published reports on the ground state vibrations [11] and of the $S_0 \rightarrow T_1$ transition in a supersonic jet [10]. In both these publications and indeed in the room temperature CRD paper [9] the molecular plane is taken to lie in the xy-plane which is not the IUPAC recommended coordinate system for C_{2v} symmetry. Table 5.1 shows these assignments. In this thesis the molecular plane is the yz-plane

and the third column in Table 5.1 shows the reassignment of vibrations based on this molecular plane.

The CRD absorption spectrum of PT cooled in a supersonic jet was also measured and the $T_{1z,0} \leftarrow S_{0,0}$ line is shown in Figure 5.5. A comparison of the three lines recorded by absorption in a static cell, through phosphorescence excitation in a jet and by absorption in a jet is shown in Figure 5.4.

5.2 Vibronic Lineshape Analysis

The cavity ring down absorption spectrum of the origin line of the $T_{1z,\nu=0} \leftarrow S_{0,\nu=0}$ of PT in a molecular jet is shown in Figure 5.5. This is the first line of the spectrum shown in Figure 5.4(B). The lineshape encompasses a very large number, the order of one thousand, of rotational transitions. The bandwidth of the dye laser used in the CRD experiment was 0.3 cm^{-1} and therefore the line shape is fully resolved under the experimental conditions. The bandwidth of the laser is larger than the line broadening of individual state-state rotational transitions in the jet. It would be extremely difficult to achieve a significantly more resolved line shape. It would require extreme jet conditions and a very narrow bandwidth laser to make the experimental resolution narrower than the rotational line separation in the line shape.

Were such extreme conditions achievable it would be possible to analyse the pattern of individual rotational transitions to obtain very detailed information on the ground and excited states involved in the transitions by the usual process of rotational structure assignment. In this Chapter an attempt is made to obtain some of this information using the less than fully resolved data available.

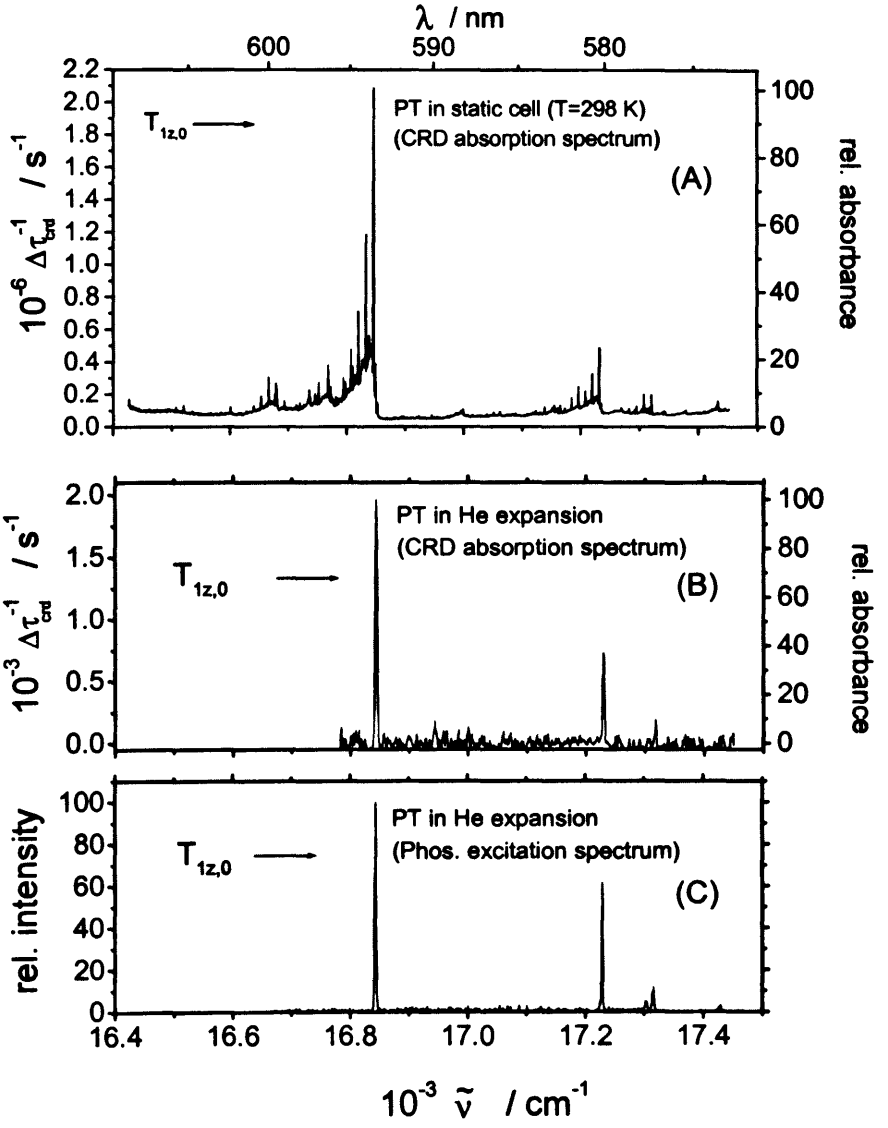


Figure 5.4: Comparison of the $T_{1z,0} \leftarrow S_{0,0}$ line in a static cell absorption, through phosphorescence excitation in a jet and through absorption in a jet.

$S_{0,\nu}$, Ref. [11]				$T_{1z,\nu}$, Ref. [10]			This thesis $T_{1z,\nu}$		
Description	energy [cm^{-1}]	sym.	vib. no.	energy [cm^{-1}]	sym.	vib. no.	energy [cm^{-1}]	sym.	vib. no.
ν_{CH}	3100	a_1	ν_1		a_1	ν_1		a_1	ν_{10}
ν_{CH}	3072	a_1	ν_2		a_1	ν_2		a_1	ν_9
$\nu_{C=C}$	1646	a_1	ν_3	1719.1	a_1	ν_3		a_1	ν_8
β_{CH}	1426	a_1	ν_4	1416.8	a_1	ν_4		a_1	ν_7
$\beta_{CH} + \nu_{C=S}$	1226	a_1	ν_5	1212.0	a_1	ν_5	1210.4	a_1	ν_6
$\beta_{ring} + \nu_{C=S}$	1168	a_1	ν_6	1202.2	a_1	ν_6	1206.4	a_1	ν_5
$\beta_{CH} + \beta$ring	1018	a_1	ν_7	1105.4	a_1	ν_7	1108.9	a_1	ν_4
$\nu_{CO} + \beta_{ring}$	918	a_1	ν_8	899.0	a_1	ν_8	902.5	a_1	ν_3
$\nu_{C=S} + \beta_{ring}$	722	a_1	ν_9	697.3	a_1	ν_9	700.9	a_1	ν_2
β_{ring}	420	a_1	ν_{10}	471.9	a_1	ν_{10}	470.2	a_1	ν_1
γ_{CH}	953	a_2	ν_{11}	958.4	a_2	ν_{11}	961.9	a_2	ν_{13}
γ_{CH}	801	a_2	ν_{12}	793.8	a_2	ν_{12}	792.5	a_2	ν_{12}
τ_{ring}	400	a_2	ν_{13}	459.6	a_2	ν_{13}	460.9	a_2	ν_{11}
ν_{CH}	3100	b_1	ν_{14}		b_1	ν_{14}		b_2	ν_{27}
ν_{CH}	3072	b_1	ν_{15}		b_1	ν_{15}		b_2	ν_{26}
$\nu_{C=C}$	1552	b_1	ν_{16}	1549.4	b_1	ν_{16}		b_2	ν_{25}
$\nu_{C-C} + \nu_{CO}$	1399	b_1	ν_{17}	1412.1	b_1	ν_{17}		b_2	ν_{24}
$\beta_{CH} + \nu_{CO}$	1301	b_1	ν_{18}	1337.7	b_1	ν_{18}		b_2	ν_{23}
β_{CH}	1232	b_1	ν_{19}	1263.3	b_1	ν_{19}	1263.4	b_2	ν_{22}
$\nu_{CO} + \beta_{CH}$	1021	b_1	ν_{20}	1110.5	b_1	ν_{20}	1113.9	b_2	ν_{21}
β_{ring}	648	b_1	ν_{21}	673.0	b_1	ν_{21}	671.2	b_2	ν_{20}
$\beta_{C=S}$	300	b_1	ν_{22}		b_1	ν_{22}		b_2	ν_{19}
γ_{CH}	963	b_2	ν_{23}	995.2	b_2	ν_{23}	998.3	b_1	ν_{18}
γ_{CH}	814	b_2	ν_{24}	815.0	b_2	ν_{24}		b_1	ν_{17}
$\tau_{ring} + \gamma_{C=S}$	685	b_2	ν_{25}	663.5	b_2	ν_{25}	666.0	b_1	ν_{16}
$\gamma_{C=S} + \tau_{ring}$	415	b_2	ν_{26}	385.7	b_2	ν_{26}	385.2	b_1	ν_{15}
τ_{ring}	94	b_2	ν_{27}		b_2	ν_{27}	152.3	b_1	ν_{14}

Table 5.1: Revised symmetry and vibronic labelling for PT. The notation for the Description column, column 1, is given in Table 2, Ref [11]. Energies given in columns 2, 4 and 7 are energies above the electronic origins $S_{0,0}$, $T_{1z,0}$ and $T_{1z,0}$ respectively.

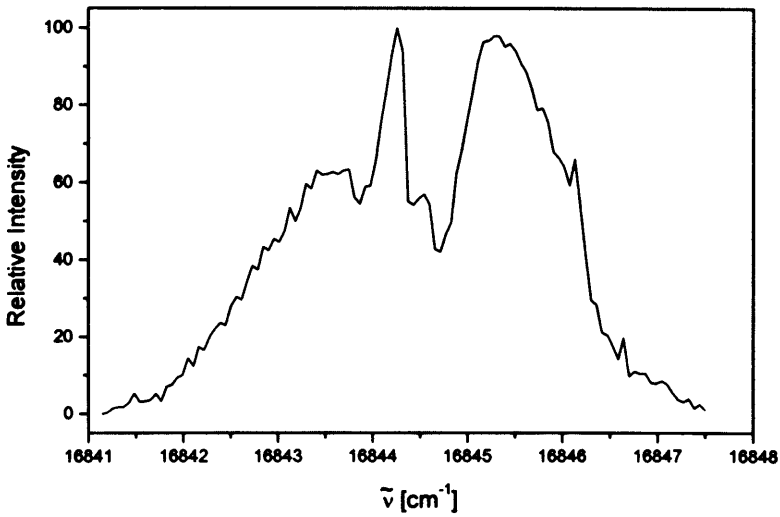


Figure 5.5: Normalised cavity ring-down spectrum of the $T_{1z} \leftarrow S_0$ transition of PT in a supersonic jet.

5.3 Calculation of Lineshapes

The Asyrot program, as described by Birss and Ramsay [12], and later extended by Zauli [13], was designed to help in the analysis of rotational lines of singlet–singlet transitions of asymmetric rotors. Given a set of ground state and excited state rotational parameters and the temperature, the energies and intensities of the rotational state transitions can be accurately calculated. Asyrot adjusted the parameters to achieve the best fit between experimental and calculated spectra. The computation however did assume the availability of a spectrum with rotational transitions resolved.

The approach taken here is similar to Asyrot in that the energies and transitions of the rotational transitions are calculated using exactly the equations given in the Birss and Ramsey paper. The equations are not reproduced here. One point to note is that although the transition under investigation is tech-

nically a T ← S transition, the large zero field splitting of T_z from the $T_{x,y}$ components of the triplet makes using a calculational scheme designed for S ← S transitions acceptable. Each of the calculated rotational lines is then convoluted with a line profile – in this case a Gaussian function was used with width equal to the laser resolution – and all lines sum together to give an overall line shape. This calculated line shape was compared with the experimental one of Figure 5.5.

In this calculation, the following parameters were input.

- Lower State Rotational Constants

  These are:

  A'', B'', C'' and are accurately known from microwave spectroscopy [14].

- Upper State Rotational Constants

  These are:

  A', B', C' and are likely to have values similar to the lower state but have to be determined.

- The Band Origin

- Band Type

  Three Band Type line shapes A, B and C are distinguished for asymmetric rotators and are determined by the direction of the transition dipole moment with respect to the rotational axes (a, b and c). If the two axes have the same symmetry, which is true for any molecular symmetry less than C_{2v}, then Hybrid Band Types occur A/B, A/C and B/C. In the case of the PT origin, the final bandshape is allowed to be a mixture of the A and C bandshapes and the extent of that mixing, M, is another adjustable parameter such that the overall bandshape is,

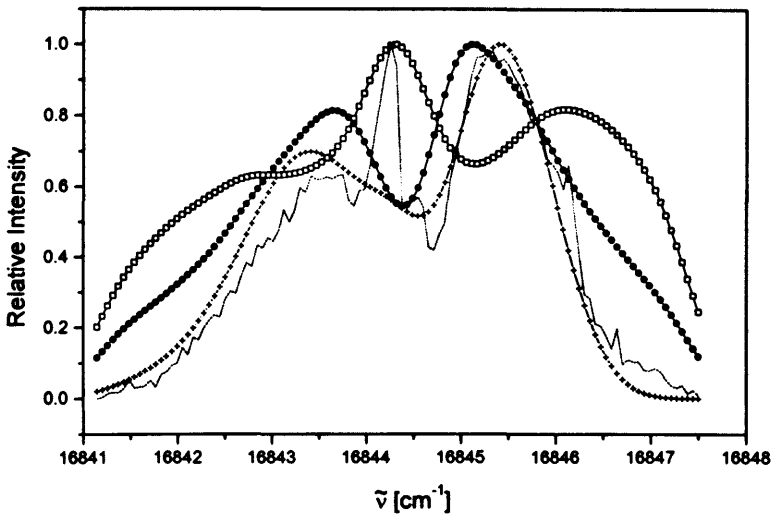


Figure 5.6: Pure A– (+), B– (•) and C–(□) type bandshapes. As can be seen in the above figure the experimentally measured bandshape is not a pure bandshape but a mixture of A– and C– type bandshapes.

$(1 - M)A + (M)C$. Figure 5.6 demonstrates the different bandshapes calculated for pure A–, B– and C–type for the set of parameters finally determined below when allowing A/C mixing. As can be seen the calculated lineshapes do not match the experimental lineshape whereas the mixed lineshape does. Despite an extensive search of reasonable values of the parameters a good match could not be achieved without allowing mixing of A and C lineshapes.

- Nuclear Statistical Weights

  Nuclear statistical weights determine the relative intensities of the rotational lines. The classic example of which is ortho– and para–hydrogen. Ortho–hydrogen rotational lines have an intensity three times that of para–hydrogen due to the influence of the statistical weights. This is

explained further below.

- Rotational Temperature of the molecules in the jet.
- Maximum value of the quantum number J to be included in the calculation. This is purely a computational parameter and was set to 30 throughout this work which was more than sufficient. The maximum value of the quantum number K was set equal to J.

The values of these parameters are optimized using a Simplex routine (which is a multidimensional optimisation routine) or Golden Search routine (a single dimensional optimisation routine), to achieve the best fit between the calculated and experimental curves. This best-fit was determined by minimizing χ^2, the goodness of fit parameter. There are a number of definitions of χ^2 and the one used in this procedure is the most stringent, namely the sum of squares of the differences between the two curves.

The goal of this exercise was to determine the upper state rotational constants, through comparison of a calculated lineshape with that of an experimentally measured one.

Nuclear Statistical Weights

The nuclear statistical weight parameter is expanded on in some detail here as it is the least familiar parameter and not particularly well explained (if at all) in standard text books.

The wavefunction of every rotational level can be described by its symmetry with respect to the three major rotation axes. In fact it is only ever necessary to specify its behaviour with respect to any pair of axes and these then fix its behaviour with respect to the third. It is conventional to use the a and c axes for this purpose and a wavefunction is either even (+) or odd (−) with

$$\frac{1}{2}\ [\ (2I_W+1)^2(2I_X+1)^2(2I_Y+1)^2(2I_Z+1)^2\cdots + (2I_W+1)(2I_X+1)(2I_Y+1)(2I_Z+1)\cdots] \qquad (5.3)$$

where I_W etc. is the nuclear spin of the pair of identical nuclei that are exchanged under rotation. Formulae 5.2 and 5.3 give the symmetric and asymmetric weights depending on whether Bose statistics are employed and conversely if Fermi statistics are employed. Bose statistics are employed if there is an even number of nuclei following Fermi statistics in the group. Fermi statistics are employed if there is an odd number of nuclei following Fermi statistics[1] in the group. In the case of XT with 8 H atoms following Fermi statistics, Bose statistics are employed. Similarly for PT with 4 H atoms following Fermi statistics, Bose statistics are also employed. Therefore, Formula 5.2 determines the symmetric weighting and Formula 5.3 determines the asymmetric weighting.

XT has 4 pairs of identical nuclei of half-integer spin (8 hydrogen atoms) that are exchanged under rotation about the C_2 axis. Therefore, the symmetric weighting is

$$\begin{aligned}\frac{1}{2}\ [\ &\left(2\tfrac{1}{2}+1\right)^2\left(2\tfrac{1}{2}+1\right)^2\left(2\tfrac{1}{2}+1\right)^2\left(2\tfrac{1}{2}+1\right)^2 \\ -\ &\left(2\tfrac{1}{2}+1\right)\left(2\tfrac{1}{2}+1\right)\left(2\tfrac{1}{2}+1\right)\left(2\tfrac{1}{2}+1\right)] \\ =\ &120\end{aligned}$$

The asymmetric weighting is

$$\frac{1}{2}\ [\ \left(2\tfrac{1}{2}+1\right)^2\left(2\tfrac{1}{2}+1\right)^2\left(2\tfrac{1}{2}+1\right)^2\left(2\tfrac{1}{2}+1\right)^2$$

[1] A nucleus follows Fermi statistics if it's a Fermion, i.e. it has a half-integral nuclear spin. Hydrogen with $I = 1/2$ is a Fermion. Those nuclei with integral nuclear spin are called Bosons.

UNIVERSITY COLLEGE CORK Library

$$+ \left(2\tfrac{1}{2}+1\right)\left(2\tfrac{1}{2}+1\right)\left(2\tfrac{1}{2}+1\right)\left(2\tfrac{1}{2}+1\right)]$$
$$= 136$$

This gives a symmetric:asymmetric ratio of 15:17.

Similarly, for PT with 2 pairs of identical nuclei with half-integer spin (4 hydrogen atoms) that are exchanged under rotation the C_2 axis, a symmetric:asymmetric ratio of 3:5 is obtained. According to Birss and Ramsay [12], the nuclear statistical weights are a required input parameter consisting of four integers. These four integers are used to calculate the intensities of transitions involving lower state levels with parity of (K_a, K_c) being ee, eo, oo, oe, corresponding to ++, +−, −− and −+ levels. ++ and −+ are the symmetric weights and +− and −− are the asymmetric weights. This gives values of 15 17 17 15 for XT and 3 5 5 3 for PT as the four statistical weight input integers.

5.4 Results and Discusson

Triplet state rotational energy levels for near–symmetric top molecules were discussed extensively in papers by Hougen [16,17]. In PT the triplet substate T_{1z} practically appears as a single non–degenerate state, which is separated from an effectively degenerate pair $T_{1(xy),0}$ by the large zero–field splitting mentioned in Chapter 1. The energy gap $|D^*| \approx$24–28 cm^{-1} is far larger than the range of rotational energies involved in determining the rotational envelope (in the jet the molecule is rotationally cold and the maximum significant quantum number J is relatively small). Being a near–symmetric top molecule, PT fits exactly to the energy level pattern described as case (ab) type I by Creutzberg and Hougen in [16] and the rotational A–type envelope of the isolated T_{1z} state is governed by energy levels which are virtually indistinguishable from those for a singlet–singlet transition. This is an important precondition for the

calculation of the rotational envelope of jet–cooled PT using the ASYROT-like program.

The ground state parameters have already been determined by MacDonald et al. [14]. Therefore, by applying the above optimisation algorithm the excited state parameters may be determined. As this is a very computer–time intensive process (as regards desktop PC computing time) a lot of time and energy was expended in obtaining the following results.

Planar Geometry of the $T_{1_{\pm},0}$ State

The geometry of the first excited triplet state of PT has been stated to be planar [14, 18] although there is no direct empirical evidence to support this. The rotational constants of planar geometries are not independent of each other (see the discussion of Inertial Defect below) and this provides an additional constraint on their values. The calculated lineshapes are very sensitive to small changes in the input rotational constants and therefore it is comparatively straightforward to search reasonable values of the rotational constants for a (nearly) planar geometry. Such searches were performed but no acceptable agreement between calculated and experimental lineshape was found. Although reasonable fits were obtained a quantitative match between theory and experiment was not possible. The best of these calculated lineshapes are shown in Figure 5.7. A calculated lineshape was deemed to have reached a 'best fit' when a certain tolerance value was reached. This tolerance value was set such that $|\Delta\chi_i^2 - \Delta\chi_{i+1}^2|/\Delta\chi_i^2$ was less than 1%. As none of these 'best fit' lineshapes achieved this tolerance value, it was not possible, therefore, to obtain any valuable spectroscopic information from these calculations.

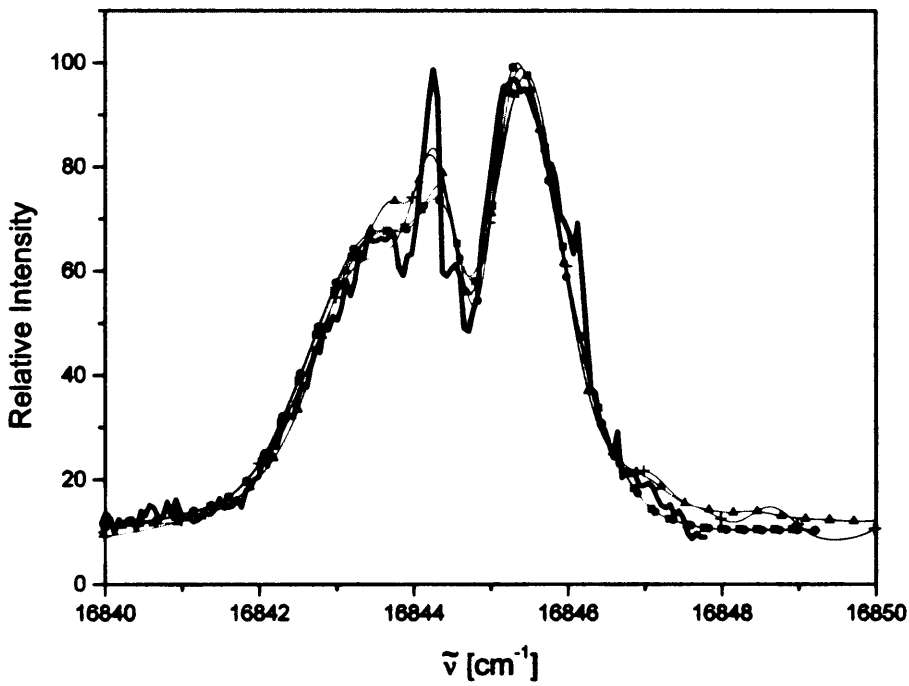


Figure 5.7: Calculated lineshapes of the $T_{1x,0}$ absorption line of PT using Asyrot assuming planar geometry. Full line is the experimentally measured lineshape; Other traces are various "best fits" to the experimental measurement.

A''	0.1975797 cm^{-1}
B''	0.0535336 cm^{-1}
C''	0.0421239cm^{-1}

Table 5.2: Ground State Rotational Constants of PT as determined by MacDonald et al. [14]

Non-Planar Geometry of the $T_{1x,0}$ State

In the following, no assumptions about the geometry of PT were made and this allowed the rotational constants to be independent of each other. In Figure 5.8, the computed best–fit lineshape is plotted along with the normalised experimental data. This lineshape did achieve the tolerance value of 1%. The excited state rotational constants obtained from this fit are shown in Table 5.3.

The goal of this exercise was to obtain the excited state parameters of PT. Although this could not be achieved by constraining the molecule to a planar structure it was indeed possible by allowing non-planarity. The values of the rotational constants in the lower and upper states are quite similar, the upper state rotational constants decreasing by less than 1.7% compared to the ground state values. It is most likely that these changes in rotational constants are due to geometric changes in the region of the C=S bond due to a lengthening of the C=S bond in the triplet state.

The value for the rotational temperature has been calculated above to be 14.28 K. This is in good agreement with a value of 9.0 ± 2.5 K for azulene in a supersonic jet [8]. The central energy of 16844.45 cm^{-1} compares well with a value of 16844.70 cm^{-1} as read from Figure 5.5. The instrumental resolution of 0.337 cm^{-1} compares well with the laser manufacturers quoted resolution of $\approx$0.3 cm^{-1}. A final upper state parameter that has been obtained from this calculation is the degree of mixing, M, of band types A and C. The effect of mixing is that PT is no longer a planar molecule in the excited state. For a perfectly planar molecule

$$I_C = I_A + I_B$$

The Inertial Defect Δ is given by

$$\Delta = I_C - I_A - I_B$$

A'	0.1944145cm^{-1}
B'	0.0528577cm^{-1}
C'	0.0417536cm^{-1}
T	14.279 K
E	16844.45 cm^{-1}
R	0.337 cm^{-1}
M	0.397

Table 5.3: Calculated Excited State Rotational Constants of PT. Also shown are the rotational temperature, T, the centre energy, E, instrumental resolution, R and the degree of bandtype mixing (A/C), M.

This can be expressed in terms of the rotational constants A, B, C, such that

$$\Delta = \frac{1}{C} - \frac{1}{A} - \frac{1}{B}$$

This definition is based on the convention that the rotational constants have the following relationship $A > B > C$. The inertial defect is an indicator of the planarity of a molecule. For planar molecules Δ is equal or close to zero, for non–planar molecules Δ is usually negative. For the ground state of PT which is known to be planar the inertial defect is -1.636×10^{-3} (cm^{-1})$^{-1}$, for the calculated excited state from the values given above is -8.0187×10^{-2} (cm^{-1})$^{-1}$. To place these values in perspective, the Inertial Defects of ground state pyridine and pyridazine (similar sized and planar molecules) are -1.8780×10^{-3} and -1.5237×10^{-3} (cm^{-1})$^{-1}$ respectively (using data from the tables in [19]) whilst that of cyclopentadiene (planar framework with out of plane hydrogen atoms) is -0.18418 (cm^{-1})$^{-1}$. Possibly more indicative is the value for the ground state of Cl_2CO, which at $+1.466 \times 10^{-2}$ (cm^{-1})$^{-1}$, approaches that found for the excited state of PT yet is for a planar molecule. This apparently large value is owing to the more flexible bonding relating to the Cl atoms compared with the H atoms of H_2CO (Inertial Defect, $+3.333 \times 10^{-3}$ (cm^{-1})$^{-1}$) for example. Whilst none of this is definitive, the value calculated for the excited state of PT would appear to be reasonable for a slightly non-planar geometry.

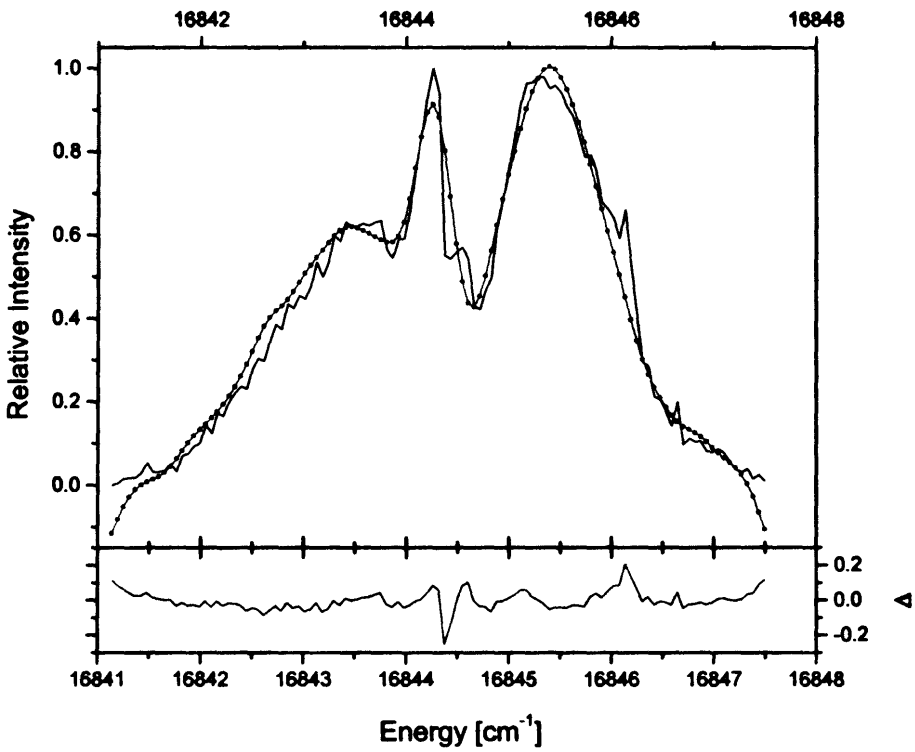


Figure 5.8: Best fit of the $T_{1s,0}$ absorption line using Asyrot allowing non–planar geometry of the excited state. Full line is the experimentally measured lineshape; dotted line is the calculated line shape. The lower trace is the residuals, $\Delta = I_{\text{measured}} - I_{\text{calculated}}$

5.5 Summary

In this Chapter, it has been shown that in the case of PT with a large zero–field splitting of the triplet substates the $T_{1z,0}$ lineshape may be calculated using the Asyrot program, a program designed primarily for singlet–singlet transition lineshape calculations. However, although a very good fit was achieved, the excited state geometry predicted was not that inferred by other measurements. The results obtained in Table 5.3 must be treated with some caution. The geometry of the triplet state of PT that these values of A', B' and C' represent is a non–planar structure. This structure is supported by Maciejewski et al. [20] and references therein who state that PT undergoes large changes in geometry in the excited state. Similarly, Ruth et al. [10] state that the C=S stretch mode in PT carries a far smaller proportion of oscillator strength of the $S_0 \rightarrow T_1$ transition than is the case for BPT suggesting that PT undergoes a more significant distortion in the $S_0 \rightarrow T_1$ excitation process than for BPT. However, this non-planar geometry is in contradiction of other studies which state that PT is planar in the ground state [14,18] and the first excited state [18]. It may be that the thiocarbonyl group and the two α-carbons of the ring form a local C_{2v} geometry but that the T_1 state has C_s symmetry overall. In Chapter 4 the activity of the C=S group was shown to dominate the vibrational structure. This localisation of activity may indeed make it possible for PT to have a non-planar T_{1z} excited state geometry and still behave according to the C_{2v} point group. When the excited state geometry was constricted to planarity, the desired spectroscopic information could not be consistently achieved.

Bibliography

[1] G. Berden, R. Peeters, and G. Meijer. *Int. Rev. Phys. Chem.*, 19(4):565–607, 2000.

[2] K.W. Busch and M.A. Busch (Editors). *Cavity-ringdown spectroscopy. An ultratrace-absorption measurement technique.* American Chemical Society, Symposium Series 720. Oxford University Press, Oxford, 1999.

[3] M.D. Wheeler, S.M. Newman, A.J. Orr-Ewing, and M.N.R. Ashfold. *J. Chem. Soc., Faraday Trans.*, 94:337, 1998.

[4] J. Scherer, J.B. Paul, A. O'Keefe, and R.J. Saykally. *Chem. Rev.*, 97:25, 1997.

[5] A.A. Ruth, T. Fernholz, R.P. Brint, and M.W.D. Mansfield. *Chem. Phys. Lett.*, 287:403–411, 1998.

[6] L.H. Spangler, Y. Matsumoto, and D.W. Pratt. *J. Phys. Chem*, 87:4781, 1983.

[7] A.A. Ruth, F.J. O'Keeffe, R.P. Brint, and M.W.D. Mansfield. *Chem. Phys.*, 217:83–98, 1997.

[8] A.A. Ruth, E.-K. Kim, and A. Hese. *Phys. Chem. Chem. Phys.*, 1:5121, 1999.

[9] A.A. Ruth, T. Fernholz, M.W.D. Mansfield, and R.P. Brint. *J. Mol. Spectrosc.*, 214:80–86, 2002.

[10] A.A. Ruth, F.J. O'Keeffe, M.W.D. Mansfield, and R.P. Brint. *J. Phys. Chem. A*, 101(42):7735–7741, 1997.

[11] Á. Somogyi, G. Jalsovszky, C. Fülöp, J. Stark, and J.E. Boggs. *Spectrochim. Acta*, 45A:679, 1989.

[12] F.W. Birss and D.A. Ramsay. *Computer Phys. Comm.*, 38:83, 1984.

[13] C. Zauli. *Computer Physics Communications*, 79:555–560, 1994.

[14] J.N. MacDonald, S.A. Mackay, J.K. Tyler, A.P. Cox, and I.C. Ewart. *J. Chem. Soc., Faraday Trans. 2*, 77:79–99, 1981.

[15] G. Herzberg. *Molecular Spectra and Molecular Structure*, volume II. Infrared and Raman Spectroscopy of Polyatomic Molecules. Van Nostrand Reinhold Company, 1945. Chapter I, 1. Pages 14–17.

[16] J.T. Hougen. *Canadian Journal of Physics.*, 42:433, 1964.

[17] F. Creutzberg and J.T. Hougen. *Canadian Journal of Physics.*, 45:1363, 1967.

[18] J. Tatchen, M. Waletzke, C.M. Marian, and S. Grimme. *Chem. Phys.*, 264:245, 2001.

[19] G. Herzberg. *Molecular Spectra and Molecular Structure*, volume III. Electronic Spectra and Electronic Structure of Polyatomic Molecules. Van Nostrand Reinhold Company, 1966.

[20] A. Maciejewski, A. Safarzadeh-Amiri, R.E. Verrall, and R.P. Steer. *Chem. Phys.*, 87:295, 1984.

Chapter 6

Conclusions

1. The direct $T_1 \leftarrow S_0$ transition of isolated XT in a molecular jet has been measured up to an excess energy of $\approx$ 3000 cm^{-1}. The T_{1z} origin has been observed at 14927.4 cm^{-1}, corresponding to a hypsochromic shift of $\approx$ hc $\times$ 175 cm^{-1} and $\approx$ hc $\times$ 203 cm^{-1} compared to a Shpolskii matrix and an alkane solvent, respectively. 19 fundamental modes have been assigned and a vibronic origin based on ν_7 has been assigned.

2. A serious doubt has been raised over the assignment of S_1 by Mahaney and Huber, and it is this value of S_1 that has been cited since. The progression observed in a Shpolskii matrix and assigned as a progression in S_1 is now in considerable doubt. However, until the exact position of S_1 is confirmed, the assignment of ν_7 is tentative. In order to confirm the energy of the S_1 origin a multiphoton absorption experiment would have to be attempted.

3. The $T_1 \rightarrow S_0$ phosphorescence excitation spectrum was measured upon absorption in $^1(\pi\pi^*) \leftarrow X^1A_1$ band of jet–cooled PT up to an excess energy of $\approx hc \times 1200$ cm^{-1} above the 0–0 transition, which is located around $\approx hc \times 27500$ cm^{-1}. An intermediate level structure was found,

which is due to the strong vibronic coupling of $^1(\pi\pi^*)$ with a dark $^1(n\pi_2^*)$ state at lower energy. The energy gap between the two states has been estimated to be approximately $hc \times 825-1025$ cm^{-1}. Hence $^1(n\pi_2^*)$ should be attributed to the second excited singlet state S_2 in PT, whereas $^1(\pi\pi^*)$ appears to be the third excited singlet state S_3.

4. Four repetitive patterns of transitions were found in the spectrum and several progressions of mixed states across the pattern were identified and tentatively assigned. Through evaluation of the linewidths in the origin pattern a lower limit of the lifetime of the highly mixed states was estimated to be $\approx$ 4 ps. A fast decay channel involving the states $^1(n\pi_2^*)(\equiv S_2)$ and $^3(\pi\pi_2^*)(\equiv T_3)$ was suggested in order to explain the violation of the energy gap law in comparison to other aromatic thiocarbonyl compounds.

5. In the case of PT with a large zero-field splitting of the triplet substates the $T_{1_{z,0}}$ lineshape may be calculated using the Asyrot program, a program designed primarily for singlet–singlet transition lineshape calculations.

   The first exited triplet state rotational constants have been calculated to be $A' = 0.1944145$ cm^{-1}, $B' = 0.0528577$ cm^{-1}and $C' = 0.0417536$ cm^{-1}, a non-planar geometry.

List of Tables

1.1 K_h Point Group 8

1.2 Species of spin functions for the more important point groups . 8

1.3 C_{2v} Point Group Table. 9

2.1 Microanalysis of synthesised PT 36

2.2 NMR spectra of synthesised PT. 37

2.3 Centreline Mach number parameters A, x_0 and $x_{\min}$. 40

3.1 Assignment and comparison of vibrational modes of XT 56

3.2 Frequencies of vibrational modes of T_1 in XT 58

3.3 Comparison of the most prominent progressions of XT based on vibronic origins ν_{43}, ν_3, ν_7 and ν_{12}. 59

4.1 List of spectroscopic features of the excitation spectrum of PT . 81

4.2 Prominent progressions and combinations of patterns P1...P4 of PT. 85

5.1 Revised symmetry and vibronic labelling for PT 101

5.2 Ground State Rotational Constants of PT 110

5.3 Excited State Rotational Constants of PT 112

List of Figures

1.1 PT, BPT and XT 2

1.2 C=S Chromophore Orbital Configuration 3

1.3 Triplet sublevels of C_{2v} thiones. 6

1.4 Jabloński Diagram 10

1.5 Jabloński Diagram for isolated molecules in a jet. 13

1.6 Simplified Jabloński Diagram 18

1.7 Schematic illustrating the three limiting cases in luminescence kinetics 19

2.1 Phosphorescence Excitation Experimental Setup 24

2.2 General Valve Corporation "Iota One" Pulsed Nozzle 27

2.3 Jet valve unit embedded in the copper block 28

2.4 Laser light passing through an optical cavity 31

2.5 Cavity Ring–down apparatus 35

2.6 Supersonic Jet Expansion 39

2.7 Velocity Distributions 42

3.1 Lens and filter arrangement in the phosphorescence excitation spectrum of XT 48

3.2 The $S_0 \rightarrow T_1$ Phosphorescence Excitation Spectrum of XT in a supersonic jet. 49

3.3 Comparison of vibronic transitions 60

3.4 Comparison of Vibration Intensities of XT 61
3.5 Density of States, ρ, for XT 67

4.1 Excitation spectrum of the $^3(n\pi^*) \rightarrow$ X $^1A_1$ phosphorescence in the region of the $^1(\pi\pi^*) \leftarrow$ X $^1A_1$ absorption band between 27400 and 28800 cm^{-1}. 73
4.2 $^3(n\pi^*) \rightarrow^1$ X phosphorescence emission spectrum upon excitation at 28499 cm^{-1}. 75
4.3 PT Phosphorescence Decay 76
4.4 Comparison of the four patterns P1 to P4 in the phosphorescence spectrum of PT 78
4.5 Excess energy dependence of the number of vibronic states . . . 84
4.6 Fit of Lorentzian profiles of lines in pattern P1 of PT 89

5.1 CRD absorption spectrum of oxygen 97
5.2 1,4-diaminoanthraquinone (DAAQ) 97
5.3 Cavity ring–down absorption spectrum of PT at room temperature 98
5.4 Comparison of the $T_{1z,0} \leftarrow S_{0,0}$ line in a static cell absorption, through phosphorescence excitation in a jet and through absorption in a jet. 100
5.5 Cavity ring-down spectrum of the $T_{1z} \leftarrow S_0$ transition of PT in a supersonic jet. 102
5.6 A–, B– and C– type bandshapes 104
5.7 Calculated lineshapes of the $T_{1z,0}$ absorption of PT using Asyrot assuming planar geometry 110
5.8 Best fit of the $T_{1z,0}$ absorption line using Asyrot 113